

Designing Novel High-Performance Anode Materials for Li-ion Batteries



Thesis submitted to,
Indian Institute of Science Education and Research, Pune

for the award of the degree of

DOCTOR OF PHILOSOPHY

in Chemical Sciences

by

Kingshuk Roy

(Integrated Ph.D. Student; Department of Chemistry; Indian Institute of Science
Education and Research, Pune; Registration number: 20142010)

Research Supervisor

Dr. Ramanathan Vaidhyanathan

Associate Professor

Dept. of Chemistry, IISER Pune

Research Co-supervisor

Prof. Satishchandra B. Ogale

Emeritus Professor

Dept. of Physics, IISER Pune

July 2020

CERTIFICATE

This is to certify that this dissertation entitled “Designing Novel High-Performance Anode Materials for Li-ion Batteries” for the award of the degree of “**DOCTOR OF PHILOSOPHY**” in Chemical Sciences at the Indian Institute of Science Education and Research, Pune represents original research carried out by Mr. Kingshuk Roy at Indian Institute of Science Education and Research, Pune under the supervision of Dr. Ramanathan Vaidhyanathan, Associate Professor, Department of Chemistry and Centre for Energy Science, Indian Institute of Science Education and Research, Pune and Prof. Satishchandra B. Ogale, Emeritus Professor, Department of Physics and Centre for Energy Science, Indian Institute of Science Education and Research, Pune during the spring semester of academic year 2020. It is further certified that this work has not been submitted to any other University or Institution in part or full for the award of any degree or diploma. Research material obtained from other sources has been duly acknowledged in the thesis. Any text, illustration, table etc. used in the thesis from other sources, have been duly cited and acknowledged.

Research Student

Mr. Kingshuk Roy

Research Supervisor

Dr. Ramanathan Vaidhyanathan

Associate Professor

Dept. of Chemistry, IISER Pune

Date: 25 July, 2020

Research Co-supervisor

Prof. Satishchandra B. Ogale

Emeritus Professor

Dept. of Physics, IISER Pune

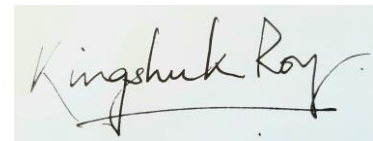
Place: IISER PUNE

DECLARATION

I hereby declare that the matter embodied in the report entitled “Designing Novel High-Performance Anode Materials for Li-ion Batteries” are the results of the investigations carried out by me at the Department of Chemistry and Centre for Energy Science, Indian Institute of Science Education and Research, Pune under the supervision of Dr. Ramanathan Vaidyanathan and Prof. Satishchandra B. Ogale and the same has not been submitted elsewhere for any other degree.

Date: 25 July, 2020

Research Student

A rectangular box containing a handwritten signature in black ink that reads "Kingshuk Roy".

Place: IISER Pune

Kingshuk Roy

ACKNOWLEDGEMENTS

At the outset, I, would like to express my sincere thanks and regards to everyone who has helped me in one way or the other and thereby contributed in this exciting journey of mine towards the fulfilment of my long-cherished dream.

First of all, I would like to express deep sense of gratitude to my supervisors Dr. Ramanathan Vaidhyanathan and Professor Satishchandra B. Ogale for providing me outstanding labs and excellent working environment. Throughout my entire Ph.D. programme, their patience, enthusiasm, immense knowledge, constant motivation and positive feedback have not only helped me finish my Ph.D. in the available time frame but also to become an independent thinker. Amongst various other things they have instilled in me the importance of always being technically sound and scientifically ethical. Their teachings through weekly group meetings and various informal chats during the morning and afternoon coffee sessions were very valuable in building me as a researcher and human being both.

Also, I would to express my deep gratitude and respect to my RAC members Dr. Manjusha Shelke and Prof. R. Boomi Shankar for their continuous support and extremely valuable scientific inputs during the last 4 years, especially during my RAC meetings.

My deepest regards are also due to the former director, Prof. K.N Ganesh and the present director, Prof. Jayant Udgaonkar to providing me such a state-of-the art institute, first rate research infrastructure and rich academic ambience. The numerous invited talks by experts, symposia and conferences held at IISER Pune always brought rich insights to all of us.

I am very much thankful to the Chairs, Dept. of Chemistry (Formerly Prof. M. Jayakannan and presently, Prof. H.N. Gopi) and Chairs, Dept. of Physics (formerly, Prof. Sunil Mukhi and presently, Prof. T. Souradeep) for letting me use the facilities of the Dept. of Chemistry and Dept. of Physics, respectively. I would like to give my deepest regards to IISER Pune MHRD for providing me fellowship which was very much helpful to me in various regards.

I would like to respectfully acknowledge all my academic collaborators who helped me shape the

research projects well, which is reflected in the final outcome. I would like to make a special mention to Sattwick with whom I had a significant overlap in terms of research interest, thoughts, and project development. It was a real joy and fun working with him in the projects.

I would further like to convey my sincere thanks to DST, UK-India Education Research Initiative (UKIERI) and Newton Prize funds for sponsoring my exchange program visits to the University of Edinburgh, the University of Cambridge, and the University of Swansea, UK. My special thanks to Prof. Neil Robertson and Tianyue Li at Edinburgh and several colleagues including Trysten Watson, Serena Margadona, Jenny Baker, Ian Mabbett at Swansea for their help, academic advice and friendship.

I would like convey my regards to all my present and past lab mates, especially, Abhik, Aniruddha, Rounak, Rohan, Umesh, Satyawan, Dipti, Rajesh, Abhijit, Mani, Reena, Minal, Shiva, Vishal, Pradeep, Rounak, Anil, Monika, Mukta, Surendar, Yogesh, Padmini, Satish, Vinila, Padmini, Richa, Subas, Supriya, Prachi, Swati, Srashti, Ishita, Shrreya, Shyamapada, Debanjan, Rahul, Sattwick, Dinesh, Shalini, Himan, Pragalb, Rinku for their helpful and extremely supportive nature, and their friendship which made this journey totally enjoyable and exciting. I would like to acknowledge all my batchmate and friends, especially, Sumanta, for always being very supportive.

I would like to give my heartiest thanks and regards to all the academic and non-academic staff, especially Tushar, Sayalee, Priyadarshini, Prabhas, Prabhakar, Mayuresh for being extremely helpful throughout the last 6 years of my stay at IISER Pune.

I would like to specially mention and give my deepest thanks to Debashree for always being there by me and being extremely supportive and providing mental boost whenever I felt low in my life.

Finally, words are not enough to give my heartiest and the deepest regards to my loving parents and family members without whom it would not have been possible to pursuing my research career.

Though, I may have missed to mention some friends and colleagues by name, I greatly appreciate all their support and help throughout my time at IISER Pune.

Dedicated to my Beloved Parents

LIST OF ABBREVIATIONS**Abbreviation****Full form**

AKA	As known as
BET	Brunauer–Emmett–Teller
CAC	Commercial Activated Carbon
CNS	Carbon nanosphere
CNFs	Carbon Nano Fibers
CNTs	Carbon Nanotubes
CV	Cyclic Voltammogram
CVD	Chemical Vapour Deposition
DMF	Dimethylformamide
EDAX	Energy dispersive Analysis of X-rays
EDLC	Electrochemical double layer capacitor
EES	Electrical Energy Storage
EIS	Electrochemical Impedance Spectroscopy
ESR	Equivalent Series Resistance
EV	Electric Vehicle
FE SEM	Field emission scanning electron microscopy
FWHM	Full width at half maximum
HEV	Hybrid Electric Vehicle
HR TEM	High resolution transmission electron microscopy

HTC	Hydrothermal Carbonization
IMPC	Interconnected Microporous Carbon
Li-HEC	Lithium ion hybrid electrochemical capacitor
LIBs	Lithium ion batteries
SIBs	Sodium ion batteries
GIXRD	Grazing incidence X-ray diffraction
XPS	X-ray photo electron spectroscopy
FLBP	Few layer black phosphorous

CONTENTS

Thesis synopsis	
Chapter 1. Introduction	
1. Global Energy demand, energy sources and energy storage:	
2. Introduction to the basic energy storage devices	
✚ Conventional di-electric capacitors.....	
✚ Electrochemical capacitors.....	
✓ Electrocheical double layer capacitors.....	
✓ Hybrid supercapacitors.....	
✓ Pseudocapacitors.....	
✚ Batteries.....	
3. Introduction to Li-ion batteries	
4. Materials for Li-ion batteries	
4.1. Potential anode materials for Li-ion batteries	
4.1.1. Intercalation anode materials	
✚ Graphitic and other carbonaceous anodes.....	
✚ Lithium titanium oxide (LTO/ $\text{Li}_4\text{Ti}_5\text{O}_{12}$).....	
4.1.2. Alloying anode materials	
4.1.3. Conversion anode materials	
4.2. Potential cathode materials for Li-ion batteries	
4.2.1. Intercalation cathode materials	
✚ Transition metal oxides.....	
✚ Polyanionic compounds.....	
4.2.2. Conversion cathode materials	
5. References	

Chapter 2. Fe₃SnC@CNF: A 3D Antiperovskite Intermetallic Carbide System as a New Robust High-Capacity Lithium-Ion Battery Anode.

1. Introduction.....
2. Experimental section.....
3. Result and discussions.....
4. Conclusion

Chapter 3. Room temperature processed in-situ carbon-coated vanadium carbide (VC@C) as a high capacity robust Li/Na battery anode material

1. Introduction.....
2. Experimental section.....
3. Result and discussions.....
4. Conclusions.....

Chapter 4. High capacity, power density and cycling stability of silicon Li-ion battery anode by few layer black phosphorous additive

1. Introduction.....
2. Experimental section.....
3. Result and discussions.....
4. Conclusions.....

Conclusions.....**Appendix.....**

Thesis Synopsis

This thesis discusses original works done by Mr. Kingshuk Roy on designing unique and novel anode materials for Li-ion batteries. The overall thesis is divided into four chapters and ends with an appendix. The first chapter introduces the thesis followed by three working chapters.

Chapter 1. This chapter provides a brief idea about the global energy demand, need for renewable energy sources and efficient energy storage devices to store the energy. It also provides basic idea about the basic energy storage systems such as batteries and capacitors followed by their working principle. Although there are exist various energy storage systems of interest, this introduction chapter provides a detailed discussion of batteries, especially Li- ion battery and its working principle and the electrode materials which are being used in this device since the working chapters of this thesis are based on electrode materials for Li-ion batteries.

Chapter 2: This chapter provides an original work on the very first report of a ternary intermetallic 3D carbide with unique antiperovskite structure involving both transition (Fe) and post transition (Sn) metals, namely Fe_3SnC , as a stable high capacity anode material for Li ion battery. DFT based computational studies reveal that Li insertion results in deviation from the cubic anti-perovskite structure with a volume expansion that induces significant strain in the electrode as is evident from the XRD and SAED data. We have also in-situ synthesized Fe_3SnC Carbon Nano Fiber (CNF) composite and realized a very impressive cyclic stability. Initial discharge capacity was found to be 1045 mAhg^{-1} and along with a stable reversible capacity of 600 mAhg^{-1} at $200 \text{ mA}g^{-1}$ and 500 mAhg^{-1} at 1 Ag^{-1} after 1000 charge discharge cycle with almost $\sim 96\%$ retention of capacity. Similarly, exceptionally high rate performance was observed with a high value of $\sim 500 \text{ mAhg}^{-1}$ obtained even at a current of 2 Ag^{-1} . Fe_3SnC is thus projected as a novel and very efficient material among the 3D carbide systems with the corresponding Li storage performance competing the best materials. We believe that this work will open up various new possibilities to focus on intermetallics and 3D carbide systems to be explored in the field of energy storage.

Chapter 3: This chapter provides an original work done on synthesis of an *in-situ* carbon encapsulated VC (VC@C) nanocomposite with three-dimensional core-shell structure by a

single-step room-temperature ball milling procedure and investigation of its electrochemical performance as anodes for LIBs and SIBs. The as-prepared VC@C shows a clear promise for practical use in terms of electrochemical performance with an impressive capacity of 640 mAh g^{-1} after 100 discharge/charge cycles at 0.1 A g^{-1} for LIBs with very high reversibility. The same material also proves to be a good host for Na ions with very good rate capability and cyclic stability. Post cyclic GIXRD data prove that the reversibility and rate capability can be attributed to the robust nature of 3D carbide since the cubic structure of the material remains intact upon charging and discharging. Indeed, VC appears to be one of the most stable battery materials in the current family of anode materials. The room temperature mechano-chemical ball-milling synthesis strategy reported in this present work is facile and cost-effective and therefore, can be expected to be a promising development for the synthesis of other transition metal carbides with different morphologies for use as a potential material in energy storage devices.

Chapter 4: This chapter provides an original work on designing a SiNP based anode for Li-ion batteries with an optimal small quantity of FLBP as physical additive which has provided very impressive capacity and stability. This is a departure from the commonly used approach employing different forms of functional carbons as additives or partner materials in Si-C composites. Our approach harnesses the uniquely flexible lithiation/delithiation stress absorbing character of FLBP that is far superior to most carbon forms. Thus, very high capacity values reaching 3386 mAh g^{-1} and 2331 mAh g^{-1} at current densities of 0.1 A g^{-1} and 0.5 A g^{-1} , respectively, are obtained with impressive stability measured up to 250 cycles. We believe that this work will open new avenues for possible utilization of other novel 2D materials in the alkali ion battery context.

Chapter 1

Introduction

This chapter provides a broad introduction to the basic energy storage systems like capacitors and batteries. Different forms of capacitors such as parallel plate capacitors, electrochemical double layer capacitors (EDLC), pseudocapacitors were introduced followed by a broad introduction to Li-ion batteries. This chapter talks about detailed working principle of Li-ion batteries followed by the major components of Li-ion batteries. Past, present and future electrode materials for Li-ion batteries which includes various types of cathodes and anodes are being duly introduced in this chapter.

1. Global Energy demand, energy sources and energy storage:

In the modern electrically driven society, one of the major concerns of people is the climate change due to global warming. Since last 35 to 40 years the global energy demand has increased tremendously, resulting in a decrease of non-renewable fossil fuel sources at a scary rate as ~85-90%, since the total global energy demand is currently fulfilled mostly by the non-renewable fossil fuels itself. Figure 1 shows the primary energy consumption of the top 20 countries worldwide.

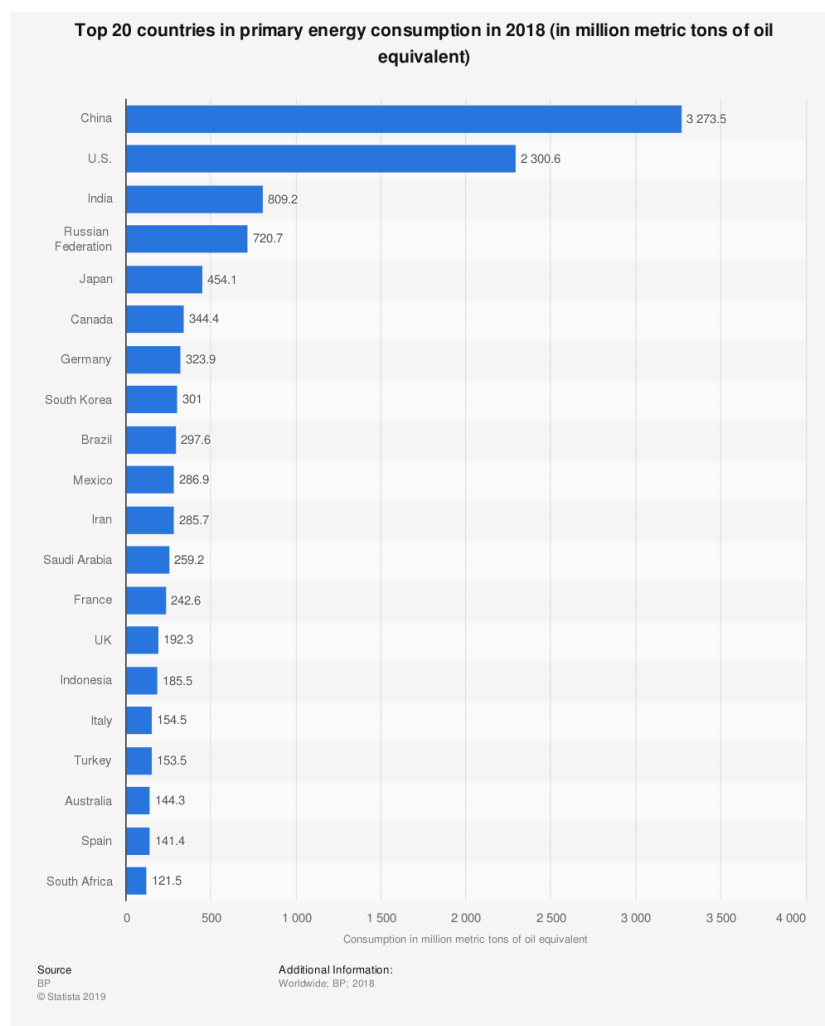


Figure 1. Primary energy consumption of the top 20 countries. (Adapted from <https://www.statista.com/statistics/263455/primary-energy-consumption-of-selected-countries/>)

The non-renewable energy sources are not only decreasing in a pretty quick manner, these sources also pollute the environment significantly, raising serious environmental concerns.

Hence, the major focus of the 21st century research is to employ various renewable energy sources to meet up the enormous energy demand worldwide. Renewable energy sources essentially involve energy obtained from sources such as highly abundant solar and wind energy. However, one of the major problems of using renewable energy sources lies in the fact that these energy sources are intermittent in nature which prohibits their usage throughout the day or throughout the year. Also the time domains of their availability do not necessarily match the time domains of the societal needs. Moreover energy requirements for applications such as mobility or transportation require the energy to be carried along rather than located at a fixed place.

Figure 2 reveals the percent usage of renewable and non-renewable energy sources worldwide.

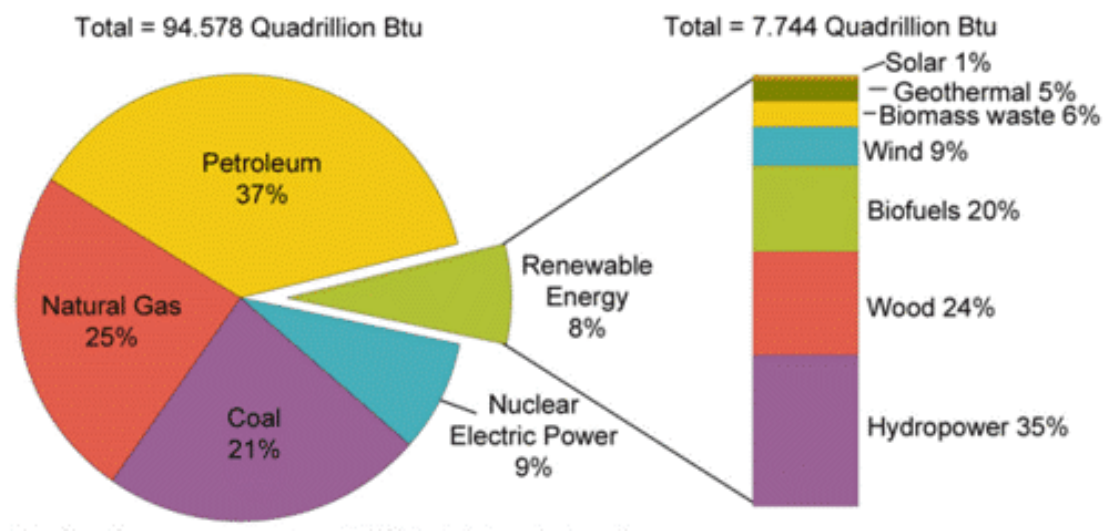


Figure 2. Renewable and non-renewable energy sources. (Adopted from <https://openoregon.pressbooks.pub/envirobiology/chapter/11-2-non-renewable-energy-sources/>)

Nonetheless, in the last 4-5 years renewable energy sources are getting much more popular and researchers are coming up with various ideas to harvest these energies properly. Figure 3 provides a statistic about the usage of renewable energy sources by the EU, who appear to be leading this front.

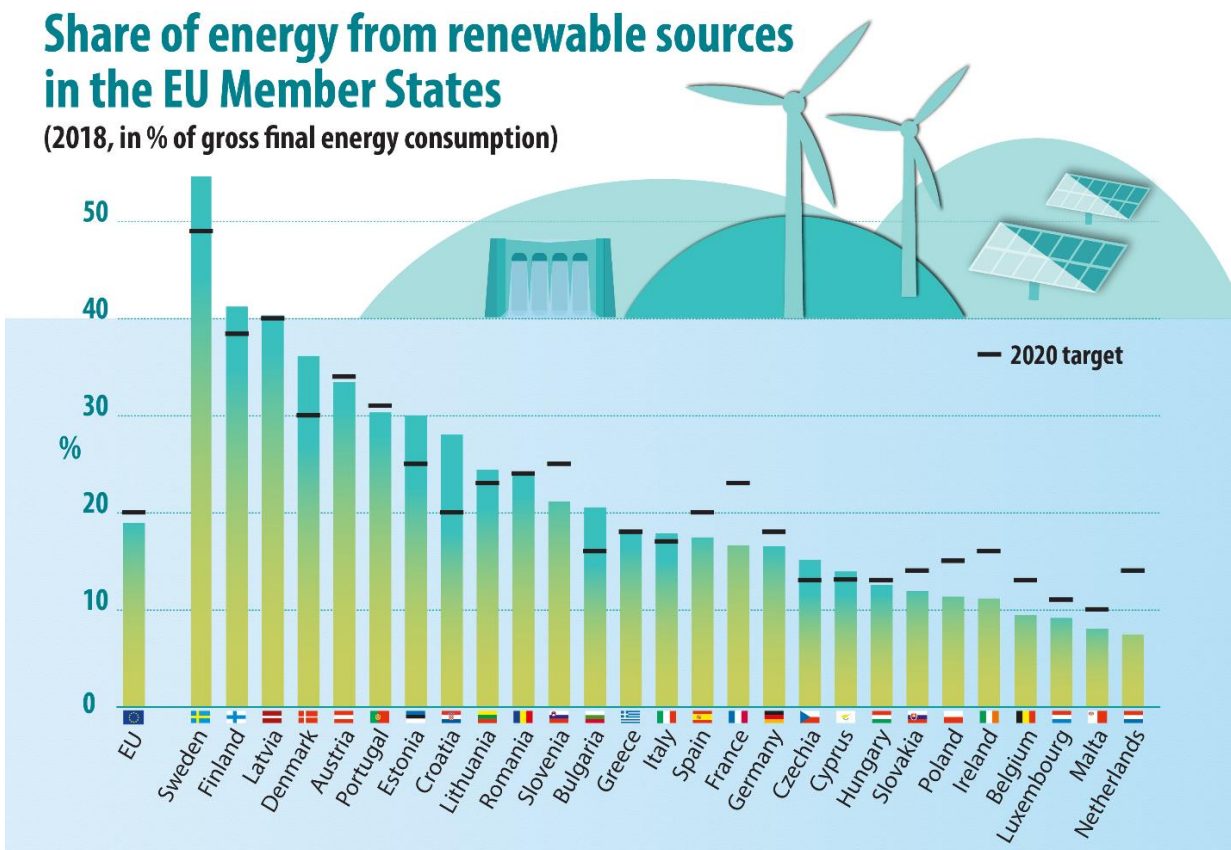


Figure 3. Share of energy from renewable sources by the European Union (Adopted from https://ec.europa.eu/eurostat/statistics-explained/index.php/Renewable_energy_statistics)

The above arguments and observations strongly suggest the urgent and growing need for energy storage devices which can store the energies at significant energy density and deliver the same at a fast space (power density) as per the requirement. The basic energy storage systems majorly include batteries, supercapacitors, fuel cell etc. These have their own advantages in terms of energy and power efficiency. Batteries and fuel cell are high energy density devices which allows them to deliver the stored energies for a long period of time whereas, supercapacitors are high power density devices which provides very high power but for a short time.

Figure 4 presents the Ragone plot which basically provides a comparative idea about the energy density and power density of different energy storage devices.

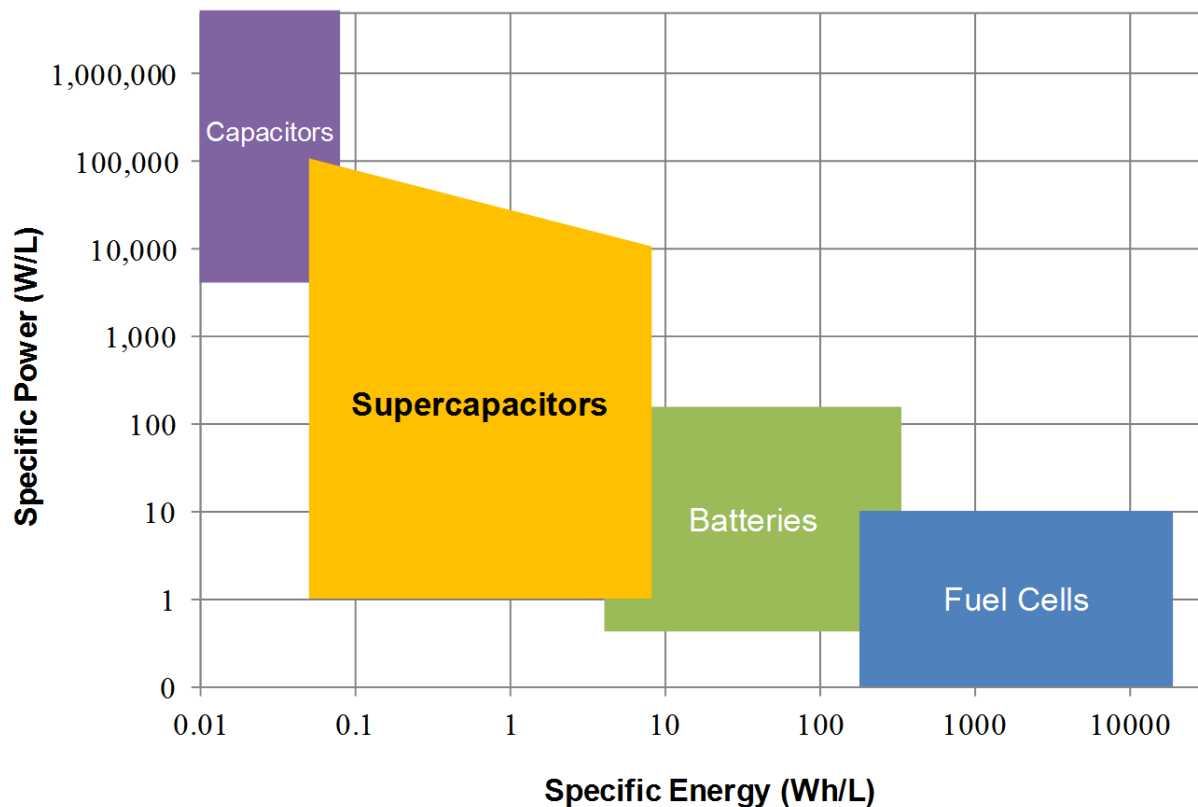


Figure 4. Ragone plot showing energy density and power density for various energy storage devices (Adopted from <https://www.cap-xx.com/resource/energy-storage-technologies/>)

In the following we focus on the discussion of the charge storage materials and systems, since this is the focus of the work presented in this thesis.

2. Introduction to the basic energy storage devices:

Basic energy storage devices broadly include batteries and capacitors. Capacitors can again be classified into two broad categories of parallel plate capacitors and supercapacitors. Figure 5 shows the classification of energy storage devices.

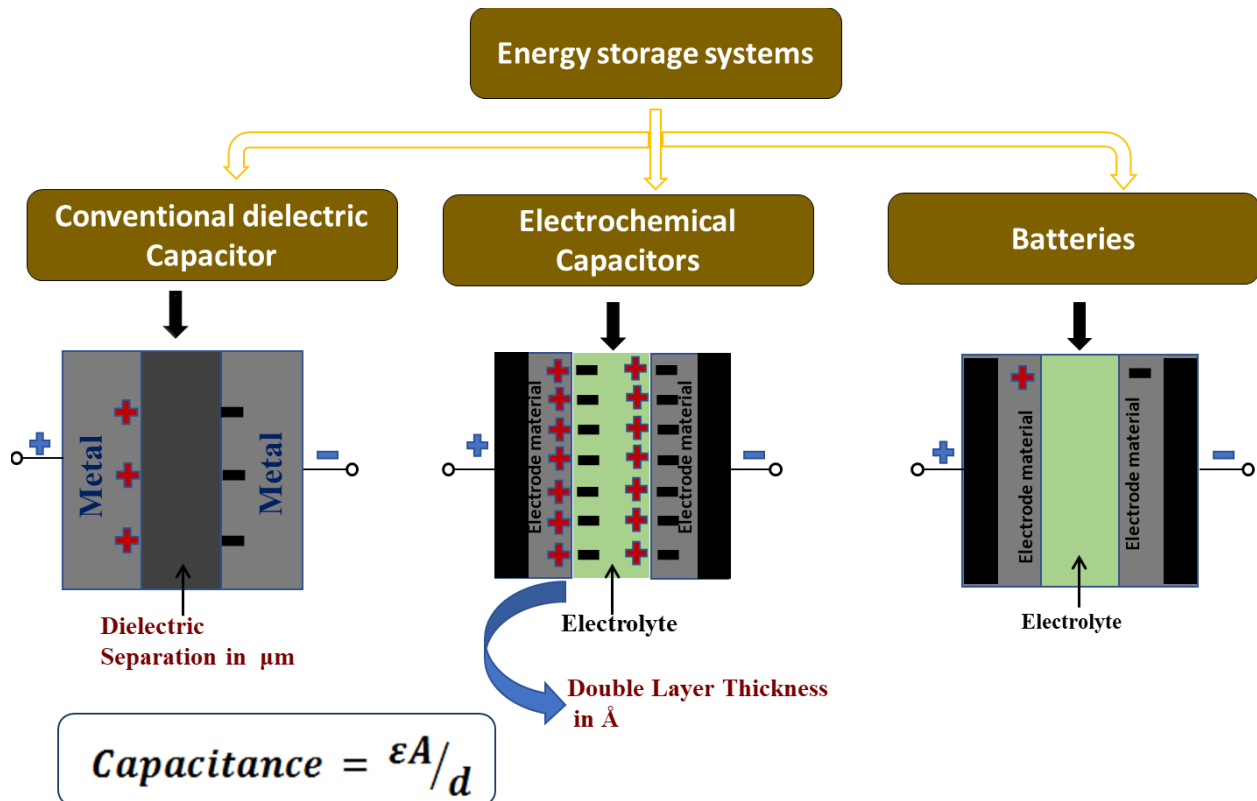


Figure 5. Classification of energy storage devices. (Source: https://commons.wikimedia.org/wiki/File:Fixed_capacitors-charge_storage_principles.png)

✚ Conventional dielectric capacitor:

A conventional dielectric capacitor consists of two parallel metal plates separated by a di-electric medium. The dielectric has a specific di-electric constant. On application of potential difference, the molecules forming the dielectric medium get polarized and the charge gets stored in either of the metal plates. The capacitance is given by the above-mentioned equation where epsilon is the

molar extinction coefficient, A is the area of the electrode and d is the distance between the two electrodes.¹

✚ Electrochemical capacitors:

Electrochemical capacitors also consist of two electrodes which are separated by an electrolyte. Application of potential difference helps the electrolyte salts get ionized and thereby the charges get stored in the surface of the electrode materials either via surface storage or via surface faradic reactions. Based on the charge storage mechanisms, electrochemical capacitors can be classified into three categories which include electrical double layer capacitors (EDLC), hybrid supercapacitors and pseudocapacitors.¹ Figure 6 shows the classification of the supercapacitors

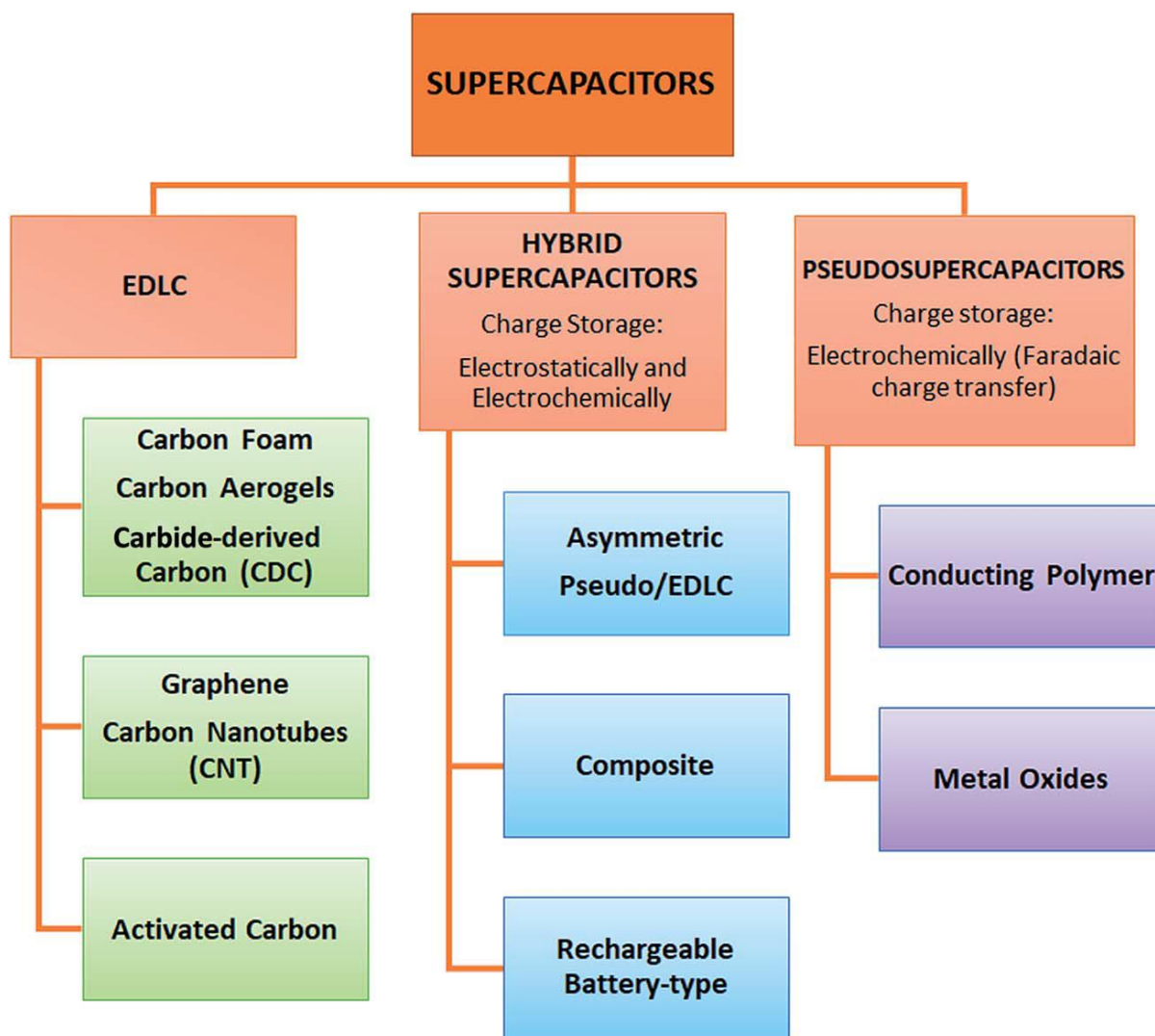


Figure 6. Classification of supercapacitors (Source: Nanoscale Adv., 2019, 1, 2818; Adopted with permission)

✓ **Electrochemical double layer capacitors:**

It uses porous materials on the electrode. Charges get stored in the pores of either of the electrodes (surface storage) on applications of potential difference and the capacitance is given by the following equation.¹

$$C = (\epsilon_0 \times \epsilon_r \times A)/d,$$

A is the surface area of the electrode, ϵ_r is the relative permittivity of the dielectric, ϵ_0 is the permittivity of the free space, d is the distance between the electrodes having opposite bias.

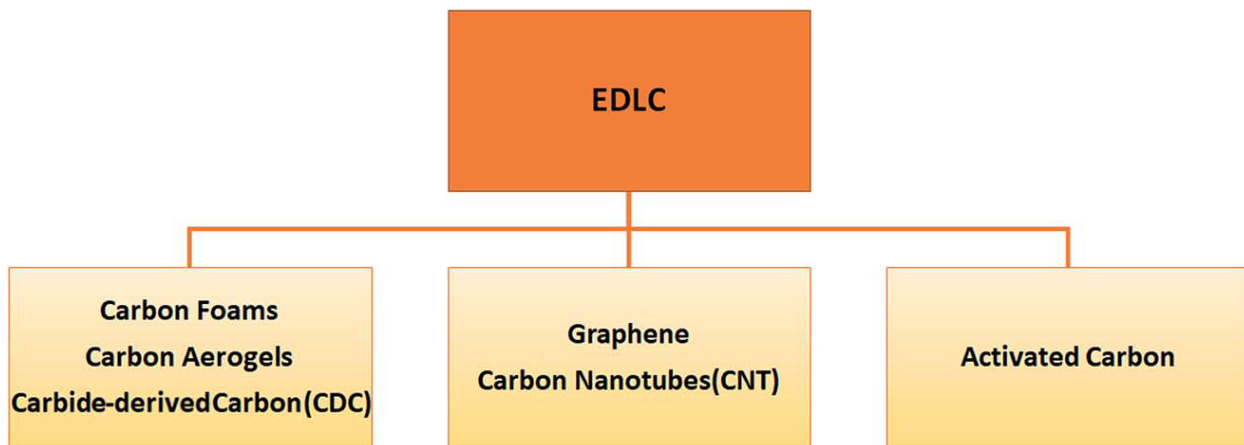


Figure 7. Classification of the EDLCs (Source: Nanoscale Adv., 2019, 1, 2819; Adopted with permission)

✓ **Hybrid supercapacitors:**

These are based on the utilization of non-polarizable electrodes (e.g. metal or conducting polymer) and polarizable electrodes (e.g. carbon) to store the charges. These categories thereby use both non-faradaic and faradic processes. They stand tall in terms of energy density and cost compare to that of the electrical double layer capacitors while the power density might have a lower value. Their charge storage mechanism can be based on rechargeable battery type, asymmetric pseudo/EDLC type or composite type.¹

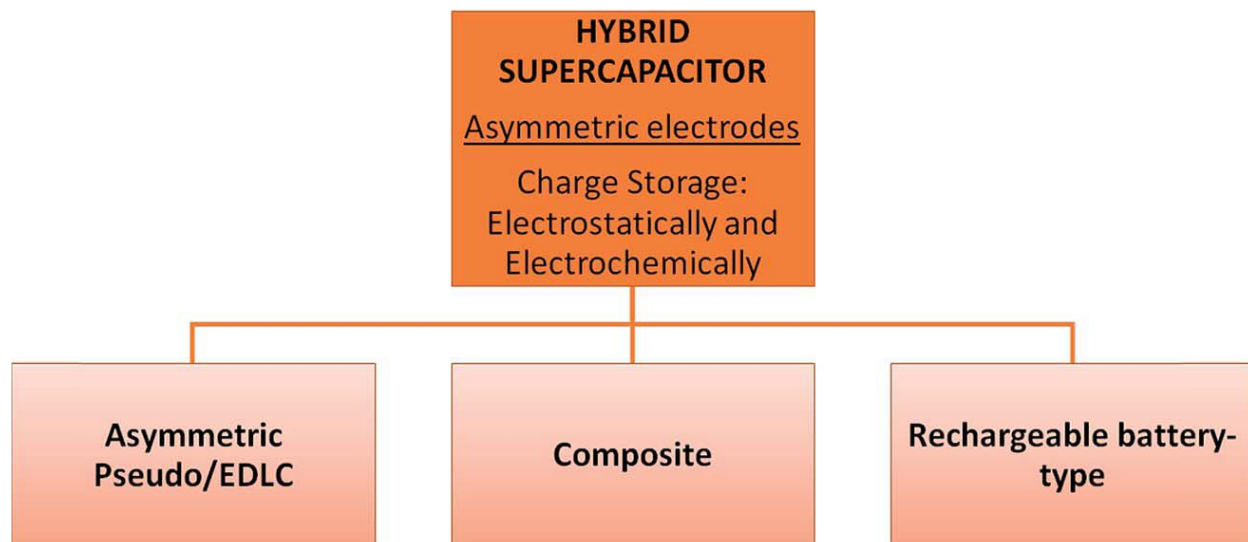


Figure 8. Classification of hybrid supercapacitors based on their working mechanisms/ design. (Source: *Nanoscale Adv.*, 2019, 1, 2821; adopted with permission)

✓ **Pseudocapacitors:**

Charge storage in the pseudocapacitors is based on the faradic reaction of the electrolyte ions with the electrode materials at the electrode-electrolyte interface. In case of pseudocapacitors, while the charges still get stored at the surface of the electrodes like EDLCs there is a faradic (redox) reaction involved in the interface like batteries.¹

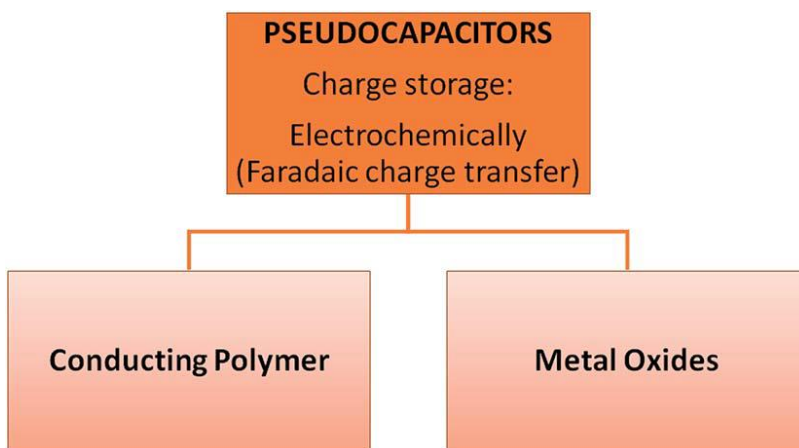


Figure 9. Classification of pseudocapacitors. (Source: *Nanoscale Adv.*, 2019, 1, 2820; adopted with permission)

Batteries:

When one or more than one interconnected electrochemical cell provides a current at a given voltage for a fixed time Δt , it is called a battery.²

Hence for a battery, two of the most important parameters are:

- Output current, I
- Time required for the depletion of the total stored energy, Δt .

These can be increased either by connecting many cells in parallel or by increasing the area of the electrode.²

Hence, the basic difference of a battery from a capacitor is that, a capacitor will always store charges on the surface of the electrodes irrespective of the chemical processes involved. In contrary a battery will always store charges in the bulk of the electrodes making bulk diffusion an extremely important phenomenon and thereby coming up with higher energy density values compare to a supercapacitor. There are various kinds of batteries reported such as primary batteries which is basically a galvanic cell where the chemical reaction is irreversible making it non-rechargeable. On the other hand, there are secondary batteries which are rechargeable in nature such as Ni-Cd, Pb-acid, Li-ion batteries etc. Ni-Cd batteries use Nickel oxide/hydroxide and metallic Cd as electrodes which deliver a gravimetric specific energy of 40-60 WhKg⁻¹ and works at a nominal voltage of 1.2 V. On the other hand, the working principle of Pb acid battery includes exploitation of PbO₂ and Pb as the two working electrodes with aq. H₂SO₄ electrolyte delivering a specific energy of 35-40 WhKg⁻¹ and the nominal voltage of 2.1 V. The popularity of Li-ion batteries over the other secondary batteries lies in in terms of its nominal voltage (3.6 V using LiCoO₂ as the cathode and graphite as the anode) and specific energy (~230-240 Wh Kg⁻¹) making the overall energy density much higher. It can be increased to a very high extent of Li metal is used instead to LiCoO₂ but that comes up different scale-up challenges like dendrite formation which finally leads to a major safety issue. There are also reports of aqueous and non-aqueous metal air batteries like Z-air, Mg-air, Al-air, Li-air, Na-air etc. which use Oxygen gas as the cathode and the corresponding metals as the anodes. These batteries come up with very high energy density values but come up with a major scalability challenges since these use gaseous cathodes.

Since, this thesis is mostly based on Li-ion batteries, this chapter will provide a broad introduction to the Li-ion battery.

3. Introduction to Li-ion batteries:

A Li-ion electrochemical cell mainly comprises of three major components:

- Anode
- Cathode
- Electrolyte

In the first commercial Li-ion cell, the anode which was being used was graphite and the cathode was LiCoO_2 .²

✓ Working principle:

At the time of discharge, Li ions which are present in the interlayers of LiCoO_2 between the two CoO_6 octahedra are pulled on application of a certain amount of current density. Li-ions travelled through the electrolyte medium across the separator and get intercalated in the graphite layers forming an intercalation Van-der-Waal compound LiC_6 . The separator being electrically insulating, keeps the positive and negative electrodes separate and allows the passage-space for the Li-ions. The electrons flow through the external circuit. The anode and cathode materials are coated on current collectors (e.g. Cu, Al foils etc.) which help in collecting the electrons which passes through the external circuit. At the time of charging, the reverse mechanism takes place. The Li ions start moving from the graphite layers and intercalates again in the LiCoO_2 layers.²

Figure 10 shows a representation of a commercialized Li-ion battery using graphite as anode and LiCoO_2 as cathode. It shows how Li ions move back and forth through the separator via electrolyte medium while charging and discharging.

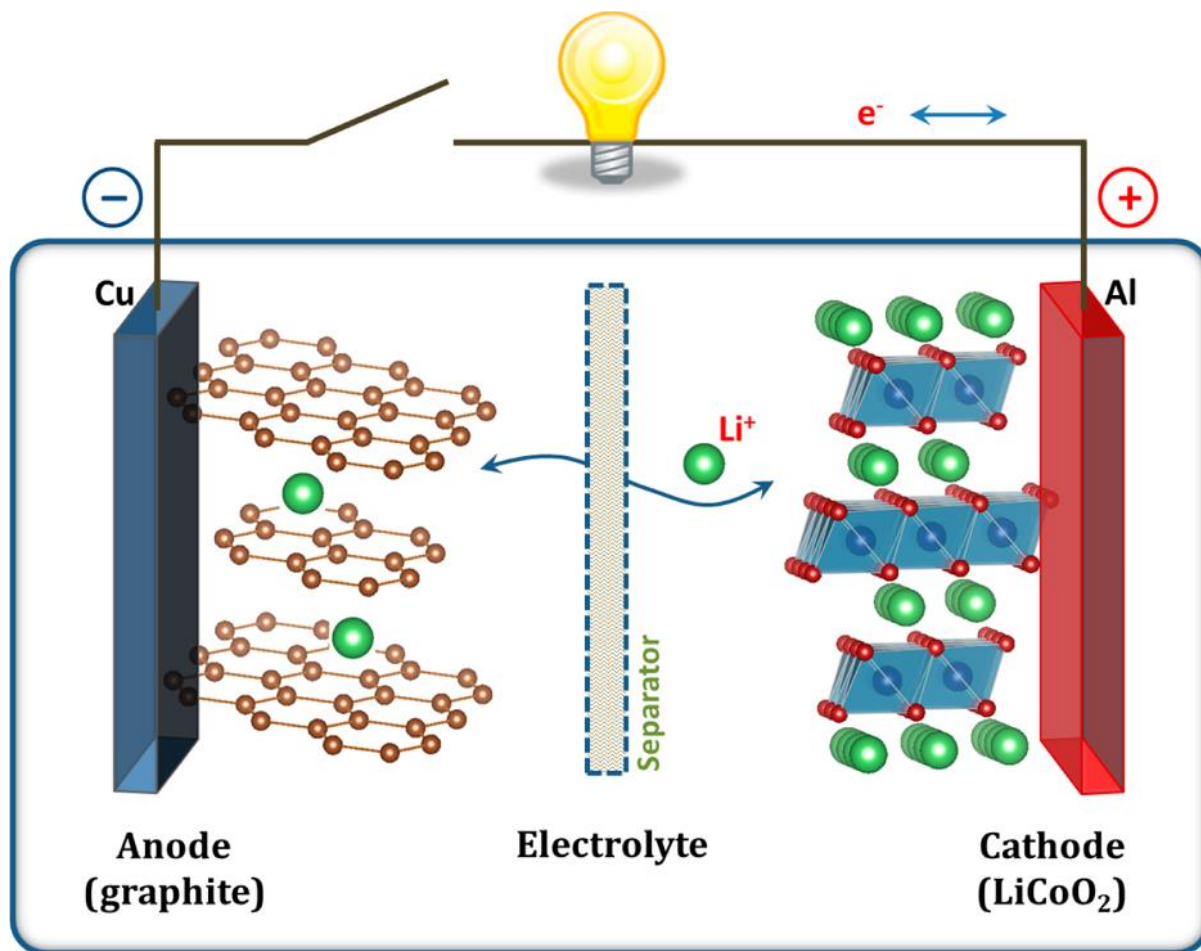


Figure 10. Schematic illustration of the Li-ion battery exploiting graphite as the anode and LiCoO₂ as the cathode. (Source: J. Am. Chem. Soc. 2013, 135, 1167–1176; adopted with permission)

The function of the electrolyte is to conduct the ionic component of the electrode materials (anodes and cathodes) to either of the electrodes while charging and discharging. Since the electronic conductivity of the current collectors (metals) is much higher than the ionic mobility inside the electrolyte, a Li-ion electrochemical cell has large-area electrodes which are separated by a very thin layer of electrolyte.²

The function of the metallic current collectors is to transfer electron (electronic current) from the electrode materials to the external circuit posts.

During charging and discharging, the discharge output voltage of the cell, V_{dis} gets reduced compared to the open-circuit voltage of the fabricated cell, V_{oc} by an involved polarization, η ($\eta = I_{\text{dis}}R_b$) where, R_b is the internal resistance of the cell. This internal resistance, on the other hand, increases the charge output voltage, V_{ch} so as to reverse the charging chemical reaction by an overpotential, $\eta = I_{\text{ch}}R_b$. (2)

$$V_{\text{dis}} = V_{\text{oc}} - \eta(q, I_{\text{dis}})$$

$$V_{\text{ch}} = V_{\text{oc}} + \eta(q, I_{\text{ch}})$$

q is the state of charge (SOC). The % efficiency or of a Li-ion cell for storing the energy at a given current, I , is:

$$100 \times \frac{\int_0^{Q_{\text{dis}}} V_{\text{dis}}(q) dq}{\int_0^{Q_{\text{ch}}} V_{\text{ch}}(q) dq}$$

$$Q = \int_0^{\Delta t} I dt = \int_0^Q dq$$

Q is the total specific charge (per unit volume, WhL^{-1} or per unit mass, WhKg^{-1}) which is transferred (stored) by current, I . ($I = dq/dt$)

$Q(I)$ is the cell capacity at a specific I .

Electrode-electrolyte interfacial ions transfer has a diffusion and capacitive contribution. At high current, it becomes diffusion controlled and thereby Q has a dependence on I .

For the Li-ion battery, the charge-discharge efficiency, known as the Coloumbic efficiency is an extremely important parameter because it determines the reversibility of the cell. It basically signifies the number Li ions moving to and fro while charging and discharging.²

The irreversible/reversible Li loss can occur due to many reasons as follows:

- ✓ Diffusion limited loss (Li insertion at a high charging/discharging rate; reversible capacity loss)
- ✓ Decomposition of the electrode materials (Irreversible capacity loss)
- ✓ Electrode-electrolyte chemical reaction (Irreversible capacity loss)
- ✓ Formation of the solid-electrolyte interphase (SEI) layer (Irreversible capacity loss)

The % Coloumbic efficiency of each cycle (Associated with the mentioned capacity fading) is given by:

$$100 \times \frac{Q_{\text{dis}}}{Q_{\text{ch}}}$$

The cycle life of a Li-ion full battery is a very important parameter. Once the cell comes to 80 % of its primary capacity, it is commonly considered as the end point of its cycle life. Gravimetric and volumetric energy densities are also extremely important beside the cost and the cycle-life of the battery. The output power of the battery, $P(q) = V(q)I_{\text{dis}}$ (I = discharge current) is also of significant importance.²

The energy stored in a fully charged cell can be obtained by calculating the time Δt (I_{dis}) at the fully discharge state at a given I ($I_{\text{dis}} = dq/dt$)

$$\text{energy} = \int_0^{\Delta t} IV(t)dt = \int_0^Q V(q)dq$$

The other important parameter is the tap density of the battery. Tap density basically means the density of a given material when poured into a cylinder after tapping. It actually reflects in the gravimetric capacity or the gravimetric energy density. If more material can be packed in smaller amount of area having a better tap density, it gets reflected in the gravimetric capacity and energy density.²

4. Materials for Li-ion batteries:

To design a state-of-the-art Li-ion battery, there are some important parameters which are of major concern:

- ✓ Availability in the earth crust (This is also one of the most important parameters which determines the cell cost).
- ✓ Specific capacity and specific energy density.
- ✓ Cyclic stability.

Hence, thus far, a tremendous amount of effort has been employed on designing novel high-performance electrode which can stand tough in terms of parameters like specific capacity, rate performance and cycle life.³

Figure 11 and figure 12 talk about the availability and charge capacities for the potential Li-host elements.

Availability

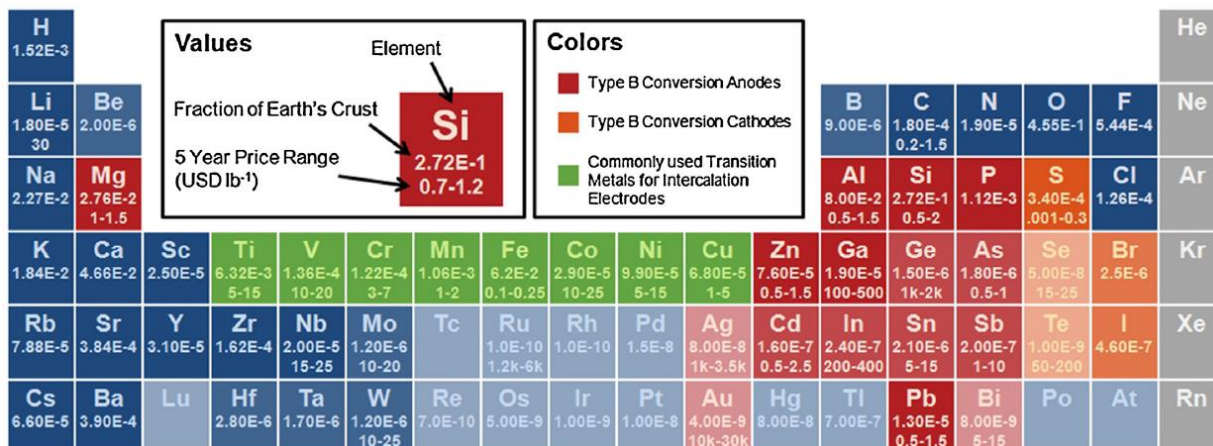


Figure 11. Availability of the potential Li-host elements. (Source: Materials Today, Volume 18, Number 5, June 2015; adopted with permission)

Charge capacity

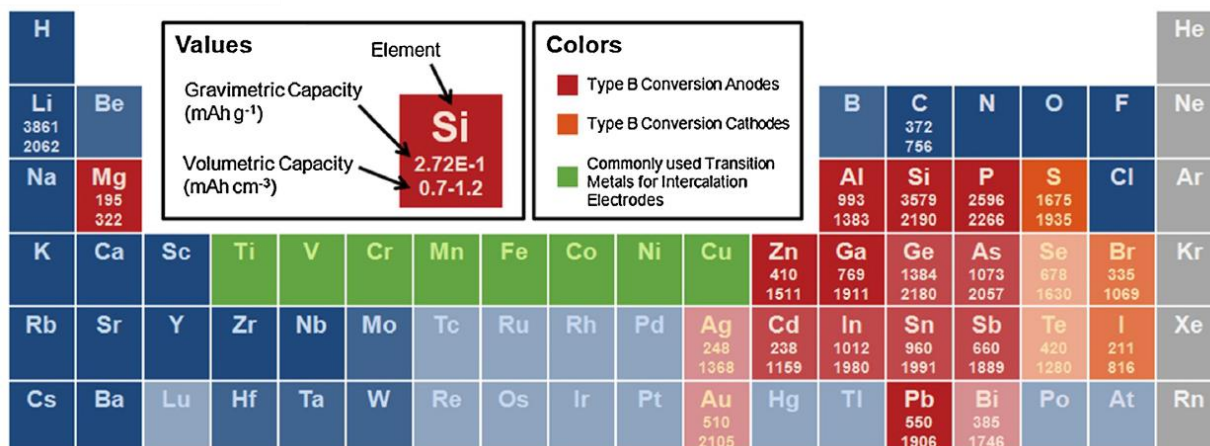


Figure 12. Charge capacity of the potential Li-host elements. (Source: Materials Today, Volume 18, Number 5, June 2015; adopted with permission)

Figure 11 shows the whole price in USD the earth abundance of the materials and figure 12 puts light on both gravimetric (mAh g⁻¹) and volumetric capacity (mAh cm⁻³).

This thesis will discuss about both the anodic and cathodic material for Li-ion battery in detail.

4.1. Potential anode materials for Li-ion batteries:

4.1.1. Intercalation Anode materials:

Initial batteries employed Li metal as the source of lithium in Li-ion batteries. However, the Li metal has problem of forming dendrite which can eventually short the cell which can lead to a thermal run-away reaction. Hence, using Li metal battery is extremely problematic although Li can theoretically provide extremely good specific capacity and energy density. Here comes the importance of a good anode material which can perform in several parameters like capacity, energy density, rate performance, stability and cost. Below discussions are based on various categories of materials which are used as the potential anode materials for Li-ion batteries.⁴⁻⁹

✚ Graphitic and other carbonaceous anodes:

Graphite is being commercialized as Li-ion battery anode from more than 20 years ago and still is the most preferred anode. The Li-ion storage in most of the carbonaceous materials (unless it has any redox active functionality) remains almost the same. These materials store Li ions via intercalation mechanism by forming a Van-der-Waal compound LiC_6 . Their theoretical capacity becomes limited since 6 C atoms are required to store 1 Li atom. Yet, they are sought out due to their high electrical conductivity, very low lithiation-delithiation volume change, high earth abundance, low cost, extremely low working potential (Hence can obtain a wide potential window with a moderately high voltage cathode), high Li diffusivity, high cycle life, power density, moderate energy density. Instead of this advantage graphite still lacks in terms of volumetric capacity which is somewhere between 330 to 430 mAhcm^{-3} .^{3,10}

Broadly, carbon-based materials can be classified in two categories of graphitic carbon and hard carbons and both have their pros and cons. Graphitic materials have large grains and has the potential to achieve close to theoretical capacity. However, it does not have a good friendship with Propylene carbonate (PC can wonder in terms of Li diffusion and has low melting temperature). PC has a tendency to intercalate into the graphite layer along with Li^+ . On the other hand, hard carbons have disordered orientation and small grains which reduces the volume expansion. But these do have a problem of forming high quantity of SEI layer due to randomly oriented planes.¹¹⁻¹⁷

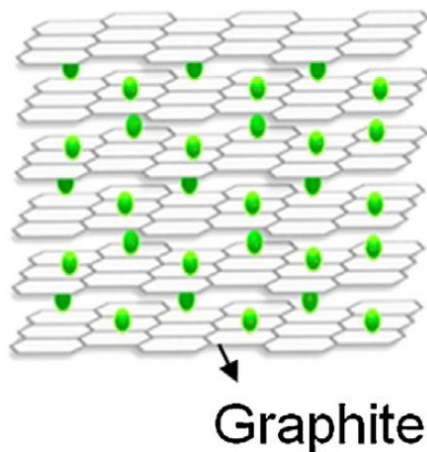


Figure 13. Lithiated graphite (Source: ACS Appl. Mater. Interfaces 2014, 6, 10892–10899; adopted with permission).

✚ Lithium titanium oxide (LTO/ $\text{Li}_4\text{Ti}_5\text{O}_{12}$):

Along with graphite, LTO is also a commercialized anode. The pros and cons of LTO is discussed below.¹⁸

❖ Pros:

- ✓ High rate capability.
- ✓ High cycle life.
- ✓ High volumetric capacity.
- ✓ Extremely low change in the volume with constant lithiation and de-lithiation

❖ Cons:

- ✓ High cost.
- ✓ High working potential (Lower potential window when used in the full cell)

LTO is known as the “zero strain” insertion anode since it shows an extremely less volume expansion of 0.2% with lithiation and de-lithiation.¹⁹⁻²¹

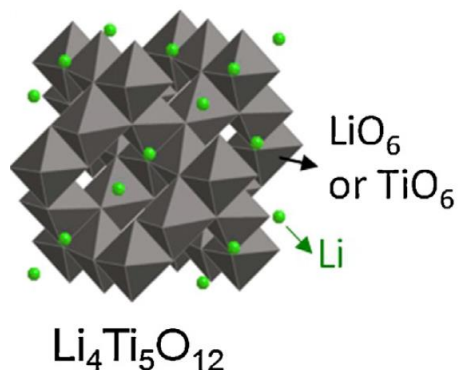


Figure 14. shows the crystal structure of LTO and the Li stored (Source: Cryst. Growth Des. 2011, 11, 4401–4405; adopted with permission).

One of the important advantages of using LTO as the anode is that since it works at a high voltage (1.55 V), the formation and growth of the SEI layer in the anode-electrolyte interface can be largely avoided. Also, its high working potential prevents the formation of dendrite to a significant extent.²²⁻²⁶ People have done researches on doping of LTO with Ca, Al, Zr etc or making a composite LTO anode with different carbonaceous additives so as to increase its

gravimetric capacity and power density. As for example, LTO/CNT/graphene composite shows a capacity of $\sim 170 \text{ mAhg}^{-1}$ at 0.2C. On the other hand, Ca^{2+} and Zr^{2+} doped LTO come up with capacity values of $\sim 155 \text{ mAhg}^{-1}$ at 0.1 C. However, these doping or composite systems are not of much importance in terms of increasing the specific capacity and thereby increasing the overall energy density of the battery.³

4.1.2. Alloying materials:

There are some materials which stores Li via formation of reversible Li alloy, are referred to the “Alloying materials.”

The alloying materials like Si, Sn, Ge, Sb etc. are of very high research interest because of their extremely high theoretical capacity and low cost. But they are still not commercialized because of their association with severe volume expansion upon lithiation and thus losing the contact with the current collector by pulverizing the electrode. This severe volume changes can potentially destroy the SEI layer and can hamper the facile Li diffusion pathway and increasing cell impedance. Heavy research is going on to stabilize the SEI layer by encapsulation the material with some carbonaceous material so as utilize the void space and to provide the space for volume expansion.

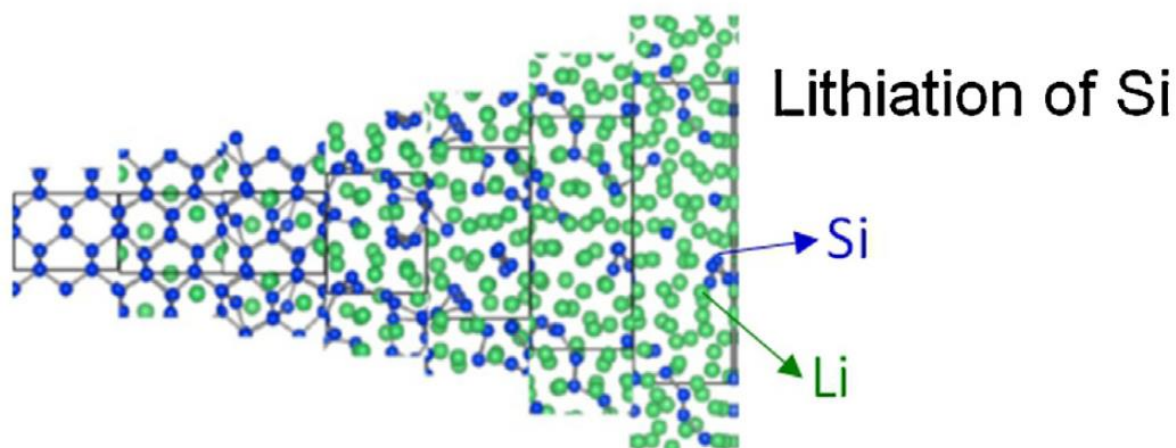


Figure 15. Structure of Si during lithiation. (Source: Materials Today, Volume 18, Number 5, June 2015; adopted with permission).

Among the various alloying materials Si has gain the highest research interest because of its highest theoretical capacity ($\sim 4200 \text{ mAhg}^{-1}$ by formation of $\text{Li}_{22}\text{Si}_5$ alloy) in the lot. Then again, along with the volume expansion, there are a number of other issues with Si anode such as poor material conductivity, repeated chemical reaction with the electrolyte, high irreversible capacity loss, and fast capacity fade. Therefore, a number of very interesting and innovative strategies have been designed and employed in recent years to stabilize the high capacity of Si; the primary ones being the use of carbon materials as elastic conducting additives in the form of composites or coatings, as discussed at length in multiple significant contributions by Y. Cui and co-workers, Y. Sun and co-workers, and many others. In some cases, these strategies are synthetically quite complex, while in other cases the use of larger weight fraction of carbon concedes the high capacity advantage of silicon, because carbon in itself is an ineffective material (capacity $300\text{-}400 \text{ mAhg}^{-1}$) in the capacity context.²⁷⁻³¹

Several research groups have tried to stabilize the Si anode by optimizing the binders as well. Poly(vinylidene fluoride), PVDF, being the most widely used binders for Li ion battery electrode preparation. However, its fair thermal and electrochemical stability makes it not so popular in the context of Si anode since its elasticity is less. Thus, capacity fade results even after 8-10 charge discharge cycles due to formation of protective solid electrolyte interphase (SEI) layer in the subsequent cycles. Hence several research groups have come up with different binders like styrene butadiene rubber (SBR), sodium carboxymethyl cellulose (CMC), cross linked polymer binder like Poly(acrylic acid), PAA-CMC composite where large numbers of -OH and -COOH groups render very strong and stable covalent bond and/or hydrogen bonding interaction with oxide layers grown on the Si nanoparticles, thus giving stability and preventing the electrode from further pulverization.³¹

Even, non-carbon conductive alternatives which could either be effective in minute quantities in accommodating the stresses and/or could concurrently contribute through their own high Li ion storage capacity have also been researched, and innovative strategies based on the use of Si-X compounds like SiO_2 , SiO , CaSi_2 , Mg_2Si etc. have shown a good promise in this regard.³¹

Sn is also of high research interest but suffers from similar issues like Si. Sn forms a Li_xSn alloy which delivers a capacity of $\sim 850\text{-}950 \text{ mAhg}^{-1}$ which also provides a huge volume expansion and thereby leading to capacity fading.³²

There are some other alloying materials like Zn, Cd, Pb, Al etc. which are of significant research interest because of their low cost. But these materials lack in terms of gravimetric although these have high volumetric capacity.³³

P and Sb are also being researched since these have a fair capacity but are far away from getting commercialized because of their toxic nature. Also, their de-lithiation potentials are relatively high which results in a voltage hysteresis.^{34,35}

4.1.3. Conversion materials:

Conversion materials are being referred to those materials which form reversible conversion product upon lithiation. Most common conversion materials are oxide based where Li_2O is formed as the conversion reaction product. These conversion materials, although have relatively high capacity, suffer from very high voltage hysteresis and sluggish kinetics. Since Li is highly electropositive, it has a very strong interaction with the highly electronegative O atom thus making the Li_2O as a very stable compound. Hence the energy required to break the Li_2O bond is much higher compare the energy gained by the formation of the Li_2O bond. This in-turn results in a very high voltage hysteresis and a very low energy efficiency of the cell.³

Figure 16 shows the charge-discharge profiles of different anode materials.

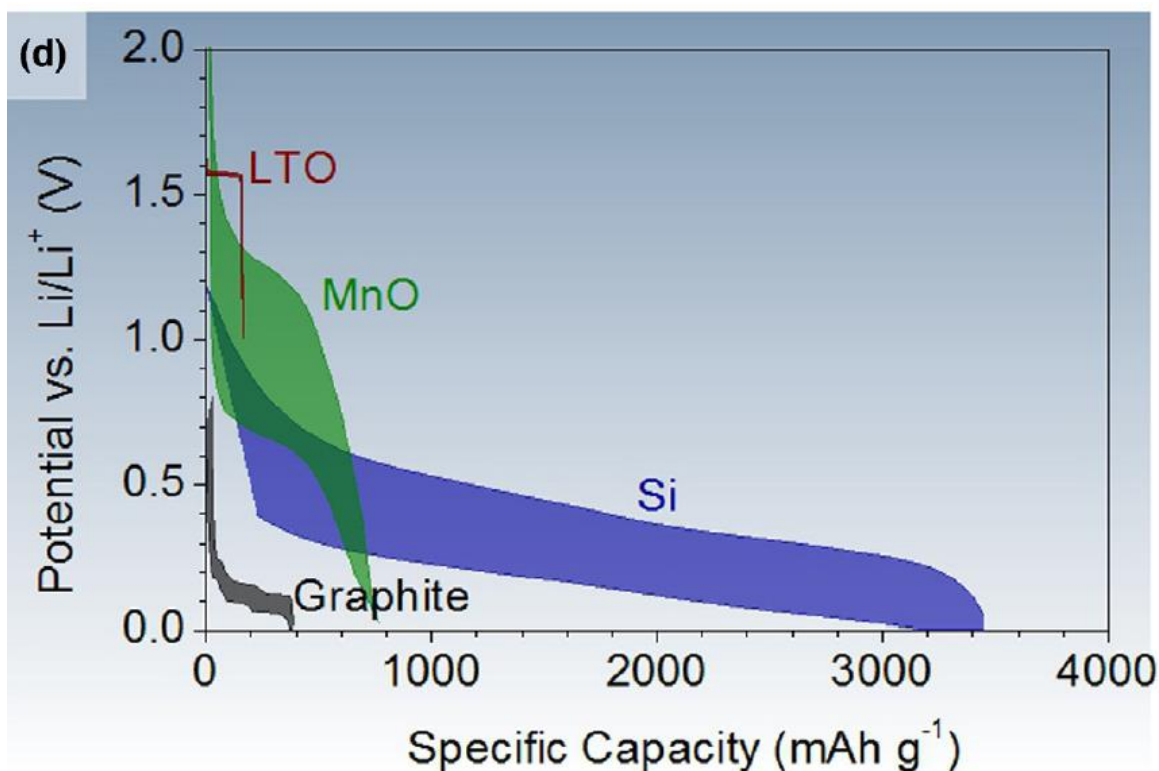


Figure 16. Charge-discharge profiles of different commonly used anode materials. (Source: Materials Today, Volume 18, Number 5, June 2015; adopted with permission).

Table 1 discusses about some important characteristic parameters of the commonly used anode materials such as lithiation and de-lithiation potential, diffusion co-efficient (which is the measure of the fast or slow kinetics of the anode) and the associated volume change on constant lithiation and de-lithiation.

Properties of some commonly studied anode materials.				
Material	Lithiation potential (V)	Delithiation potential (V)	D ($\text{cm}^2 \text{s}^{-1}$)	Volume change
Graphite	0.07, 0.10, 0.19	0.1, 0.14, 0.23	10^{-11} – 10^{-7}	10%
LTO	1.55	1.58	10^{-12} – 10^{-11}	0.20%
Si	0.05, 0.21	0.31, 0.47	10^{-13} – 10^{-11}	270%
Ge	0.2, 0.3, 0.5	0.5, 0.62	10^{-12} – 10^{-10}	240%
Sn	0.4, 0.57, 0.69	0.58, 0.7, 0.78	10^{-16} – 10^{-13}	255%
Li_2O (amorphous)	N/A	N/A	5×10^{-12} – 5×10^{-10}	N/A

Table 1. Properties of some commonly used anode materials (Source: Materials Today, Volume 18, Number 5, June 2015; adopted with permission).

4.2. Potential cathode materials for Li-ion batteries:

4.2.1. Intercalation cathode materials:

Intercalation cathode materials are mainly known as those compounds which consists of a solid host network which can accommodate guest ions. The hosting of guest ions in these systems occurs via a complete reversible fashion. In case of Li-ion batteries, the guest mainly consists of different transition metal oxides, various polyanionic compounds, metal chalcogenides. These materials can have various crystal structures like spinel, olivine, layered, tavorite etc. Figures 17 and 18 show the crystal structure and the charge-discharge profiles of the various intercalation cathodes.³⁶⁻⁴²

Layered structures are most common in this lot. NbSe_3 and TiS_3 were among the earliest investigated the layered intercalation cathodes. The reversibility in case of NbSe_3 was far better compare to TiS_3 (On lithiation, TiS_3 goes to octahedral from trigonal prismatic).⁴³

Afterwards a ternary chalcogenide LiTiS_2 (LTS) was commercialized by Exxon owing to its high gravimetric capacity, high energy density and high cyclic stability (>1000 cycles).^{44,45}

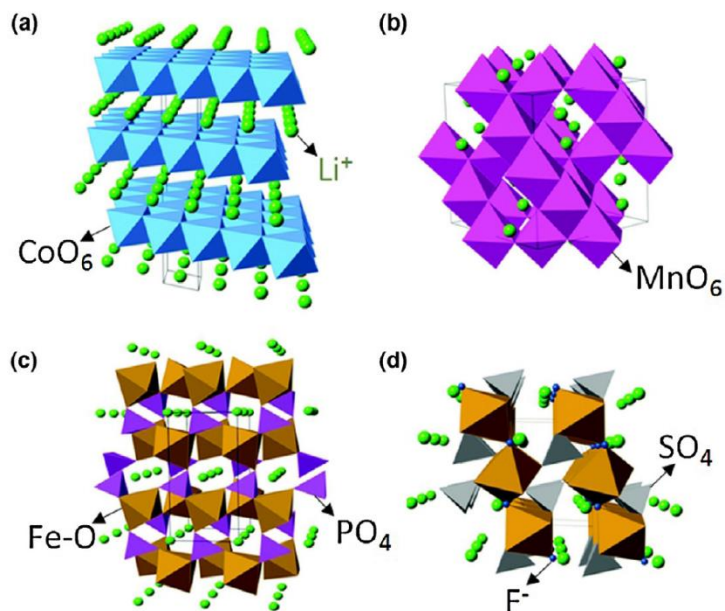


Figure 17. Crystal structure of various intercalation cathodes. (a) LiCoO_2 (layered) (b) LiMn_2O_4 (spinel) (c) LiFePO_4 (olivine) (d) LiFeSO_4F (tavorite) (Source: Materials Today, Volume 18, Number 5, June 2015; adopted with permission).

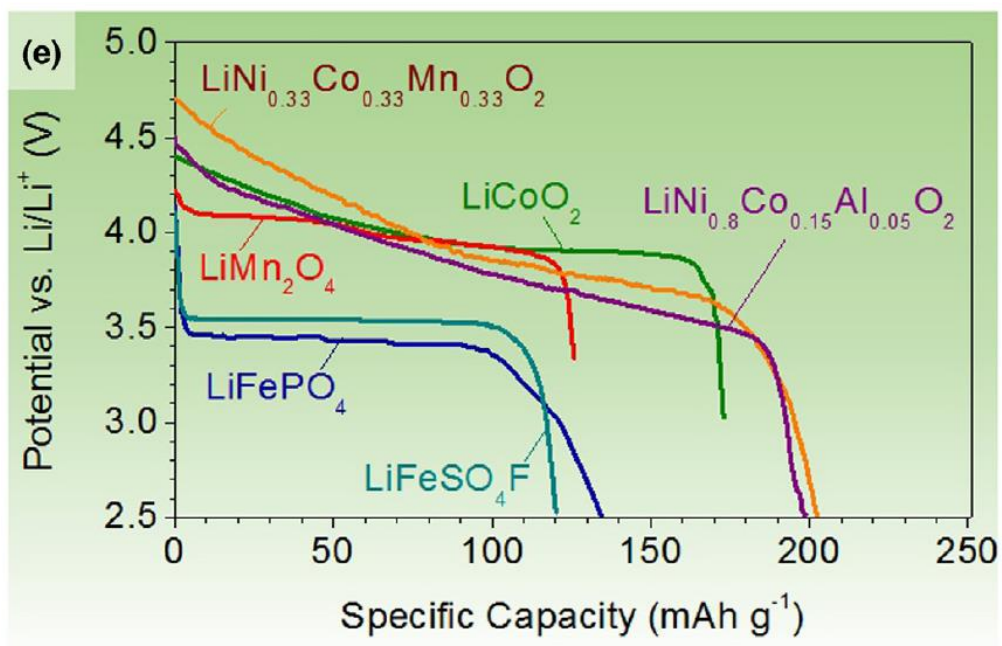


Figure 18. Charge-discharge profiles of the intercalation cathodes (Source: Materials Today, Volume 18, Number 5, June 2015; adopted with permission).

✚ Transition metal oxides:

The most commonly used and the first commercialized transition metal oxide cathode was LiCoO_2 (LCO). The material was first introduced by Prof. John B. Goodenough.⁴⁶ LCO is an extremely popular cathode. The advantages of LCO are⁴⁷

- ✓ Very high theoretical gravimetric and volumetric capacity $\sim 274 \text{ mAh g}^{-1}$ and 1363 mAh cm^{-3} respectively.
- ✓ High discharge voltage ($\sim 3.7 \text{ V}$).
- ✓ Very low self-discharge rate.
- ✓ Good cyclic stability.

Instead of its numerous benefits which led to its commercialization it suffers from some severe disadvantages which are as follows.⁴⁸

- ✓ Low thermal stability.
- ✓ Poor rate capability (At high current or with deep cycling it shows a fast capacity fade).
- ✓ Very high cost (Because of the use of Co).

Although the theoretical capacity of LCO is $\sim 274 \text{ mAh g}^{-1}$ (Taking into consideration the pulling of 100% of the Li atoms from the interlayer sandwiched between the two consecutive CoO_6 octahedra) it is very hard to achieve a practical capacity of more than 150 mAh g^{-1} because of its structural limitations. When more than 50% of Li comes out of the system there is a very strong electronic repulsion between the P orbitals of the O atoms between the consecutive CoO_6 octahedra. This leads to an irreversible phase transformation of the layered structure and thereby the whole crystal structure collapses.³

Also, when LCO is heated above a certain temperature the O atoms get released from the crystal structure via an exothermic reaction which leads to thermal runaway reaction making LCO a thermally less stable system. This is a major concern of the Li-ion battery industry.⁵⁰

Various strategies have been employed to stabilize the structure of the LCO so as to take more Li out from the interlayer without changing the crystal structure.

- ✓ Some strategies include doping of various elements Mn, Cr, Fe, Ni, Al etc. Mn has various oxidation state ranging from +II to +VII which can aid to increase the capacity. When Li is pulled out from the interlayer, the metal has to get oxidized where Mn can contribute much better compare to Co owing to its variable oxidation states. On the other hand, Ni³⁺ to Ni⁴⁺ has a very high redox potential which can in-turn increase the overall potential window of the Li-ion full battery and thereby increasing the overall energy density (LiNi_{0.5}Mn_{0.5}O₂ delivers a specific capacity of ~180 mAhg⁻¹) Al on the other hand can increase the thermal stability of the system.⁵⁰
- ✓ Other strategies include coating of different oxides like ZrO₂, B₂O₃, Al₂O₃, TiO₂ etc. which are beneficial in terms of enhancing the stability and reducing the chances of side reactions of the cathode material with the electrolyte.^{51,52}

LiNiO₂ is also a cathode of very high research interest because of its similar high gravimetric capacity of ~275 mAhg⁻¹ and high working potential. But it has various shortcomings one of which includes the migration of Ni²⁺ ions in the Li layer. It is very hard to maintain Ni³⁺ all throughout the structure even under flowing Oxygen atmosphere. Now, since Ni²⁺ and Li⁺ has very similar ionic radii (69 pm for Ni²⁺ and 72 pm for Li⁺) Ni²⁺ always has tendency to irreversibly migrate to the Li layer from the transition metal layer when Li is pulled during charging process. This essentially leads to collapse of the structure.⁵³

Finally, after many years of research, people have could come up with two interesting cathode systems (discussed below) which are commercialized. Even these cathodes suffer leave some drawbacks but on the whole their performance parameters are satisfactory for commercialization.

- ✓ **LiNi_xCo_yAl_zO₂ (NCA):** Lithium Nickel Cobalt Aluminum Oxide (NCA) is a very popular cathode. Depending on the values of x, y and z, NCA can have various different stoichiometry. The famous-most composition of NCA is LiNi_{0.8}Co_{0.15}Al_{0.05}O₂. Because of its high discharge capacity (~200 mAhg⁻¹) and extremely good cyclic performance, it is now commercialized and is used in Panasonic batteries designed for TESLA EVs.³
But the shortcoming still remains in terms of thermal stability due to the growth of SEI layer at high temp (50-70⁰C) leading to growth of micro cracks at the grain boundaries.^{54,55}

- ✓ **LiNi_xCo_yMn_zO₂ (NCM aka NMC):** Lithium Nickel Cobalt Manganese oxide is also another heavily researched cathode. Same as NCA, x, y and z can take different values in NMC. LiNi_{0.33}Co_{0.33}Mn_{0.33} is the most common form of NMC. Besides, LiNi_{0.68}Co_{0.18}Mn_{0.18} and LiNi_{0.46}Co_{0.23}Mn_{0.31}O₂ are also possible.⁵⁶ Depending on the composition, the specific capacity of the NMC varies in the range of 180-200 mAhg⁻¹. Like NCA, NMC also has high working potential owing to the presence of Ni. NMC has a better thermal stability compare to NCA.⁵⁶

Figure 18 describes the various potential strategies which can be employed to stabilize the cathode structure.

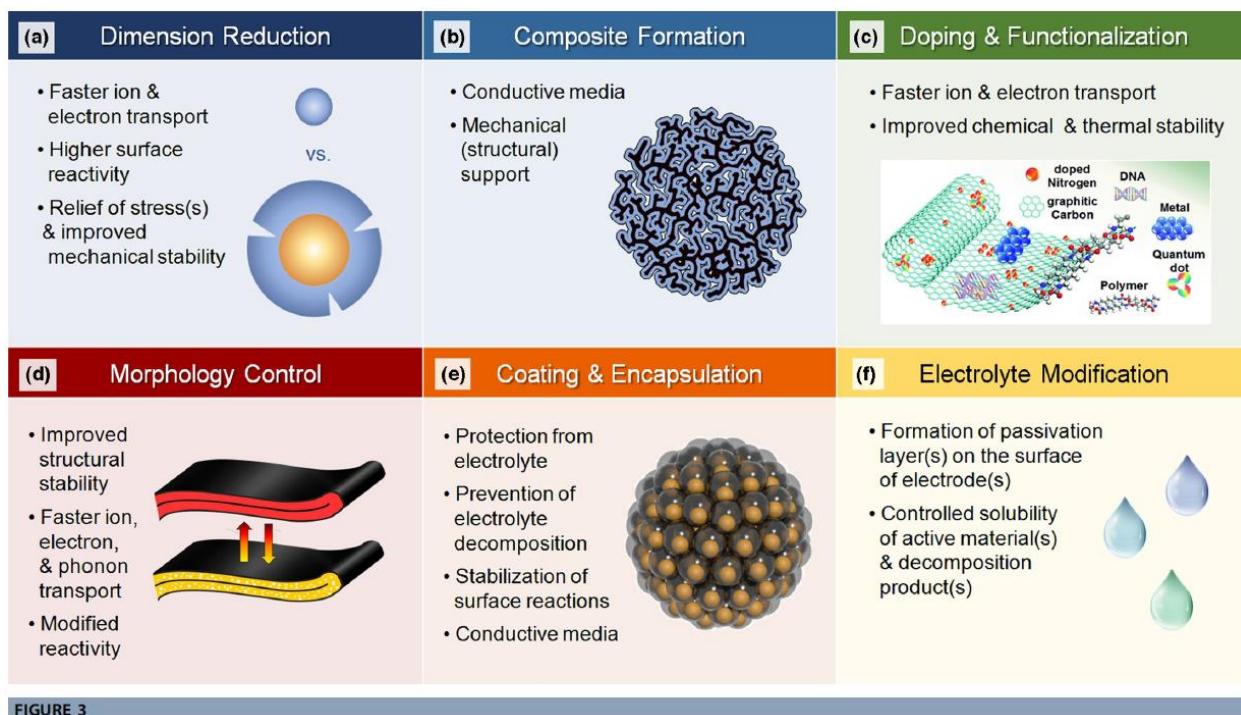


Figure 18. General strategies to improve the performance parameters for the cathodes. (Source: Materials Today, Volume 18, Number 5, June 2015; adopted with permission).

✚ Polyanionic compounds:

Intercalation cathode materials also include a special class of compounds which is known as the polyanionic compounds. In these cases, the counter anions are polyanions instead of a monoanion like oxide or sulfide. The polyanions can be described by a general formula, $(XO_4)^{3-}$ where X can be S, Si, P, Mo, As, W etc. Polyanionic compounds have relatively high working potential due to very strong bonding between the metal and polyanion.³ The overall stability also thus gets very high. Polyanionic compounds are mostly stabilized in the Olivine and the Tavorite structures.⁵⁸

LiFePO₄ (LFP) is the most common polyanionic compound having the Olivine structure. Li⁺ and Fe²⁺ are located at the octahedral sites and P occupies the tetrahedral sites and the overall lattice becomes distorted hexagonal close-packed. LFP stands really tall in terms of high rate capability and superior thermal stability but leaves shortcomings of low working potential (figure 14) along with poor ionic and electronic conductivity. Several researches which are done to understand the structure and to increase the performance majorly include carbon coatings and cation doping. Instead of these drawbacks, LFP is successfully commercialized owing to its low cost and high thermal stability.⁵⁸

LiFeSO₄F is a polyanionic compound having the Tavorite structure which delivers a specific

Characteristics of representative intercalation cathode compounds; crystal structure, theoretical/experimental/commercial gravimetric and volumetric capacities, average potentials, and level of development.					
Crystal structure	Compound	Specific capacity (mAh g ⁻¹) (theoretical/experimental/typical in commercial cells)	Volumetric capacity (mAh cm ⁻³) (theoretical/typical in commercial cells)	Average voltage (V)	Level of development
Layered	LiTfS ₂	225/210	697	1.9	Commercialized
	LiCoO ₂	274/148/145	1363/550	3.8	Commercialized
	LiNiO ₂	275/150	1280	3.8	Research
	LiMnO ₂	285/140	1148	3.3	Research
	LiNi _{0.33} Mn _{0.33} Co _{0.33} O ₂	280/160/170	1333/600	3.7	Commercialized
	LiNi _{0.8} Co _{0.15} Al _{0.05} O ₂	279/199/200	1284/700	3.7	Commercialized
	Li ₂ MnO ₃	458/180	1708	3.8	Research
Spinel	LiMn ₂ O ₄	148/120	596	4.1	Commercialized
	LiCo ₂ O ₄	142/84	704	4.0	Research
Olivine	LiFePO ₄	170/165	589	3.4	Commercialized
	LiMnPO ₄	171/168	567	3.8	Research
	LiCoPO ₄	167/125	510	4.2	Research
Tavorite	LiFeSO ₄ F	151/120	487	3.7	Research
	LiVPO ₄ F	156/129	484	4.2	Research

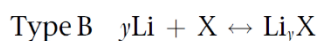
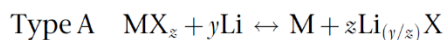
capacity of 151 mAh g⁻¹ and does not need carbon coatings to gain extra stability.⁵⁹

Table 2. Characteristics of different intercalation cathode compounds (Materials Today, Volume 18, Number 5, June 2015; adopted with permission)

4.2.2. Conversion cathode materials:

Conversion cathode materials are also of very high research interest because of the very high theoretical specific capacity.⁶⁰⁻⁶⁸

Solid-state redox reactions occur in case of conversion cathodes which can be described as follows:



Type A mainly include metal halides which comprise of high valance ions which can provide high theoretical capacities. A common fluoride-based conversion cathode is FeF_2 . The F ions diffuse through the FeF_2 molecule and it forms LiF reacting with Li owing to the higher mobility of F ions. Fe with higher size and lower mobility remains behind it. Figure 20 describes this phenomenon.³

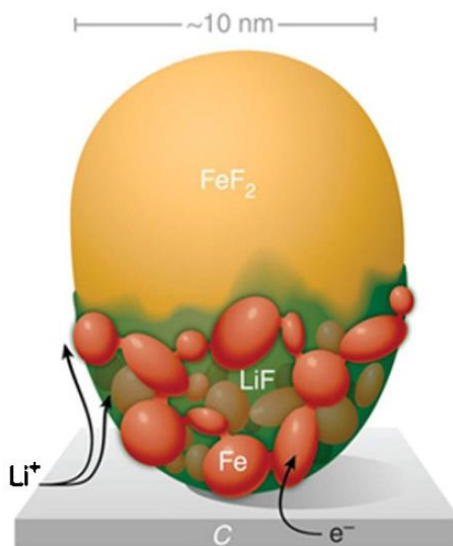


Figure 20. The schematic pathway of the working mechanism of FeF_2 conversion cathode. (Source: F. Wang, et al. Nat. Commun. 3, 2012, 1201; adopted with permission.)

But the major shortcomings are the voltage hysteresis and the cyclic stability. Since, LiF is the formed conversion compound which is extremely stable owing to a hard-hard combination

between Li and F, the reversibility of these materials is very poor. Also, this leads to very high voltage hysteresis and thereby significantly poor energy efficiency.⁶⁹

Type B majorly include compound elements like S, O, Se, I and Te. S has a very high theoretical gravimetric capacity of 1675 mAh g⁻¹ (ref). In fact, Li-S battery is a super-hot area of research not only because S has a very high theoretical capacity but this battery is a Li metal battery which uses Li metal as the anodes. But Li-S batteries also have major drawbacks as the intermediate S conversion compounds (commonly known as intermediate polysulfides) continuously shuttle between the two electrodes while charging and discharging limiting the reversibility of the cell. Figure 21 shows the mechanistic pathway of how S acts as a conversion cathode system.³

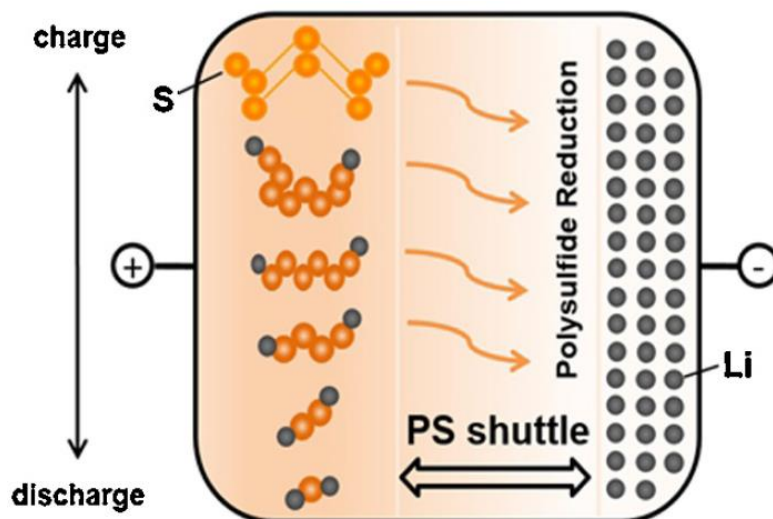


Figure 21. Working mechanism of Li-S batteries where S is working as the conversion cathode (Source: D.-W. Wang, et al. *J. Mater. Chem. A* 1, 33, 2013, 9382; adopted with permission.)

Besides, Li-S batteries, Li-O₂ batteries are also being researched where Oxygen gas is used as the cathode. But O₂ being a gaseous material these battery systems face a completely different kind of hurdles when it comes to commercialization.

Besides, there are other conversion cathodes BiF₃, CuF₂ etc. which are of research interest. Figure 22 puts light on the voltage profiles for various conversion cathodes.^{70,71}

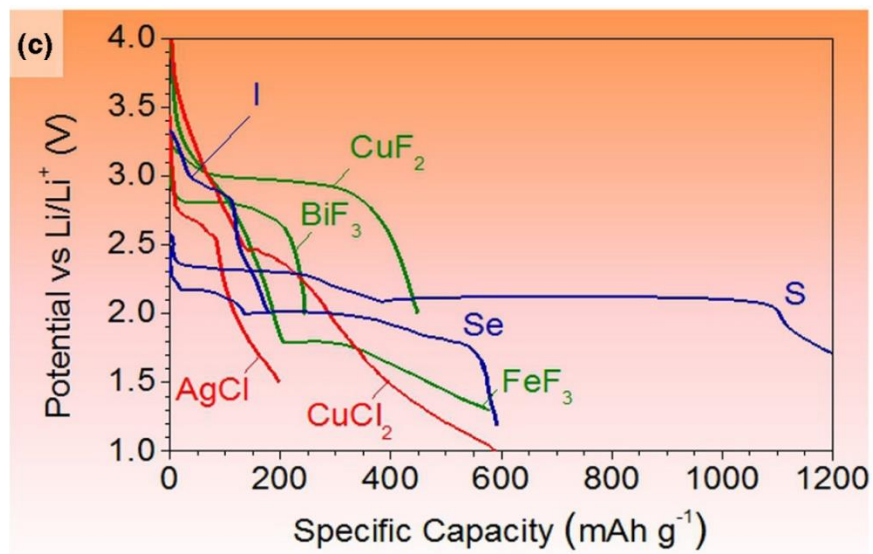


Figure 22. Voltage profile of various conversion cathodes (Materials Today, Volume 18, Number 5, June 2015; adopted with permission)

Finally, figure 23 summarizes the performance parameters of the most commonly used cathodes and anodes.

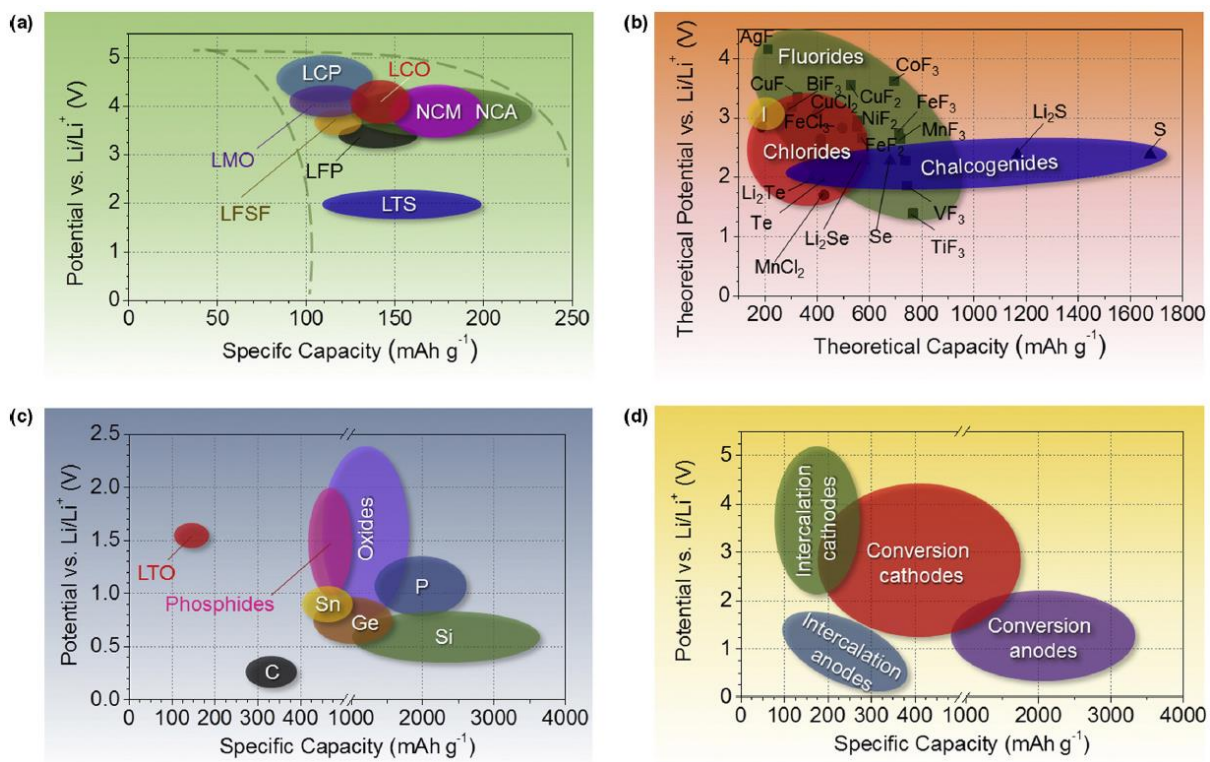


Figure 23. (a-d) Performance parameters for the common cathode and anode materials (Materials Today, Volume 18, Number 5, June 2015; adopted with permission)

Thus, as the whole this chapter provides a brief idea about the global energy demand, need for renewable energy sources and efficient energy storage devices to store the energy. It also provides basic idea about the basic energy storage systems such as batteries and capacitors followed by their working principle. Although there are exist various energy storage systems of interest, this introduction chapter provides a detailed discussion of batteries, especially Li- ion battery and its working principle and the electrode materials which are being used in this device since the working chapters of this thesis are based on electrode materials for Li-ion batteries. It is also evident that there is excellent scope for introducing novel anode and cathode materials with new chemistries to enhance the overall output of a battery marked by properties such as specific capacity, energy density and durability. This thesis focuses on anodic component of batteries.

5. References:

1. S. Najib, E. Erdem, *Nanoscale Adv.*, **2019**, 1, 2817.
2. J. B. Goodenough, K-S. Park, *J. Am. Chem. Soc.* **2013**, 135, 1167–1176.
3. N. Nitta, F. Wu, J.T. Lee, G. Yushin, *Materials Today*, **2015**, 18, 5, 252-264
4. N.A. Kaskhedikar, J. Maier, *Adv. Mater.* **2009**, 21, 25–26, 2664.
5. G-N. Zhu, Y-G. Wang, Y-Y. Xia, *Energy Environ. Sci.* **2012**, 5, 6652.
6. Z. Chen, I. Belharouak, Y.K. Sun and K. Amine, *Adv. Funct. Mater.* 2013, 23, 8, 959.
7. N. Nitta and G. Yushin, *Syst. Charact.* **2014**, 31 ,3, 317.
8. J. C. Laure, M.D. Larcher, M. R. Palacín, *Adv. Mater.* **2010**, 22, 35, 170.
9. C-M. Park, J-H. Kim, H. Kim, H-J. Sohn, *Chem. Soc. Rev.* **2010**, 39, 8, 3115.
10. Y.Y. Kenji, U.C. Hua, C. Keisuke, K.K. Furukawa, A. Yamada, *ACS Appl. Mater. Interfaces*, **2014**, 6, 14, 10892-10899
11. D. Aurbach, B. Markovsky, I. Weissman, E. Levi, Y. Ein-Eli, *Electrochim. Acta*, **1999**, 45, 1–2, 67.
12. D. Bar-Tow, E. Peled, L. Burstein, *J. Electrochem. Soc.*, 1999, 146, 824.
13. H. Nozaki, K. Nagaoka, K. Hoshi, N. Ohta, M. Inagaki, *J. Power Sources*, **2009**, 194, 1, 486.

14. M. Winter, O. Jürgen, E. B. Michael, S. P. Novák, *Adv. Mater.*, **1998**, 10, 10,725.
15. R. Mukherjee, A.V. Thomas, D. Datta, E. Singh, J. Li, O. Eksik, V.B. Shenoy, N. Koratkar, *Nat. Commun.*, **2014**, 5, 3710.
16. J. R. Dahn, T. Zheng, Y. Liu, J.S. Xue, *Science*, **1995**, 270, 5236, 590.
17. T. Zheng, W.R. McKinnon and J.R. Dahn, *J. Electrochem. Soc.*, **1995**, 142, 8, 2581.
18. K. Teshima, H. Inagaki, S. Tanaka, K. Yubuta, M. Hozumi, K. Kohama, T. Shishido, S. Oishi, *Cryst. Growth Des.*, **2011**, 11, 10, 4401.
19. S. Scharner, W. Weppner, P. S. Beurmann, *J. Electrochem. Soc.*, 1999, 146, 3, 857.
20. M. Wagemaker, D. R. Simon, E. M. Kelder, J. Schoonman, C. Ringpfeil, U. Haake, D. Lützenkirchen-Hecht, R. Frahm, F. M. Mulder, *Adv. Mater.*, **2006**, 18, 23, 3169.
21. J.-F. Colin, V. Godbole, P. Novak, *Electrochem. Commun.*, **2010**, 12, 6, 804.
22. H-G. Jung, M. W. Jang, J. Hassoun, Y-K. Sun, B. Scrosati, *Nat. Commun.*, **2011**, 2, 516.
23. F.X. Wu, Z. Wang, X. Li, H. Guo, P. Yue, X. Xiong, Z. He, Q. Zhang, *Electrochim. Acta*, **2012**, 78, 331.
24. Y-B. He, B. Li, M.Liu, C. Zhang, W. Lv, C. Yang, J. Li, H. Du, B. Zhang, Q-H. Yang, J-K. Kim, F. Kang, *Sci. Rep.*, **2012**, 2, 913.
25. Y.-B. He, M. Lu, Z.-D. Huang, B. Zhang, Y. Yu, B. Li, F. Kang, J.-K. Kim, *J. Power Sources*, **2013**, 239, 269.
26. G.-L. Xu, Q. Wang, J.-C. Fang, Y.-F. Xu, J.-T. Li, L. Huang, S.-G. Sun, *J. Mater. Chem. A*, **2014**, 2, 3, 631.
27. J. Wang, Y.-C. K. C.- Wiegart, J. Wang, *Angew. Chem. Int. Ed.* **2014**, 53, 17, 4460.
28. CK. Chan, H. Peng, G. Liu, K. McIlwrath, XF. Zhang, RA. Huggins, Y. Cui, *Nat. Nano*, **2008**, 3, 1, 31.
29. Y. Oumellal, N. Delpuech, D. Mazouzi, N. Dupré, J. Gaubicher, P. Moreau, P. Soudan, B. Lestriez, D. Guyomarda, *J. Mater. Chem.*, **2011**, 21, 17, 6201.
30. A. Magasinski, P. Dixon, B. Hertzberg, A. Kvit, J. Ayala, G. Yushin, *Nat. Mater.*, 2010, 9, 4, 353.
31. K. Roy, M. Wahid, D. Puthusseri, A. Patrike, S. Muduli, R. Vaidhyanathan, S. Ogale, *Sustainable Energy Fuels*, **2019**, 3, 245.
32. S. Tongay, J. Zhou, C. Ataca, J. Liu, J. S. Kang, T. S. Matthews, L. You, J. Li, J. C. Grossman, J. Wu, *Nano Lett.*, **2013**, 13, 6, 2831-2836

33. Y.Liu, N. S. Hudak, D. L. Huber, S. J. Limmer, J. P. Sullivan, J. Y. Huang, *Nano Lett.*, **2011**, 11, 10, 4188-4194
34. J. Qian, D. Qiao, X. Ai, Y. Cao, H. Yang, *Chem. Commun.*, 2012, 48, 71, 8931.
35. A. Darwiche, C. Marino, M. T. Sougrati, B. Fraisse, L. Stievano, L. Monconduit, *J. Am. Chem. Soc.*, **2012**, 134, 51, 20805-20811.
36. M.S. Islam, C.A. Fisher, *Chem. Soc. Rev.*, **2014**, 43, 1, 185.
37. J. Cho, YJ. Kim, B. Park, *Chem. Mater.*, **2000**, 12, 12, 3788.
38. M. Yoncheva, V. Koleva, M. Mladenov, M. Sendova-Vassileva, M. Nikolaeva-Dimitrova, R. Stoyanova, E. Zhecheva, *J. Mater. Sci.*, **2011**, 46, 22, 7082.
39. A. Sobkowiak, M. R. Roberts, R. Younesi, T. Ericsson, L. Häggström, C-W. Tai, A. M. Andersson, K. Edström, T. Gustafsson, F. Björefors, *Chem. Mater.*, **2013**, 25, 15, 3020-3029
40. J. Tu, X.B. Zhao, G.S. Cao, D.G. Zhuang, T.J. Zhu, J.P. Tu, *Electrochim. Acta*, **2006**, 51, 28, 6456.
41. F. Lin, I. M. Markus, D. Nordlund, T-C. Weng, M. D. Asta, H. L. Xin, M. M. Doeff, *Nat. Commun.*, **2014**, 5, 3529.
42. S. K. Martha, O. Haik, E. Zinigrad, I. Exnar, T. Drezen, J. H. Miners, D. Aurbach, *J. Electrochem. Soc.*, **2011**, 158, 10, A1115.
43. D. W. Murphy, F. A. Trumbore, *J. Electrochem. Soc.*, **1976**, 123, 7, 960.
44. M.S. Whittingham, *Science*, **1976**, 192, 4244, 1126.
45. M.S. Whittingham, *Chem. Rev.*, **2004**, 104, 10, 4271-4302
46. K.Mizushima, P.C.Jones, P.J.Wiseman, J.B.Goodenough, *Mater. Res. Bull.*, **1980**, 15, 6, 783.
47. A. D. Pasquier, I. Plitz, S. Menocal, G. Amatucci, *J. Power Sources*, **2003**, 115, 1, 171.
48. J.R.Dahn, E.W.Fuller, M.Obrovac, U.von Sacken, *Solid State Ionics*, **1994**, 69, 3-4, 265.
49. J.N. Reimers, J. Dahn, *J. Electrochem. Soc.*, **1992**, 139, 8, 2091.
50. E.Rossen, C.D.W.Jones, J.R.Dahn, *Solid State Ionics*, **1992**, 57, 3-4, 311.
51. J. Cho, Y. J. Kim, T-J. Kim, B. Park, *Angew. Chem.*, **2001**, 113, 18, 3471.
52. I. D. Scott, Y.S. Jung, A.S. Cavanagh, Y. Yan, A.C. Dillon, S. M. George, S-H. Lee, *Nano Lett.*, **2011**, 11, 2, 414-418

53. B. Song, W. Li, S.M. Oh, A. Manthiram, *ACS Appl. Mater. Interfaces*, **2017**, 9, 9718–9725
54. I. Bloom, S.A. Jones, V.S. Battaglia, G.L. Henriksen, J.P. Christophersen, R.B. Wright, C.D. Ho, J.R. Belt, C.G. Motloch, *J. Power Sources*, **2003**, 124, 2, 538.
55. Y. Itou, Y. Ukyo, *J. Power Sources*, **2005**, 146, 1, 39.
56. Y-K. Sun, S-T. Myung, B-C. Park, J. Prakash, I. Belharouak, K. Amine, *Nat. Mater*, **2009** 8, 4, 320.
57. K.S. Nanjundaswamy, A.K.Padhia, J.B.Goodenough, S.Okada, H.Ohtsuka, H.Arai, J.Yamaki, *Solid State Ionics*, **1996**, 92, (1–2), 1.
58. D. Doughty, E.P. Rother, *Electrochem. Soc. Interface*, **2012**, 21, 2, 2012, 35.
59. N. Recham, J-N. Chotard, L. Dupont, C. Delacourt, W. Walker, M. Armand & J-M. Tarascon, *Nat. Mater*, **2010**, 9, 1, 68.
60. F. Wang, H-C. Yu, M-H. Chen, L. Wu, N. Pereira, K. Thornton, A. V. d. Ven, Y. Zhu, G. G. Amatucci, J. Graetz, *Nat. Commun*, **2012**, 3, 1201.
61. A.J. Gmitter, J. Gural, G.G. Amatucci, *J. Power Sources*, **2012**, 217, 21.
62. F. Badway, A. N. Mansour, N. Pereira, J. F. Al-Sharab, F. Cosandey, I. Plitz, G. G. Amatucci, *Chem. Mater*, **2007**, 19, 17, 4129-4141
63. M-Q. Zhao, Q. Zhang, J-Q. Huang, G-L. Tian, J-Q. Nie, H-J. Peng, F. Wei, *Nat. Commun*, **2014**, 5, 3410.
64. D-W. Wang, Q. Zeng, G. Zhou, L. Yin, F. Li, H-M. Cheng, I. R. Gentle, G. Q. M. Lu, *J. Mater. Chem. A*, **2013**, 1, 9382-9394.
65. Y.L. Wang, Q. L. Sun, Q. Q. Zhao, J. S. Cao, S. H. Ye, *Energy Environ. Sci.*, 2011, 4, 10, 3947.
66. T. Li, Z. X. Chen, Y. L.Cao, X. P. Ai, H.X. Yang, *Electrochim. Acta*, **2012**, 68, 202.
67. J. Liu, D. Zhu, C. Guo, A. Vasileff, S-Z. Qiao, *Adv. Energy Mater*, **2013**, 3, 1, 113.
68. Z. Zhang, Z. Zhang, K. Zhang, X. Yang and Q. Li, *RSC Adv*, **2014**, 4, 15489-15492.
69. F. Wang, R. Robert, N. A. Chernova, N. Pereira, F. Omenya, F. Badway, X. Hua, M. Ruotolo, R. Zhang, L. Wu, V. Volkov, D. Su, B. Key, M. S. Whittingham, C. P. Grey, G. G. Amatucci, Y. Zhu, J. Graetz, *J. Am. Chem. Soc.*, **2011**, 133, 46, 18828-18836
70. A.J. Gmitter, J. Gural, G.G. Amatucci, *J. Power Sources*, **2012**, 217, 21.

71. F. Badway, A. N. Mansour, N. Pereira, J. F. Al-Shara, F. Cosandey, I. Plitz, G. G. Amatucci, *Chem. Mater.*, **2007**, 19, 17, 4129-4141.

Chapter 2

Fe₃SnC@CNF: A 3D Antiperovskite Intermetallic Carbide System as a New Robust High-Capacity Lithium-Ion Battery Anode

A 3D intermetallic anti-perovskite carbide, Fe₃SnC, is reported as a Li-ion battery anode. Single-phase Fe₃SnC showed a reversible Li-ion capacity of 426 mAhg⁻¹ that increased significantly (600 mAhg⁻¹) upon its in situ synthesis by electrospinning and pyrolysis to render a conducting carbon nanofibre (CNF) based composite. Importantly, the Fe₃SnC@CNF composite showed excellent stability in up to 1000 cycles with a remarkable 96% retention of capacity. The rate performance was equally impressive with a high capacity of 500 mAhg⁻¹ delivered at a high current density of 2 Ag⁻¹. An estimation of Li ion diffusion from the electrochemical impedance data showed a major enhancement of the rate by a factor of 2 in the case of Fe₃SnC@CNF compared to the single-phase Fe₃SnC sample. Post-cyclic characterization revealed that the unit cell was retained despite a volume expansion upon the inclusion of four Li atoms per unit cell, as calculated from the capacity value. The cyclic voltammogram shows four distinctive peaks that could be identified as the sequential incorporation of up to four Li atoms. First-principles DFT calculations were performed to elucidate the favourable sites for the inclusion of 1–4 Li atoms inside the Fe₃SnC unit cell along with the associated strain.

Related publication: *ChemSusChem*, 2020, 13, 196 – 204

Declaration

The text and the figures in this chapter are being reproduced from my own co-authored publication “*ChemSusChem, 2020,13, 196-204*” with permission from the publisher

I acknowledge help and active collaboration of Dr. Vinila Chavan in the synthesis of single phase Fe₃SnC material and Mr. Mujaffer Hossain and Dr. Prasenjit Ghosh in DFT calculations

1. Introduction:

The most recent research on anode materials for Li-ion batteries has focused on the development of new materials with distinct advantages over existing ones. New materials must deliver better than existing ones on certain important parameters such as cyclic stability, voltage hysteresis, operating potential, current stability and capacity.^[1-4] The key anode materials researched thus far fall into three broad categories of conversion, alloying and intercalation types and are limited in one way or another to stake the claim of perfection in terms of desirable performance parameters.^[5-9] Silicon is the most notable of the anode materials that is researched with great interest. Although it promises the highest achievable capacity, it falls short in terms of cycling and current stability because of very high volume expansion and related pulverisation.^[10-12] Various strategies that involve composite formation have been examined to improve Si-based anode performance, but the issues still appear to be only partially resolved.^[13-17] Other interesting alloy alternatives such as Sn and Sb also suffer from similar limitations.^[18, 19] The key conversion materials researched thus far, that is, transition and post-transition metal oxides, sulfides and phosphides, have separate problems of high operating potentials and high voltage hysteresis.^[7] However, intercalation-type materials are the best thus far in terms of cycling and rate stabilities. In general, the low capacities of these materials along with high operating potentials (especially associated with some promising candidates) have been recognised as their major limitations.^[3, 20] Apart from graphite, none of the other anode materials in the present pool has passed the stringent tests of present-day commercial specifications. However, the rapid growth of the projected applications of Li-ion batteries in the near future calls for a further intense search for new alternatives to graphite because of its theoretically limited low capacity. Recently, phosphide- and nitride-based compounds of transition metals (TMs) and post-TMs have been visited for Li-ion battery applications, but because of underlying conversion and alloying mechanisms, these materials are also not free of limitations.^[21-24] Carbide-based materials are under active consideration in different applications because of the special metallic structure with C atoms located in the voids of the densely packed metallic lattice.^[25-30] Carbides have delivered superbly in catalysis and some of their exciting properties such as high electronic conductivity, mechanical robustness and corrosion resistance could be hugely beneficial for a role as anode materials in Li-ion batteries. Indeed, some TM-based binary carbides such as

Mo_2C , Ti_3C_2 , Nb_2C and V_2C have been evaluated for anode applications.^[27,31,32] Minchan Li et al. have shown that ultrafine MoC nanoparticles in carbon matrix deliver reversible and stable capacity of 742 mA hg^{-1} for up to 100 initial cycles at 200 mA hg^{-1} .^[33] The special family of two-dimensional carbides, Mxenes has also been studied for anode applications in Li ion batteries by Gogotsi and coworkers.^[27,28,32] The special layered structure of such 2D carbides has been the primary attraction here owing to apparent intercalation type Li storage with higher capacity than the familiar intercalation types anodes.^[27,28,32] Qing Tang et al. have shown by computational studies that Ti_3C_2 based Mxenes possess low Li diffusion barriers and high theoretical capacity apart from possessing high conductivity.^[34] Si-based 2D carbides of formulae SiC_8 with stabilized planar tetracoordinate $\text{C}_{12}\text{H}_8\text{Si}$ units can accommodate six Li atoms per unit cell and as such can deliver a theoretical capacity of 1297 mA hg^{-1} .^[35] However, on practical front although these 2D carbides exhibited commendable stabilities, they have been found wanting in terms of capacity, long term cyclic stability, and rate performance. We noted that 3D carbides, specially the antiperovskite compounds having a universal formula AXM_3 (A=Ga, Al, In, Zn, Sn, etc.; X=C, N, B; M=Ti, Mn, Fe, Co, or Ni) which are endowed with robust mechanical structure, better 3D packing, intermetallic nature, and simultaneous presence of transition metal (TM) and Non-TM, have remained mostly unexplored in terms of their electrochemical properties as anode materials for Li-ion batteries.^[36-39] There is only one report by Chen et. al. wherein a ternary carbide Co_3ZnC , involving both transition metals in a carbon nanotube matrix was studied, and it exhibited a high reversible capacity of 800 mAhg^{-1} along with a retained capacity of 585 mAhg^{-1} after 1500 cycles.^[40] In this work we examine a new ternary carbide system (Fe_3SnC) containing a post transition Sn metal, which is already and separately of interest in the Li-ion battery context, in addition to an earth abundant late transition metal (Fe) and non-TM Carbon, forming an antiperovskite 3D carbide. The choice of material was made on the basis of special antiperovskite structure, its mechanical robustness, and the presence of redox active centres in terms Fe and Sn. Our conjecture was that the favourable structure, mechanical strength (high ductility) and the presence of multiple redox centres can allow an easy accommodation of Li in the octahedral/ tetrahedral sites in the 3D lattice of carbides in spite of volume expansion. The Pugh criterion of proposed ductility and brittleness of a material provided a strong back up to the high ductility of our material where the bulk modulus(B)/Shear modulus(G) ratio was found out to be ~ 2.5 ($\text{B/G} > 1.75$ suggests a material to be ductile).^[41] Furthermore, we were able to increase the

capacity of single phase Fe_3SnC (440 mAhg^{-1}) by an in-situ synthesis via electrospinning and pyrolysis, rendering a conducting carbon nano-fibre (CNF) based composite. We achieved a highly stable capacity of 600 mAh g^{-1} with negligible loss in the capacity even after 1000 charging/discharging cycles. The rate stability is another hall mark as the capacity of 500 mAh g^{-1} was observed even at high current density of 2 A g^{-1} . It is to be noted that, to the best of our knowledge, this is very first report of synthesis of a carbide system in a conducting carbon fibre matrix exploiting the use of electrospinning technique. Estimates based on the observed capacity reveal that inclusion of four Li atoms occurs inside the cubic unit cell of Fe_3SnC , which is justified by the first principle Density Functional Theory (DFT) calculations. Post cycling characterizations showed that the cubic structure of Fe_3SnC remains in-tact upon lithiation and de-lithiation owing to the robustness (elasticity) of the carbide system against lithiation strain.

2. Experimental Section:

2.1. Synthesis of single phase Fe_3SnC composite:

The single phase polycrystalline Fe_3SnC was synthesized by a solid-state reaction performed in an evacuated quartz tube. Metal powders of Iron (Fe), Tin (Sn) and Graphite (C) were mixed and ground for about 30 minutes. The mixture was placed in quartz tube, sealed under vacuum and heated at 900°C for 72 hrs, followed by a quench to room temperature. The mixture was pulverised, ground and annealed in evacuated quartz tube again using the same heating protocol. After the second heating, the tube was cooled to room temperature. It should be noted that an excess of Graphite was added in the initial composition to avoid carbon loss. After that the material was ball milled for 5 hours using a Retsch MM400 ball miller. The milling and stand-by time was 30 minutes each. The ball milled sample was labelled as $\text{Fe}_3\text{SnC-BM}$.

2.2. Synthesis of $\text{Fe}_3\text{SnC@CNF}$ composite:

The synthesis was carried out by using the technique of electrospinning. First, a mixture of FeCl_3 and SnCl_2 was dissolved (3:1 molar ratio) in a 10 wt.% Dimethylformamide (DMF) solution of Polyacrylonitrile (PAN). The resulting solution was taken in a syringe and put for electrospinning at a flow rate of 0.5 ml/hour . After collection of the fibre mat (Fig 1a), the same was calcined for 2 hours at 200°C followed by an Argon (Ar) pyrolysis at 800°C for 4 hours. The obtained fibre matter was named as $\text{Fe}_3\text{SnC@CNF}$ composite (Fig 1b).

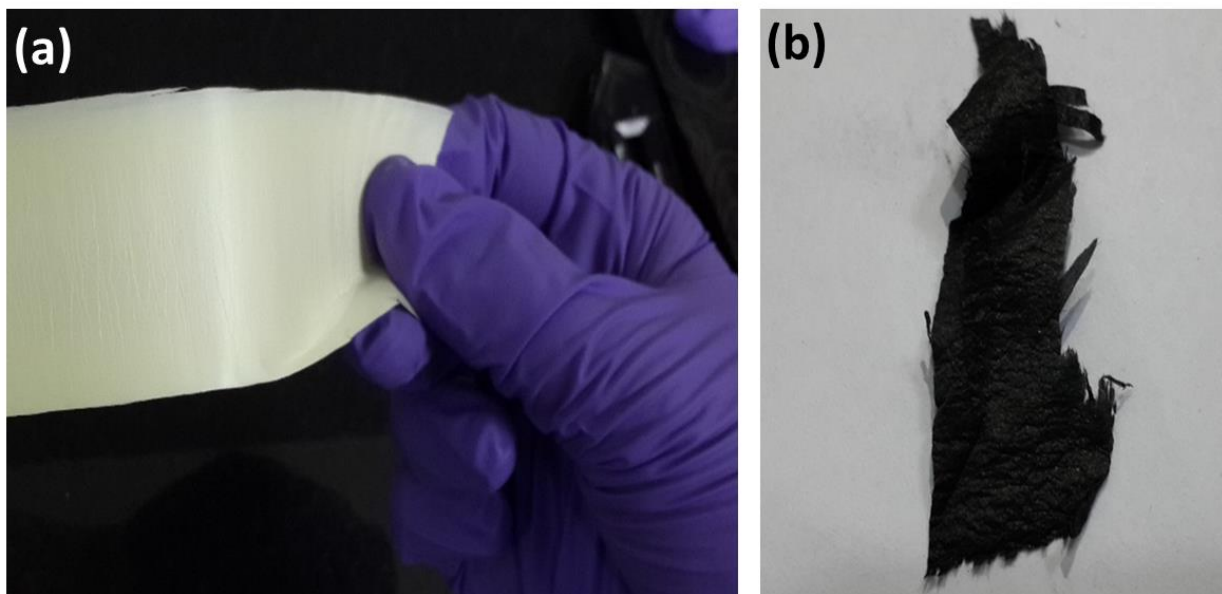


Fig. 1. (a) Electro-spun fibre mat derived from a solution of FeCl_3 and SnCl_2 in 10 wt.% DMF solution of Polyacrylonitrile (PAN), (b) fibre mat after pyrolysis.

2.3. Electrode and coin cell fabrication:

The electrodes for both the single phase Fe_3SnC and $\text{Fe}_3\text{SnC@CNF}$ composite materials were made by mixing the active material, conducting carbon (Super-P) and PVDF (Polyvinylidene difluoride, Sigma Aldrich) binder (Weight ratios were maintained as 8:1:1) in N-Methyl-2-pyrrolidone solvent and coating the slurry onto a Cu foil. Then the electrodes were dried in the oven at 80°C overnight. The dried electrodes were then cut into round-shaped electrodes using a disc-cutter. 2032 type coin cells were made in Ar-filled glove box. For all the studies Lithium hexafluorophosphate (LiPF_6) electrolyte was used in a solvent combination of 1:1 Ethylene carbonate (EC) and Dimethyl carbonate (DMC) along with 5 wt.% fluoroethylene carbonate (FEC, Sigma Aldrich) as additive. Celgard 2500 was used as the separator.

2.4. Measurements:

Powder X-ray diffraction and Field emission SEM (FE-SEM) along with Energy dispersive x-ray (EDAX) were done using Bruker D8 advance x-ray instrument and NOVA nano SEM, respectively. The high resolution transmission electron microscopy (HRTEM) and selected area electron diffraction (SAED) were performed using (Jeol, JEM 2200FS, 200KeV). Cyclic

voltammetry was performed in Ametek potentiostat at a scan-rate of 0.2 mV/s keeping the vertex potentials from 0.01 to 3 V. The galvanostatic charge-discharge measurements were carried out in MTI corporation battery analyser at different current densities of 0.05 Ag⁻¹, 0.1 Ag⁻¹, 0.5 Ag⁻¹, 1 Ag⁻¹ to 2 Ag⁻¹. The potentiostatic electrochemical impedance spectroscopy was also performed in the Ametek potentiostat instrument in a frequency ranging from 300 KHz to 100 mHz.

3. Results and Discussions:

3.1. Structural characterizations of single phase Fe₃SnC:

It is well known that nanoparticles with smaller crystallite size and high surface area, have a greater surface energy to participate in any given reaction. Hence, we decided to ball-mill the as-synthesized chunks of Fe₃SnC, in order to fully exploit its capacity as a Lithium ion battery anode. The PXRD of the ball milled sample reveals a phase pure Fe₃SnC pattern, as observed in Fig. 2a, wherein all the peaks match to those of as-synthesized Fe₃SnC (from the Inorganic crystal structure database data). However, the peak corresponding to C (111) at 2 theta=26.7° was noted to be absent in the ball milled sample (Fig. 2a) compared to the non-ball-milled one. This may be attributed to the conversion of the excess carbon as gaseous product during the local heat generated during ball milling. The crystallite size of the ball milled Fe₃SnC was found to be about 25 nm. EDAX data shown in Fig. 2b confirms that the stoichiometric composition of the constituent elements is retained in the ball milled Fe₃SnC. The HRTEM image (Fig. 2c) reveals a typical platelet type crystal growth (marked in Fig. 2c) morphology possibly due to the presence of graphitic carbon or screw dislocation driven crystal growth. The calculated d-spacing from HRTEM (~0.2 nm) matches well with the XRD data (d-spacing of the (111) plane of the Fe₃SnC crystal) (Fig. 2d).

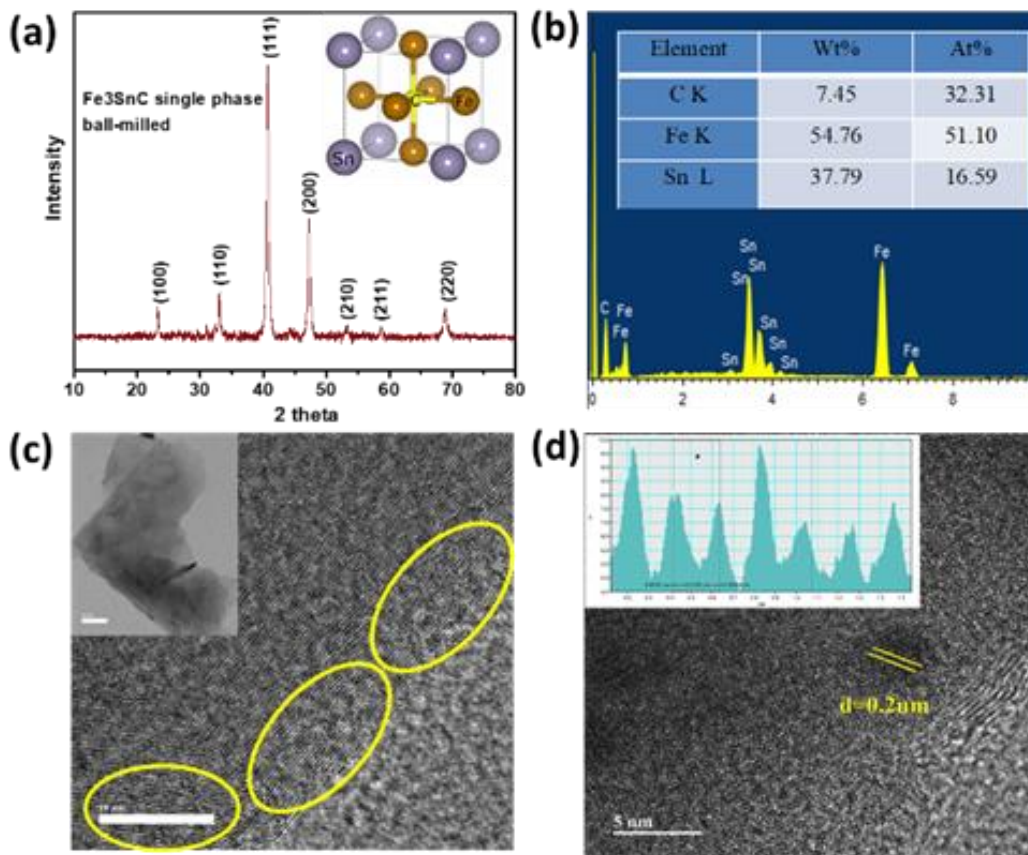


Fig 2. Characterizations of the ball-milled single-phase Fe₃SnC sample: **(a)** Powder X-ray diffraction analysis (Inset is the antiperovskite structure of Fe₃SnC), **(b)** EDAX analysis, **(c and d)** HRTEM analysis (Inset of fig. 1d shows the interplanar distance of the Fe₃SnC (111) plane).

3.2. Electrochemical characterizations of single phase Fe₃SnC:

The ball-milled particles show an initial discharge capacity of 584 mAh g⁻¹ (Fig. 3a), which is noted to be much higher compared to the non-ball-milled sample. This can be attributed to the finer and smaller particle size of the ball-milled surface, thereby providing much larger surface area, which enables greater fraction of Li incorporation inside the bulk of the material (Fig 3c). However, this shows an increasing trend in reversible capacity (Fig. 3c), which tends to stabilize from about 90th cycle onwards and after 150 cycles it shows a reversible capacity of 426 mAhg⁻¹ with a Coloumbic efficiency of ~100% (Fig. 3c). This can be attributed to the fact that for the Fe₃SnC crystal system, activation of the favourable octahedral and tetrahedral sites (as evident from the theoretical studies discussed later) for Li accommodation required a potential driven electrochemical activation. This increasing trend of capacity for Sn containing systems has been reported in some literatures previously.^[42,43] A similar trend can also be observed in the rate

performance studies (Fig. 3c inset), wherein after measuring the charging and discharging capacities at variable current densities of 50 mA g^{-1} , 100 mA g^{-1} , 200 mA g^{-1} , 500 mA g^{-1} , 1 Ag^{-1} and 2 Ag^{-1} , reverting back to 50 mA g^{-1} showed an increasing trend in capacity. The Nyquist plot (Fig. 4a) reveals that the electrochemical series resistance (R_s) is $\sim 6.5 \Omega$ and the charge transfer resistance (R_{ct}) is 138Ω .

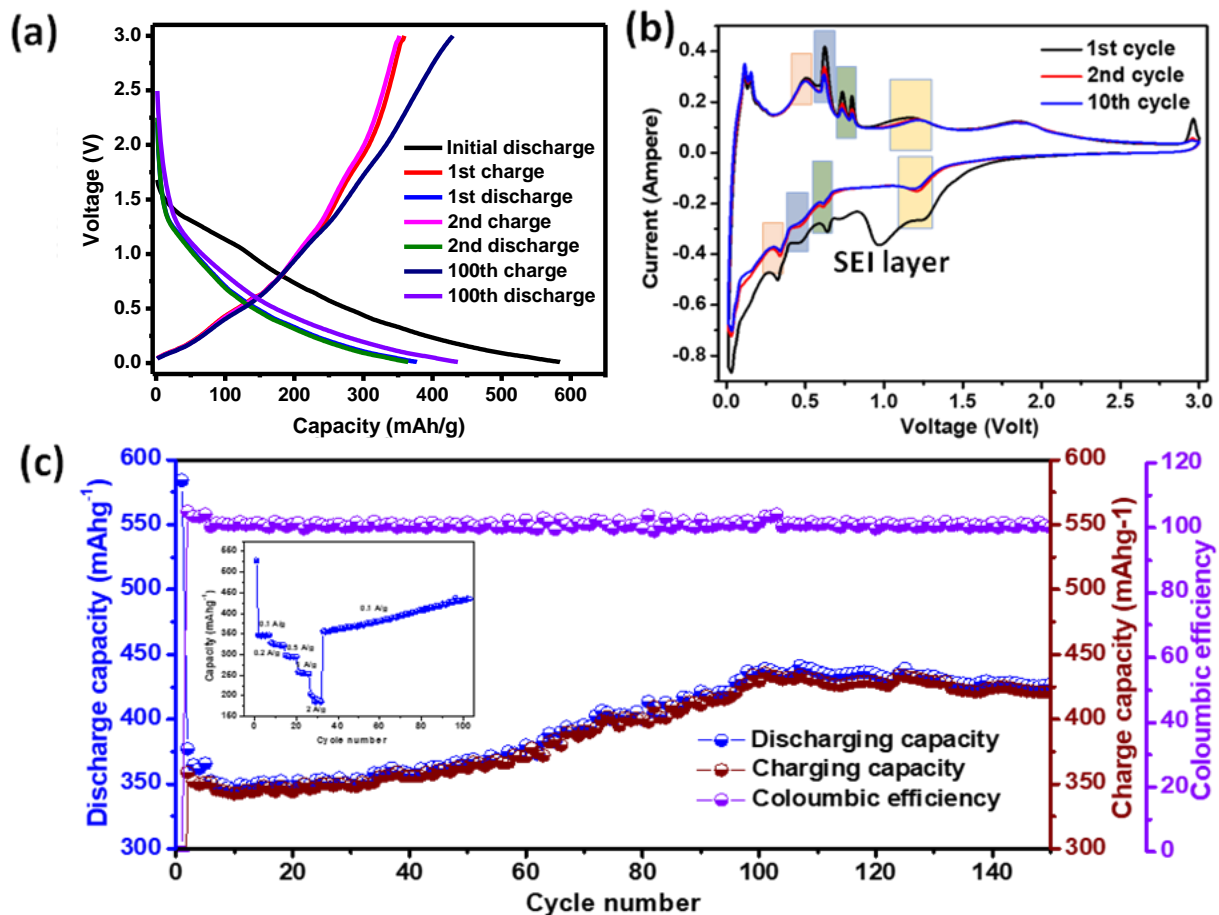


Fig 3. Electrochemical studies on ball-milled single-phase Fe_3SnC : (a) charge-discharge pattern, (b) cyclic voltammetry data, (c) stability and Coulombic efficiency (Inset shows the rate performance).

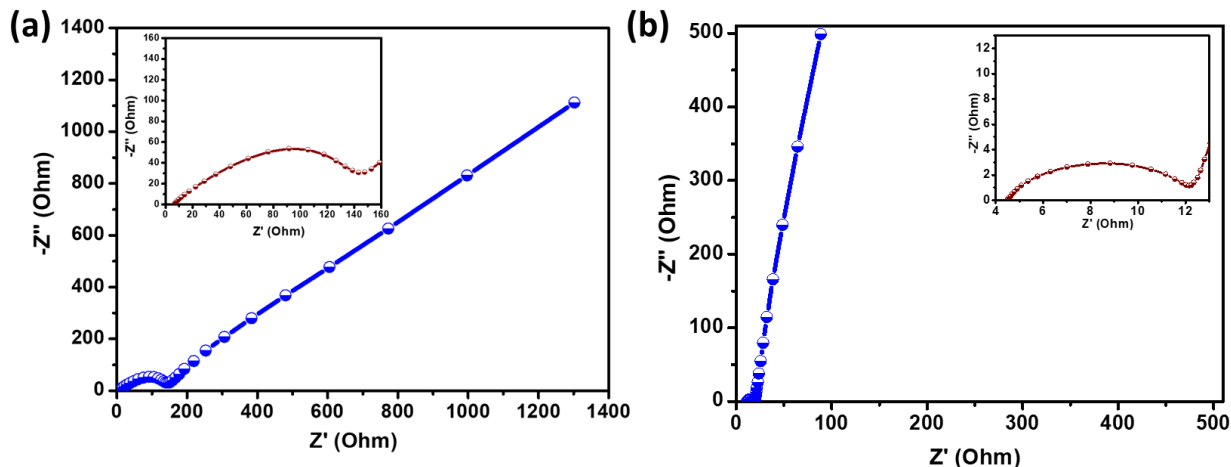


Fig 4. Impedance spectra recorded of the fresh cell of the (a) single phase ball-milled Fe_3SnC sample, and (b) $\text{Fe}_3\text{SnC}@ \text{CNF}$ sample.

We performed a simple calculation based on the realized capacity of $\sim 420 \text{ mAhg}^{-1}$ (by comparing the potential window from both the CV and the charge-discharge data of Fig. 5a and 5b) to determine the number of Li atom which may have been accommodated by one Fe_3SnC unit, and this number turned out to be ~ 4 . The detailed calculation procedure is as follows.^[44]

Capacity contribution calculation:

$1 \text{ mAh} = 3.6\text{C} = 2.2 \times 10^{19}$ number of electron or Li^+ .

In this case, for the Fe_3SnC system, the observed stable capacity was $\sim 400 \text{ mAhg}^{-1}$

This would yield the number of Li^+ ion $= 2.2 \times 10^{19} \times 420 = 924 \times 10^{19}$.

Hence, the specific capacity of 420 mAhg^{-1} is realized from 924×10^{19} no of Li^+ (we assume that Li^+ ions are the sole charge carriers).

The molecular weight of Fe_3SnC is 298.26 g/mol .

Hence, weight for unit cell of Fe_3SnC would be $298.26 / (6.023 \times 10^{23}) \text{ g}$

Considering that for 1 g of the Fe_3SnC , the calculated number of Li^+ ions to be $924 \times 10^{19} \Rightarrow$ number of Li^+ per unit cell of Fe_3SnC turned out to be $= 924 \times 10^{19} \times 298.26 / (6.023 \times 10^{23}) = \sim 4$.

Rest of the capacities ($\sim 25 \text{ mAhg}^{-1}$ were from the capacitive contribution from the carbonaceous additive)

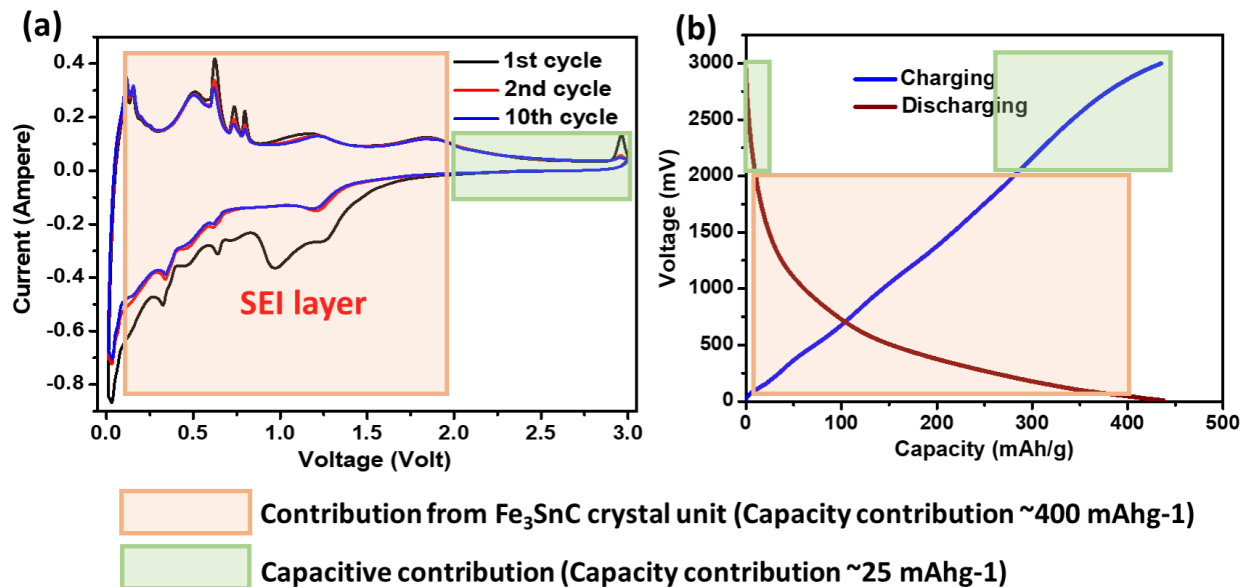


Fig 5. Capacity contribution calculation on single phase Fe₃SnC ball-milled sample.

Interestingly, this could be nicely correlated with the CV data (Fig. 3b) where four clear peaks are observed in a potential window of 0.15 to 2 volt on both the anodic and cathodic potential windows, signifying reversible uptake and release of four Li atoms by the Fe₃SnC crystal system. This can again be correlated with the plateau regions in the charge discharge data in Fig. 3a. A peak at ~1V corresponds to the formation of the solid-electrolyte interphase (SEI) layer which is absent from the consecutive cycles delivering a stable performance. The anodic peaks at ~0.2V, ~0.4V and ~0.6V correspond to the alloying reactions of Li with Sn to form Li_xSn, and their cathodic counterparts at ~0.5, ~0.6V, ~0.75V suggest the corresponding de-alloying reactions (Fig. 3b).^[45-47] Li extraction from carbon is reflected in the broad oxidation peak at ~1.2V.^[42,45,46] Another broad peak at ~1.8V suggests the catalytic decomposition of the electrolyte on Sn.^[43] The CV peaks are also prominent in the subsequent cycles which is a testimony to the robustness of the 3D carbide system in terms of holding its structure under reversible electrochemical perturbation.

To have a comparison between the ball-milled and non ball-milled sample Fe_3SnC samples, we have also performed the Raman spectroscopy and the charge-discharge stability of the non ball-milled sample. The data reveal the superiority of the ball-milled sample over the non ball-milled one. This is because the fact that ball-milled samples are much smaller in size and hence can provide better accessibility and diffusion pathway to the Li-ions.

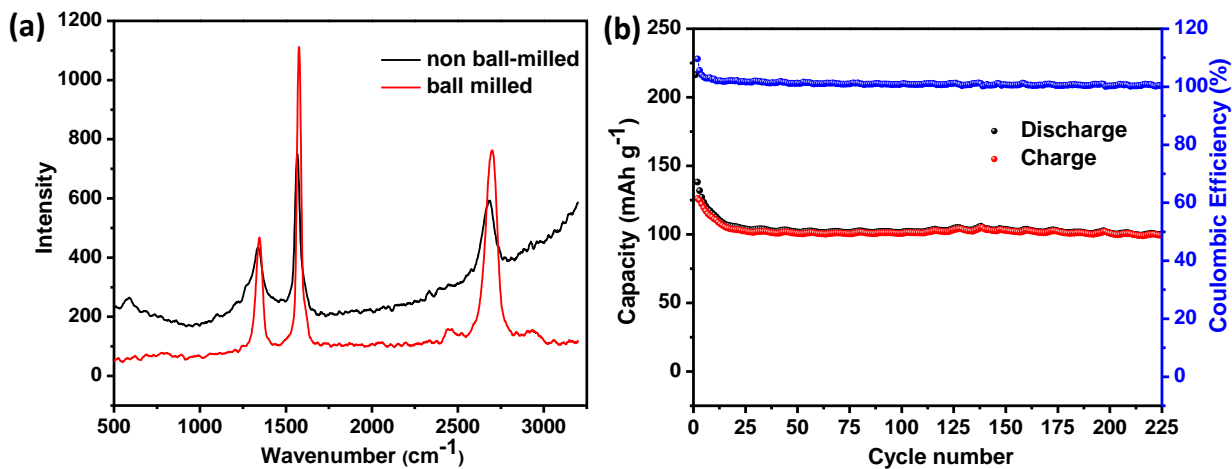


Fig. 6. (a) Raman spectroscopy data comparison for the ball-milled and non ball-milled samples (b) Stability data of the non ball-milled sample.

3.3. Post cycling characterizations on single phase Fe₃SnC system:

To prove the robustness of this 3D intermetallic carbide, we also performed ex-situ post-cycling x-ray diffraction studies and it was found that the Fe₃SnC crystal retained its cubic structure both after lithiation and delithiation (fig.7) owing to the high ductility of the system (B/G ~2.5). However, a tensile strain in the crystal structure was observed after discharge due to incorporation of Li ions in the cubic system as the XRD peaks showed systematic shifts towards lower 2 theta (Fig. 7a and 7b). Upon de-lithiation the system showed a tendency to return to its original configuration with some degree of irreversibility (Fig. 7a and 7b). This fact can also be nicely correlated with the selected area electron diffraction (SAED) pattern (Fig. 8a and 8b) wherein the interplanar distance in the reciprocal space is decreasing, indicating a higher interlayer spacing (d value) of the lithiated Fe₃SnC compared to the non-lithiated (as-made) one.

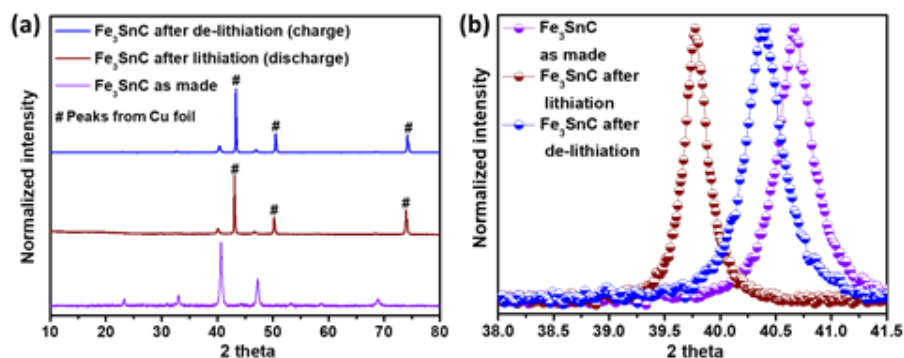


Fig 7. Post cycling x-ray diffraction studies on the Fe₃SnC single phase ball-milled sample. Zoomed part to show the shift towards lower 2 theta after 100 discharge (a) whole area (b) zoomed area of the highest intensity (111) peak.

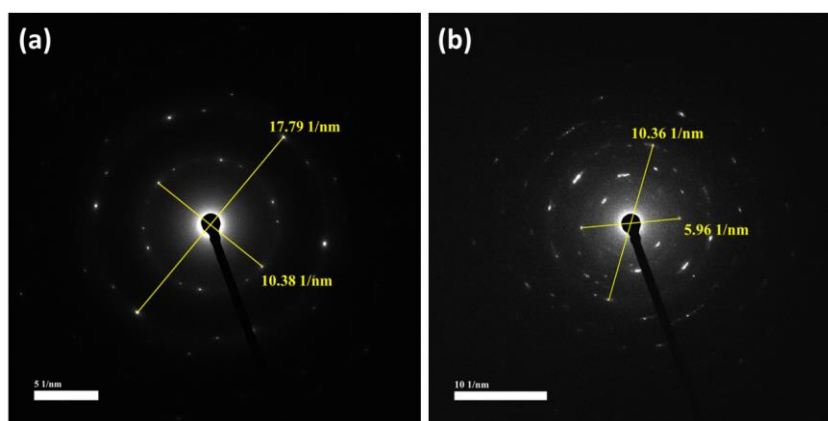


Fig 8. SAED pattern of single-phase ball-milled Fe₃SnC sample: (a) as-made sample, (b) Sample after 100 discharge.

3.4.Theoretical studies:

In order to probe further into the cause of such high specific capacity and robust nature of cycling stability of Fe_3SnC , we addressed the question of the evolution of the ternary carbide intermetallic structure as a function of the addition of 1-4 Li atoms into the same, as evidenced by the CV plots. While it is clear from the pre- and post-lithiation XRD and the SAED data that the structure generates disorder or at least crumbles into a nanostructured constitution (large XRD linewidth and diffused spots in the SAED pattern) (fig.7a and 7b and fig. 8a and 8b) with subsequent lithiation/delithiation retaining broadly the same constitution (albeit possibly with some nanoscale evolutions), it is useful to understand the cause of such scenario. It is important to note that even in the case of a disordered state of a solid the local order persists and the corresponding energetics could be important to understand. Towards this end we performed first principle Density Functional Theory (DFT) computations to explore the lattice energetics, structures, and strain as a function of the inclusion of 1-4 Li atoms to the structure. Table 1, 2 and 3 show the lowest energy structures and the volume expansion (with respect to bulk Fe_3SnC) induced in the system as a result of insertion of 1-4 Li atoms. We find that Lithiation not only results in novel structures of $\text{Li}_x\text{Fe}_3\text{SnC}$ ($x=1-4$) that are different from the original cubic anti-perovskite structure of Fe_3SnC but also results in a volume expansion. The volume expansion and thereby the strain induced in the system due to Lithiation increases with the increase in the number of the inserted Li ions. The enhancement of % volume expansion shows a jump when the second Li-ion is internalized, but the rise in the same is not equally significant when additional Li ions are inserted. It may be noted that the bond angle evolutions are also not monotonic, which means that the perturbation to the lattice system is quite significant and with the presence of major strain in the system, disordering can be expected, as indeed is experimentally seen. It should be recognized that during the room temperature electrochemical lithiation and delithiation the lattice structure does not get an opportunity to thermodynamically equilibrate and acquire the energetically lowest interesting structural forms that are reflected in the DFT calculations. Making solids with different Li content such as $\text{Li}_x\text{Fe}_3\text{SnC}$ ($x=1-4$) using a high temperature process could enable the full connection between the DFT calculations and the structural evolution of the ternary intermetallic carbide.

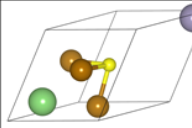
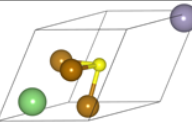
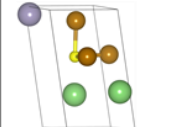
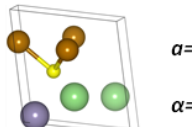
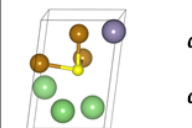
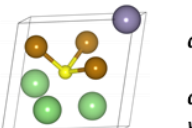
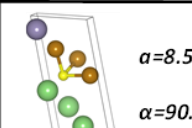
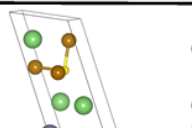
No. of Li atoms	GGA			GGA+U	
	Lithiated unit cell	% strain		Lithiated unit cell	% strain
1	 $a=b=c=4.39 \text{ \AA}$ $\alpha=\beta=\gamma=67.03^\circ$	24	Brown (Fe)	 $a=b=c=4.61 \text{ \AA}$ $\alpha=\beta=\gamma=73^\circ$	18
2	 $a=6.48 \text{ \AA} \quad b=c=3.79 \text{ \AA}$ $\alpha=89.26^\circ \quad \beta=\gamma=97.02^\circ$	66	Grey (Sn)	 $a=5.38 \text{ \AA} \quad b=c=5.19 \text{ \AA}$ $\alpha=60.17^\circ \quad \beta=\gamma=111.52^\circ$	55
3	 $a=b=3.99 \text{ \AA} \quad c=6.42 \text{ \AA}$ $\alpha=\beta=95.69^\circ \quad \gamma=79.03^\circ$	80	Yellow (C)	 $a=b=5.07 \text{ \AA} \quad c=5.20 \text{ \AA}$ $\alpha=80.57^\circ \quad \beta=80.33^\circ$ $\gamma=99.67^\circ$	73
4	 $a=8.51 \text{ \AA} \quad b=3.76 \text{ \AA} \quad c=4.63 \text{ \AA}$ $\alpha=90.04^\circ \quad \beta=66.03^\circ \quad \gamma=66.08^\circ$	119	Green (Li)	 $a=b=4.06 \text{ \AA} \quad c=9.34 \text{ \AA}$ $\alpha=89.96^\circ \quad \beta=90.73^\circ$ $\gamma=64.29^\circ$	88

Table.1. Results of the First Principles Density Functional Theory Calculations based on GGA and GGA+U models for 1, 2, 3, 4 Li incorporated Fe_3SnC with values of strains (%) and lattice parameters.

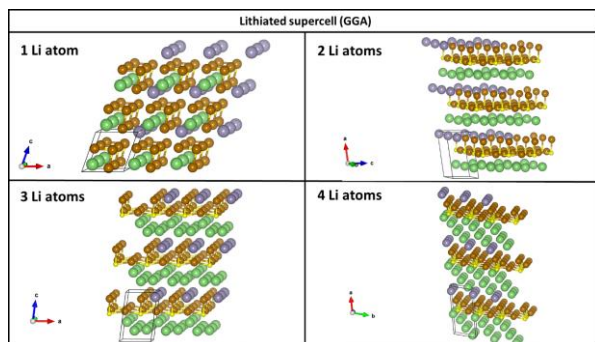


Table 2. Repeating unit of lithiated Fe_3SnC (successive addition of 1 to 4 Li atoms) using GGA approximation.

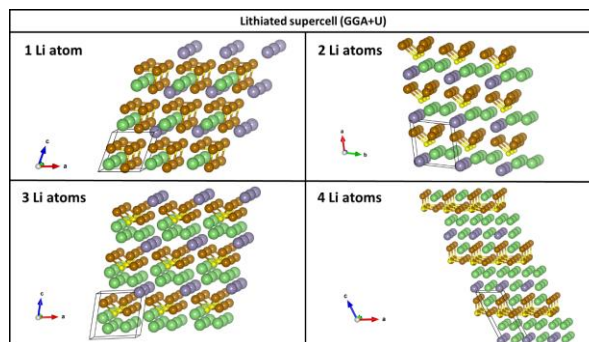


Table 3. Repeating unit of lithiated Fe_3SnC (successive addition of 1 to 4 Li atoms) using GGA+U approximation.

3.4.1. Computational details:

The calculations were performed using spin polarized density functional theory (DFT) calculations with the help of Quantum ESPRESSO software package, which is a plane-wave pseudopotential based implementation of DFT.^[48] Ultrasoft pseudopotentials were used to describe the electron ion interactions.^[49] The electron-electron exchange correlation was described by the Perdew-Burke-Ernzerhof (PBE) parametrization of the generalized gradient approximation (GGA).^[50] Since conventional exchange correlation functionals cannot correctly capture the strong electron-electron correlation effects observed in transition metal based compounds, we have used the DFT+ U_{eff} approach using the Cococcioni-Gironcoli method as implemented in QE.^[51-54] The pseudopotentials used for Fe, Sn and C have a valence electron configuration of $3D^6 4S^2$ (Fe), $5S^2 5P^2$ (Sn), $2S^2 2P^2$ (C). The wavefunction and the charge density are expanded in a plane wave basis with cut offs of 60 Ry and 500 Ry respectively. The Brillouin zone integrations were performed with a shifted $(12 \times 12 \times 12)$ Monkhorst-Pack k-point mesh for bulk.^[55] Further to speed up convergence, we have used Marzari-Vanderbilt based smearing scheme with a smearing width of 0.008 Ry width to speed up the convergence.^[56]

3.4.2. Determination of U:

In order to determine the U, we have used the linear response method proposed by Cococcioni-Gironcoli.^[51-54] The advantage of this method lies in the fact that it allows us to compute U_{eff} internally in a self-consistent way without making prior assumptions about the screening and/or basis set used in the calculation. According to the linear response theory, the response (χ_{IJ}) of d state occupations to a small localized perturbation potential α is given by:

$$\chi_{IJ} = \frac{\partial^2 E}{\partial \alpha_I \alpha_J} = \frac{\partial n_I}{\partial \alpha_J}$$

U_{eff} is then given by:

$$U_{eff} = (\chi_0^{-1} - \chi^{-1})$$

where the first and the second terms on the right-hand side of the above equation are the Kohn-Sham and the interacting inverse density response function of the system with respect to localized perturbations. By changing α , we obtain the bare and the self-consistent occupation

regression response functions, which are plotted in Fig S12. Then χ_0^{-1} and χ^{-1} are given by the slopes of the plot. From there we determine U_{eff} to be 5.0 eV

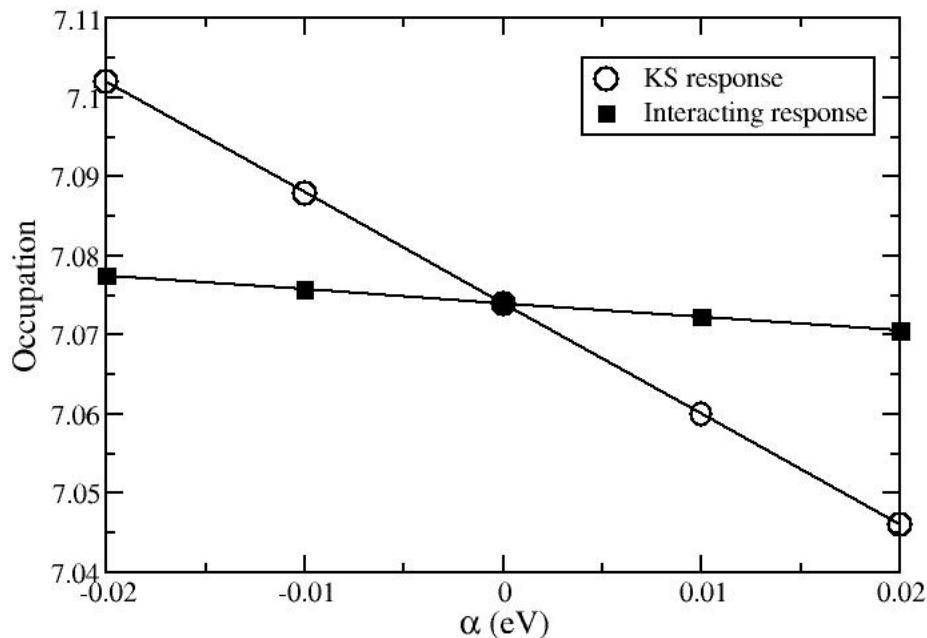


Fig 9. Linear response of Fe- d occupation to the change of potential shift α .

Fe_3SnC has an antiperovskite cubic structure (as shown in Fig 9a) with $Pm\bar{3}m$ space group (No. 221). At low temperatures it is known to exhibit spin glass behaviour. Hence it is expected that DFT ground state ($T=0\text{K}$) should be magnetic. However, from our GGA calculations we find the non-magnetic configuration to be lowest in energy. Upon including the U_{eff} in our calculations we find that as expected the ground state is ferromagnetic. However, as shown below the GGA+ U_{eff} calculations overestimate the lattice parameters. Hence for all the cases we have performed the calculations with both GGA and GGA+ U_{eff} . The bulk lattice parameter for the ferromagnetic configuration of Fe_3SnC obtained from our calculations using GGA and GGA+ U_{eff} was found to be 3.88 Å and 4.19 Å, respectively. These values were overestimated by 0.61% and 8.5%, respectively compared to experimentally reported value of 3.86-3.89Å.^[57-59]

It was observed experimentally that single phase Fe_3SnC can accommodate 4 Li atoms per unit cell. On inspection of the antiperovskite structure one can observe that Li atoms can be plausibly accommodated either in three octahedral voids in three different directions Fig 10c or either of the eight tetrahedral voids Fig 10b or a combination of both the octahedral and tetrahedral voids present in the Fe_3SnC structure. Hence as the number of Li atoms inserted increases the number of possible configurations also increase. In our study, for each case we have considered all the possible symmetry inequivalent configurations and optimized their structure (both atomic positions and lattice parameters) to find the lowest energy configuration for a given Li concentration. These minimum energy configurations are shown in table 1 and table 2 (with GGA) and table 1 and table 3 with GGA+ U_{eff} . Further, for each case the % volume expansion was computed using the following expression:

$$\text{Volume expansion (\%)} = \frac{V_{\text{Li}x\text{Fe}_3\text{SnC}} - V_{\text{Fe}_3\text{SnC}}}{V_{\text{Fe}_3\text{SnC}}} \times 100 ;$$

where $x = 1, 2, 3, 4$ number Li ions.

$V_{\text{Li}x\text{Fe}_3\text{SnC}}$ = Volume of lithiated Fe_3SnC structure during discharging of cell

$V_{\text{Fe}_3\text{SnC}}$ = Volume of Fe_3SnC structure during charging of the cell

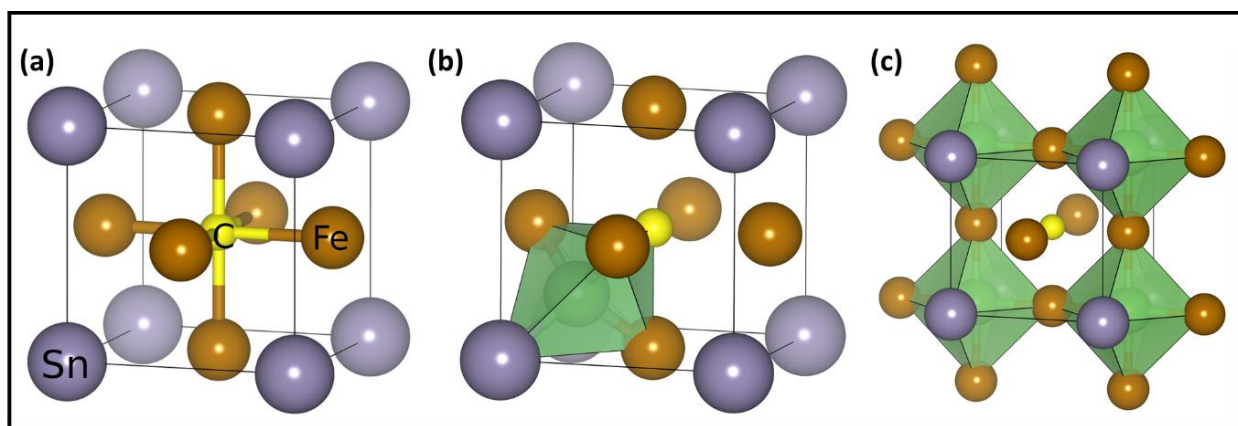


Fig 10. (a) Crystal structure of Fe_3SnC : (b) Tetrahedral sites for Li, (c) Octahedral sites for Li.

3.5. Synthesis, characterizations of Fe₃SnC@CNF composite:

Following the results of the initial work on the Fe₃SnC system discussed above, we adopted an interesting strategy to enhance the reversible capacity, cyclic stability, and rate performance of the material, namely *in situ* co-synthesis of the Fe₃SnC@CNF (CNF=Carbon Nano Fibre) composite. The detailed synthesis procedure is provided in the experimental section. Herein, the conducting carbon fibre was intended to provide a conducting support matrix to enhance the electrochemical performance. The Fe₃SnC@CNF composite compound was thoroughly characterized by Powder XRD, FESEM, EDAX and HRTEM. The PXRD data (Fig. 11a) shows the formation of Fe₃SnC phase along with the formation of carbon fibre which can be confirmed by the reference of ICSD (Inorganic Crystal Structure Database). The broad peak around 2 theta = 25° value shows the presence of carbon and the other peaks at 2 theta values 32°, 40°, 47°, 53°, 58°, 68° and 73° correspond to the formation Fe₃SnC phase. The FESEM images (Figs. 4c and 11d) show the distribution of Fe₃SnC particles on the carbon fibre matrix. The HRTEM images (Fig. 10b and inset) reveals that the Fe₃SnC particles not only distribute themselves onto the carbon fibre but are also present inside those fibres. To check the ratio of Fe and Sn for validating the formation of Fe₃SnC phase further, we performed the EDAX studies from FESEM as well as HRTEM (Fig. 12(a-d)). The overall EDAX (Figs. 12a and 12b) scan shows a weight ratio of Fe and Sn as 3:1. Just to make sure that the Fe₃SnC particles are also present inside the carbon fibre, along with HRTEM we also performed spot EDAX measurements by intentionally selecting the regions where the Fe₃SnC particles are not visible onto the carbon fibre (Fig. 12c and 12d) and this study also confirmed the expected weight ratios of Fe and Sn in support of the above-mentioned analysis.

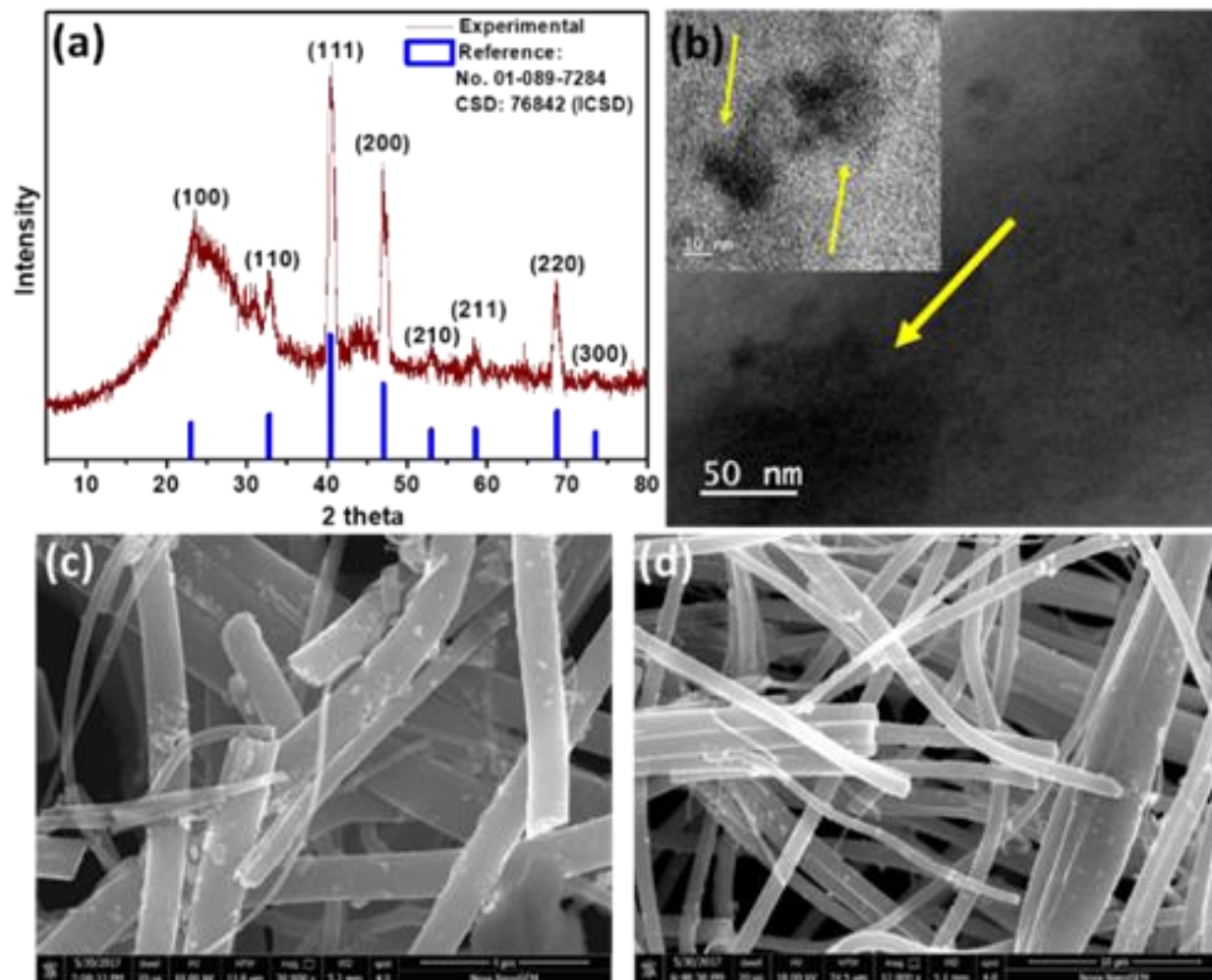


Fig 11. Characterizations of the $\text{Fe}_3\text{SnC@CNF}$ composite material: **(a)** Powder X-ray diffraction analysis, **(b)** HRTEM analysis, **(c and d)** FESEM analysis. FESEM shows the distribution of the Fe_3SnC particles on the CNF matrix while HRTEM reveals that the particles are also inside the fibres

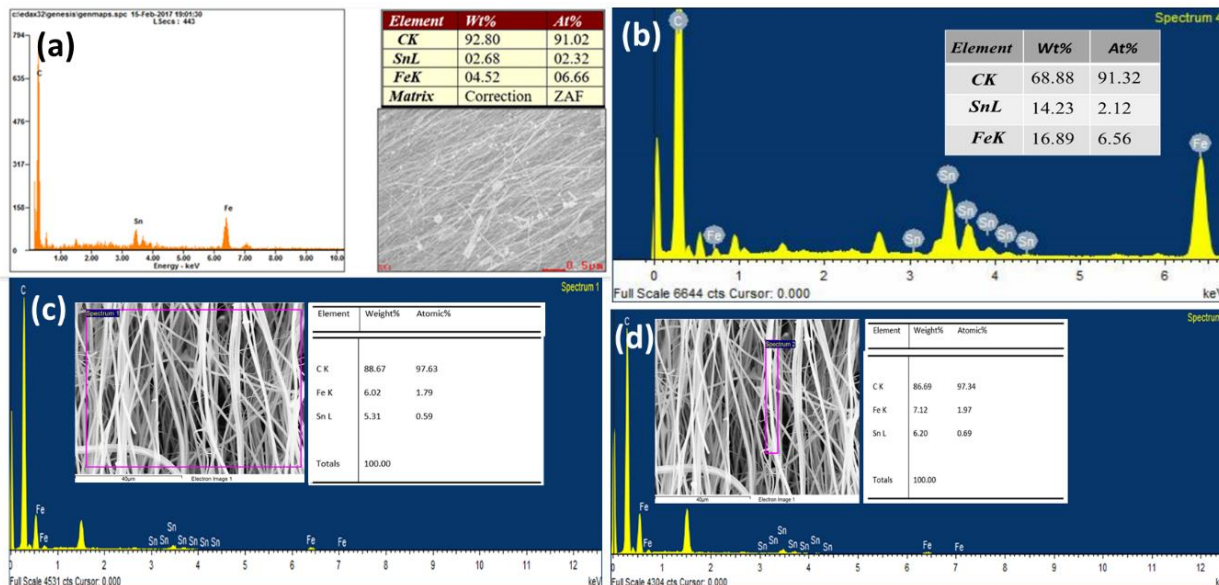


Fig 12. Characterizations of the $\text{Fe}_3\text{SnC@CNF}$ sample: (a) EDAX data from FESEM, (b) EDAX data from HRTEM, (c) and (d) Spot EDAX data from FESEM.

3.6. Electrochemical studies on $\text{Fe}_3\text{SnC@CNF}$ composite:

Now to proceed with the electrochemical performance of the $\text{Fe}_3\text{SnC@CNF}$ anode material in Li-ion battery, we performed the charge-discharge measurements at different current densities. Current densities were varied from 50 mA g^{-1} to 2 Ag^{-1} . A very impressive initial high discharge capacity of 1046 mAh g^{-1} was observed at a current density of 200 mA g^{-1} (fig 13a) with a reversible capacity of 573 mAh g^{-1} . The irreversible loss of the capacity was due to formation of solid electrolyte interphase (SEI) layer which is also reflected in the cyclic voltammetry data (Fig. 13b). But in the consecutive cycles there was no signature of formation of SEI layer leading to an extremely stable anode performance. The material managed to withstand a reversible lithiation-delithiation current density of 200 mA g^{-1} for the first 100 cycles and 1 Ag^{-1} till 1000 cycles with a $\sim 96\%$ retention of capacity (Fig. 13d) to prove itself as an ultra-stable anode material. On the other hand, the material also delivered very high power density when it was subjected to variable current densities of 50 mA g^{-1} , 100 mA g^{-1} , 200 mA g^{-1} , 500 mA g^{-1} , 1 Ag^{-1} and 2 Ag^{-1} (Fig. 13e) by showing an excellent rate performance. The material delivered a reversible capacity of more than 500 mAh g^{-1} even when exposed to a current density as high as 2

Ag^{-1} . Due to the presence of carbon to a significant extent, the charge-discharge data (fig 13a) does have a flat plateau which is again reflected in the cyclic voltammetry data. (fig 13b). However, there are formations of some small peaks in the cathodic potential window of 0.5 to 1.2 Volt which is reversible also in the anodic counterpart (marked by orange box in the figure). Those mainly correspond to the reversible uptake and release of Li by the Fe_3SnC crystals (fig. 13b) which can be correlated with the CV data of the single phase Fe_3SnC in fig 3b.

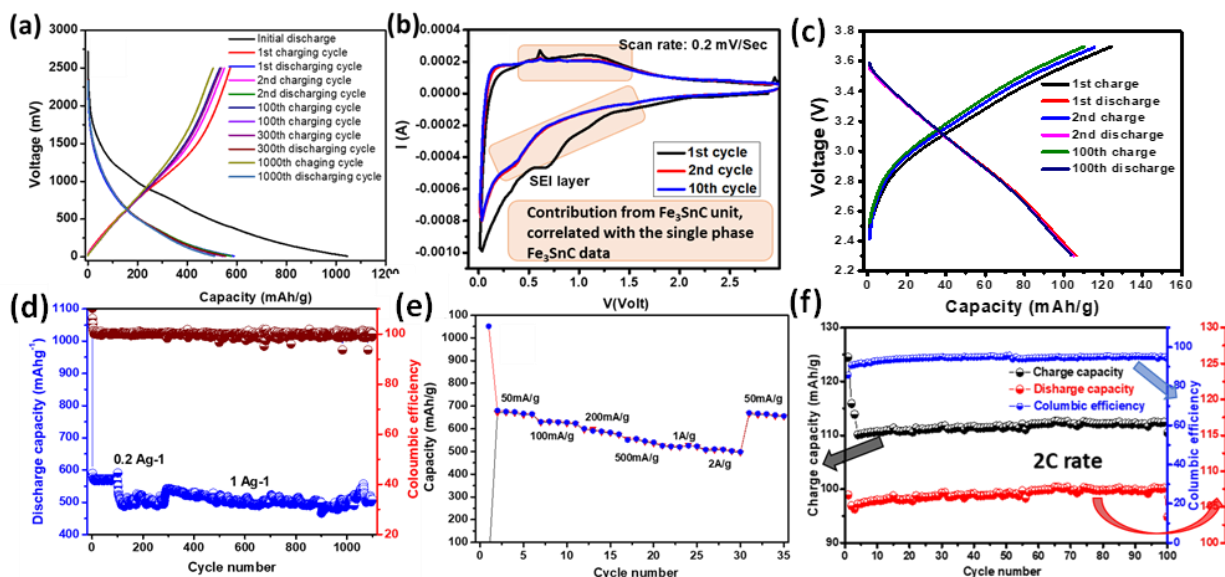


Fig 13. Electrochemical studies on the $\text{Fe}_3\text{SnC}@CNF$ sample: (a) Charge-discharge data, (b) cyclic voltammetry data, (d) stability and Coloumbic efficiency data, (e) Rate performance data. Excellent stability was observed after 1000 charge discharge cycles along with a very high capacity of 500 mAhg^{-1} even at a very high applied current density of 2Ag^{-1} . Full cell data: (c) charge-discharge data (f) stability and efficiency data

Electrochemical impedance spectroscopy (EIS) was also performed for the fresh cell (fig. 4b) and it showed very low charge transfer as well as electrochemical series resistance as compared to single phase Fe_3SnC which is due to presence of carbon fibre. In order to further probe the rete of ionic diffusion into the Fe_3SnC single phase material as well as the $\text{Fe}_3\text{SnC}@CNF$ composite system, diffusion coefficient calculations were performed from the impedance data. $\text{Fe}_3\text{SnC}@CNF$ showed a significant increase in the diffusion coefficient as compared to the

Fe₃SnC single phase system (Fig. 14) owing to the presence of conducting carbon fibre matrix resulting to an excellent rate performance proving it as a potential high power density anode.

A full cell using LiCoO₂ as a cathode was also fabricated to check the performance of the Fe₃SnC@CNF material in a practical Li-ion full battery and the performance turned out to be impressive as a high first reversible capacity of 124 mAhg⁻¹ was obtained with an initial coulombic efficiency of ~85 % retaining a reversible charge capacity of 110 mAhg⁻¹ after 100 cycles with a coulombic efficiency of ~96% at 2C rate (based on the active mass of the combining weight of the anode and cathode). (Fig. 13c and 13f). The procedure for the fabrication of the full cell can be found in the experimental section

The detailed calculation of the Warburg as well as diffusion coefficient can be found below.

Diffusion coefficients of Li ion were calculated using the following equation,

$$D = 0.5(RT/AF^2\sigma C)^2$$

Where, R is the universal gas constant (8.314 J mol⁻¹ K⁻¹), T is the temperature (298.5 K), A is the area of the electrode surface (1.14 cm²), F is the Faraday's constant (9.65 × 10⁴ C mol⁻¹),

C is the molar concentration of Li⁺, and σ is the Warburg coefficient.

Warburg co-efficient, σ can be calculated using the following equation:

$$Z_{re} = R_e + R_{ct} + \sigma\omega^{-0.5}$$

where σ is the slope for the plot of Z_{re} vs. the reciprocal root square of the lower angular frequencies ($\omega^{-0.5}$).

Warburg co-efficient, σ for single phase Fe₃SnC turns out to be 27.22 whereas, for Fe₃SnC@CNF it is 20.63. Corresponding calculated values of diffusion co-efficient are 4.2*10⁻¹⁰ cm²s⁻¹ and 7.3*10⁻¹⁰ cm²s⁻¹ for single phase Fe₃SnC and Fe₃SnC@CNF respectively.

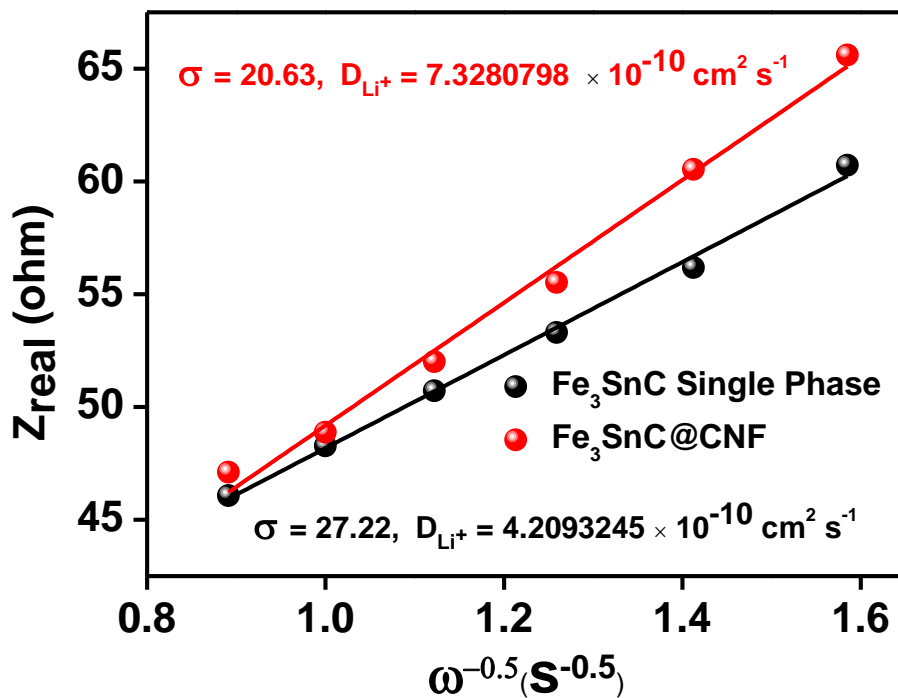


Fig 14. Z_{real} vs $\omega^{-0.5}$ plots for Fe₃SnC single phase and the Fe₃SnC@CNF composite.

Projected material	Initial discharge capacity	Current density (mA ^g ⁻¹ /C-rate)	First reversible capacity	Reversible capacity (stability)	References
Ti ₃ C ₂ T _x	410	0.1 C	250	147.4 at 1 C after 100 cycles	Kong, F.; He, X.; Liu, Q.; Qi, X.; Zheng, Y.; Wang, R.; Bai, Y. <i>Electrochim. Acta</i> 2018 , <i>265</i> , 140-150.
V ₂ CT _x	380	1C	210	260 at 1 C after 150 cycles	Naguib, M.; Halim, J.; Lu, J.; Cook, K. M.; Hultman, L.; Gogotsi, Y.; Barsoum, M. W. <i>J. Am. Chem. Soc.</i> 2013 , <i>135</i> , 15966-15969.
V ₂ C	467	370	291	243 at 0.5 A g ⁻¹ after 500 cycles	Liu, F.; Zhou, J.; Wang, S.; Wang, B.; Shen, C.; Wang, L.; Hu, Q.; Huang, Q.; Zhou, A. <i>J. Electrochem. Soc.</i> 2017 , <i>164</i> , A709-A713.
MoS ₂ @Ti ₃ C ₂	386.4	50	245	131.6 at 1 A g ⁻¹ after 200 cycles	Shen, C.; Wang, L.; Zhou, A.; Zhang, H.; Chen, Z.; Hu, Q.; Qin, G. <i>J. Electrochem. Soc.</i> 2017 , <i>164</i> , A2654-A2659.
Nb ₂ CT _x	422	1C	250	170 at 1 C after 150 cycles	Naguib, M.; Halim, J.; Lu, J.; Cook, K. M.; Hultman, L.; Gogotsi, Y.; Barsoum, M. W. <i>J. Am. Chem. Soc.</i> 2013 , <i>135</i> , 15966-15969.
Mo ₂ C-C	1054.3	100	940	777.7 at 1 A g ⁻¹ after 1000 cycles	Xiao, Y.; Zheng, L.; Cao, M. <i>Nano Energy</i> 2015 , <i>12</i> , 152-160.
Fe@Fe ₃ C/C	941.1	50	505	382.2 at 0.2 A g ⁻¹ after 30 cycles	Su, L.; Zhou, Z.; Shen, P. <i>Electrochim. Acta</i> 2013 , <i>87</i> , 180-185.
Mo ₂ C-NCNFs	1070.9	100	790	411.9 at 2 A g ⁻¹ after 50 cycles	Li, R.; Wang, S.; Wang, W.; Cao, M. <i>Phys. Chem. Chem. Phys.</i> 2015 , <i>17</i> , 24803-24809.

SiC nanofibers	309.3	100	210	504.1 at 0.3 A g ⁻¹ after 500 cycles	Sun, X.; Shao, C.; Zhang, F.; Li, Y.; Wu, Q. -H.; Yang, Y. <i>Front. Chem.</i> 2018 , <i>6</i> , 166.
Ti ₃ C ₂ /CNF	848	1 C	407	320 at 1C after 295 cycles	Lin, Z.; Sun, D.; Huang, Q.; Yang, J.; Barsoum, M. W.; Yan, X. <i>J. Mater. Chem. A</i> 2015 , <i>3</i> , 14096-14100.
Fe₃SnC@C NF (Present work)	1060	100	604	510 at 1 A g⁻¹ after 1000 cycles	This work.

Table 4. Comparison table of different carbide materials used as anodes for Li-ion battery

4. Conclusion:

In conclusion, we report for the first time, a ternary intermetallic 3D carbide with unique antiperovskite structure involving both transition (Fe) and post transition (Sn) metals, namely Fe₃SnC, as a stable high capacity anode material for Li ion battery. DFT based computational studies reveal that Li insertion results in deviation from the cubic anti-perovskite structure with a volume expansion that induces significant strain in the electrode as is evident from the XRD and SAED data. We have also in-situ synthesized Fe₃SnC Carbon Nano Fiber (CNF) composite and realized a very impressive cyclic stability. Initial discharge capacity was found to be 1045 mAhg⁻¹ and along with a stable reversible capacity of 600 mAhg⁻¹ at 200 mA g⁻¹ and 500 mAhg⁻¹ at 1 Ag⁻¹ after 1000 charge discharge cycle with almost ~96% retention of capacity. Similarly, exceptionally high rate performance was observed with a high value of ~500 mAhg⁻¹ obtained even at a current of 2 Ag⁻¹. The full cell with LCO cathode delivered a high reversible capacity of 110 mAhg⁻¹ after 100 cycles with a very good stability. CNF loaded Fe₃SnC is thus projected as a novel and very efficient material among the 3D carbide systems with the corresponding Li storage performance competing the best materials. We believe that this work will open up various new possibilities to focus on intermetallics and 3D carbide systems to be explored in the field of energy storage.

5. References:

- [1] E. Environ, V. Etacheri, R. Marom, R. Elazari, G. Salitra, D. Aurbach, *Energy Environ. Sci.* **2011**, *4*, 3243.
- [2] P. Roy, S. Kumar, *J. Mater. Chem. A* **2015**, *3*, 2454.
- [3] N. Nitta, F. Wu, J. T. Lee, G. Yushin, *Materials Today* **2015**, *18*, 252.
- [4] J. B. Goodenough, K. S. Park, *J. Am. Chem. Soc.* **2013**, *135*, 1167.
- [5] M. N. Obrovac, V. L. Chevrier, *Chem. Rev.* **2014**, *114*, 11444.
- [6] Y. Lu, L. Yu, X. W. (David) Lou, *Chem* **2018**, *4*, 972.
- [7] D. Puthusseri, M. Wahid, S. Ogale, *ACS Omega* **2018**, *3*, 4591.
- [8] U. Kumar Sen, A. Shaligram, S. Mitra, *ACS Appl. Mater. Interfaces* **2014**, *6*, 14311.
- [9] L. S. Roselin, R. Juang, C. Hsieh, S. Sagadevan, A. Umar, R. Selvin, H. H. Hegazy, *Materials (Basel)*. **2019**, *12*, 1229.
- [10] P. Bo, Z. Sha, Q. Pei, Z. Ding, J. Jiang, V. Sorkin, Y. W. Zhang, J. Jiang, H. S. Park, Z. Bao, M. R. Weatherspoon, S. Shian, Y. Cai, P. D. Graham, S. M. Allan, G. Ahmad, M. B. Dickerson, B. C. Church, Z. Kang, H. W. A. Iii, C. J. Summers, M. Liu, K. H. Sandhage, X. Su, Q. Wu, J. Li, X. Xiao, A. Lott, W. Lu, B. W. Sheldon, J. Wu, **2014**, *33*, 172.
- [11] C. Chae, H. J. Noh, J. K. Lee, B. Scrosati, Y. K. Sun, *Adv. Funct. Mater.* **2014**, *24*, 3036.
- [12] Z. Lu, N. Liu, H. W. Lee, J. Zhao, W. Li, Y. Li, Y. Cui, *ACS Nano* **2015**, *9*, 2540.
- [13] Y. Yang, M. T. McDowell, A. Jackson, J. J. Cha, S. S. Hong, Y. Cui, *Nano Lett.* **2010**, *10*, 1486.
- [14] B. Wang, X. Li, X. Zhang, B. Luo, M. Jin, M. Liang, S. A. Dayeh, S. T. Picraux, L. Zhi, *ACS Nano* **2013**, *7*, 1437.
- [15] J. Y. Li, Q. Xu, G. Li, Y. X. Yin, L. J. Wan, Y. G. Guo, *Mater. Chem. Front.* **2017**, *1*, 1691.
- [16] Q. Xu, J. Y. Li, J. K. Sun, Y. X. Yin, L. J. Wan, Y. G. Guo, *Adv. Energy Mater.* **2017**, *7*, 1.
- [17] K. Roy, M. Wahid, D. Puthusseri, A. Patrike, S. Muduli, R. Vaidhyathan, S. Ogale, *Sustain. Energy Fuels* **2019**, *3*, 245.

- [18] H. Ying, W. Q. Han, *Adv. Sci.* **2017**, *4*, DOI 10.1002/advs.201700298.
- [19] A. Chemistry, *Communications* **2008**, 1679.
- [20] M. S. Whittingham, *Chem. Rev.* **2014**, *114*, 11414.
- [21] D. Yang, J. Zhu, X. Rui, H. Tan, R. Cai, H. E. Hoster, D. Y. W. Yu, H. H. Hng, Q. Yan, *ACS Appl. Mater. Interfaces* **2013**, *5*, 1093.
- [22] S. Huang, C. Meng, M. Xiao, S. Ren, S. Wang, D. Han, Y. Li, Y. Meng, *Sustain. Energy Fuels* **2017**, *1*, 1944.
- [23] R. C. De Guzman, J. Yang, M. Ming-Cheng Cheng, S. O. Salley, K. Y. S. Ng, *J. Mater. Chem. A* **2014**, *2*, 14577.
- [24] A. Ulvestad, H. F. Andersen, I. J. T. Jensen, T. T. Mongstad, J. P. Maehlen, O. Prytz, M. Kirkengen, *Sci. Rep.* **2018**, *8*, 1.
- [25] Y. Zhong, X. H. Xia, F. Shi, J. Y. Zhan, J. P. Tu, H. J. Fan, *Adv. Sci.* **2015**, *3*, DOI 10.1002/advs.201500286.
- [26] X. Tang, X. Guo, W. Wu, G. Wang, *Adv. Energy Mater.* **2018**, *8*, 1.
- [27] M. Naguib, J. Halim, J. Lu, K. M. Cook, L. Hultman, Y. Gogotsi, M. W. Barsoum, *J. Am. Chem. Soc.* **2013**, *135*, 15966.
- [28] M. Naguib, J. Come, B. Dyatkin, V. Presser, P. L. Taberna, P. Simon, M. W. Barsoum, Y. Gogotsi, *Electrochem. commun.* **2012**, *16*, 61.
- [29] I. H. Son, J. H. Park, S. Kwon, S. Park, M. H. Rummeli, A. Bachmatiuk, H. J. Song, J. Ku, J. W. Choi, J. M. Choi, S. G. Doo, H. Chang, *Nat. Commun.* **2015**, *6*, 1.
- [30] H. Zhang, Z. Fu, R. Zhang, Q. Zhang, H. Tian, D. Legut, T. C. Germann, Y. Guo, S. Du, J. S. Francisco, *Proc. Natl. Acad. Sci.* **2017**, *114*, E11082.
- [31] Y. Yu, Z. Guo, Q. Peng, J. Zhou, Z. Sun, *J. Mater. Chem. A* **2019**, *7*, 12145.
- [32] D. Er, J. Li, M. Naguib, Y. Gogotsi, V. B. Shenoy, *ACS Appl. Mater. Interfaces* **2014**, *6*, 11173.
- [33] M. Li, S. Yu, Z. Chen, Z. Wang, F. Lv, B. Nan, Y. Zhu, Y. Shi, W. Wang, S. Wu, H. Liu, Y. Tang, Z. Lu, *Inorg. Chem. Front.* **2017**, *4*, 289.
- [34] Q. Tang, Z. Zhou, P. Shen, *J. Am. Chem. Soc.* **2012**, *134*, 16909.
- [35] M. J. Sun, X. Cao, Z. Cao, *Nanoscale* **2018**, *10*, 10450.
- [36] N. N. Wang, D. F. Shao, W. J. Lu, H. Y. Lu, *J. Appl. Phys.* **2016**, *119*, DOI 10.1063/1.4940723.

- [37] M. Bilal, I. Ahmad, S. J. Asadabadi, R. Ahmad, M. Maqbool, *Electron. Mater. Lett.* **2015**, *11*, 466.
- [38] S. AL, A. İYİGÖR, *Süleyman Demirel Üniversitesi Fen Bilim. Enstitüsü Derg.* **2018**, *22*, 482.
- [39] B. S. Wang, P. Tong, Y. P. Sun, X. B. Zhu, Z. R. Yang, W. H. Song, J. M. Dai, *Appl. Phys. Lett.* **2010**, *97*, 1.
- [40] T. Chen, B. Cheng, R. Chen, Y. Hu, H. Lv, G. Zhu, Y. Wang, L. Ma, J. Liang, Z. Tie, Z. Jin, J. Liu, *ACS Appl. Mater. Interfaces* **2016**, *8*, 26834.
- [41] Y. Qi, L. G. Hector, C. James, K. J. Kim, *J. Electrochem. Soc.* **2014**, *161*, F3010.
- [42] N. Zhang, Q. Zhao, X. Han, J. Yang, J. Chen, *Nanoscale* **2014**, *6*, 2827.
- [43] Y. Xu, J. Guo, C. Wang, *J. Mater. Chem.* **2012**, *22*, 9562.
- [44] S. Haldar, K. Roy, S. Nandi, D. Chakraborty, D. Puthusseri, Y. Gawli, S. Ogale, R. Vaidhyanathan, *Adv. Energy Mater.* **2018**, *8*, 1.
- [45] Y. Guo, X. Zeng, Y. Zhang, Z. Dai, H. Fan, Y. Huang, W. Zhang, H. Zhang, J. Lu, F. Huo, Q. Yan, *ACS Appl. Mater. Interfaces* **2017**, *9*, 17172.
- [46] Y. Xu, Q. Liu, Y. Zhu, Y. Liu, A. Langrock, M. R. Zachariah, C. Wang, *Nano Lett.* **2013**, *13*, 470.
- [47] L. Ji, Z. Tan, T. Kuykendall, E. J. An, Y. Fu, V. Battaglia, Y. Zhang, *Energy Environ. Sci.* **2011**, *4*, 3611.
- [48] P. Giannozzi, S. Baroni, N. Bonini, M. Calandra, R. Car, C. Cavazzoni, D. Ceresoli, G. L. Chiarotti, M. Cococcioni, I. Dabo, A. Dal Corso, S. De Gironcoli, S. Fabris, G. Fratesi, R. Gebauer, U. Gerstmann, C. Gougoussis, A. Kokalj, M. Lazzeri, L. Martin-Samos, N. Marzari, F. Mauri, R. Mazzarello, S. Paolini, A. Pasquarello, L. Paulatto, C. Sbraccia, S. Scandolo, G. Sclauzero, A. P. Seitsonen, A. Smogunov, P. Umari, R. M. Wentzcovitch, *J. Phys. Condens. Matter* **2009**, *21*, 39, 395502.
- [49] D. Vanderbilt, *Phys. Rev. B* **1990**, *41*, 7892.
- [50] J. P. Perdew, K. Burke, M. Ernzerhof, *Phys. Rev. Lett.* **1996**, *18*, 3865.
- [51] M. Cococcioni, S. De Gironcoli, *Phys. Rev. B - Condens. Matter Mater. Phys.* **2005**, *71*, 1.
- [52] V. I. Anisimov, J. Zaanen, O. K. Andersen., *Phys. Rev. B* **1991**, *44*, 943.

- [53] V. I. Anisimov, I. V. Solovyev, M. A. Korotin, M. T. Czyzyk, G. A. Sawatzky, *Phys. Rev. B* **1993**, *48*, 16929.
- [54] V. I. Anisimov, O. Gunnarsson, *Phys. Rev. B* **1991**, *43*, 7570.
- [55] J. D. Pack, H. J. Monkhorst, *J. Chem. Inf. Model.* **2013**, *53*, 1689.
- [56] N. Marzari, D. Vanderbilt, A. De Vita, M. C. Payne, *Phys. Rev. Lett.* **1999**, *82*, 3296.
- [57] B. S. Wang, P. Tong, Y. P. Sun, X. B. Zhu, Z. R. Yang, W. H. Song, J. M. Dai, *Appl. Phys. Lett.* **2010**, *97*, 1.
- [58] F. G. Gerard, A, *J. Phys. F Met. Phys.* **1976**, *6*, 451.
- [59] A. L. Ivanovskii, R. F. Sabiryanov, A. N. Skazkin, *Phys. Solid State*, **2002**, *40*, 1516

Chapter 3

Room temperature processed in-situ carbon-coated vanadium carbide (VC@C) as a high capacity robust Li/Na battery anode material

3D carbide systems with their robust physical and mechanical properties have always attracted multiple application interests. In this report, we have synthesized a three-dimensional in-situ carbon coated cubic carbide, Vanadium Carbide (VC@C), by a very simple, scalable and cost-effective room temperature mechano-chemical ball-milling procedure and researched its promise as effective anode material for Li and Na ion batteries. We have demonstrated that VC@C shows an impressive initial discharge/lithiation capacity of 1165 mAh g⁻¹ with a high reversible capacity of 640 mAh g⁻¹ after 100 charge-discharge cycles at an applied current density of 0.1 A g⁻¹. We have also found that this material renders a very promising rate performance with significantly low capacity drop after exposing it to variable current densities ranging from 0.05 A g⁻¹ to 2 A g⁻¹ with an excellent stability up to 1000 cycles owing to its structural robustness, as verified by post-cycling characterizations. A Li-ion full cell study using LiCoO₂ as cathode also showed excellent promise in terms of practical application demonstrating a reversible capacity of 95 mAh g⁻¹ after 100 cycles. Even for Na insertion/de-insertion VC@C shows a clear promise in terms of capacity, cyclic stability and rate performance.

Related publication: *Carbon*, 2020 ,161, 108-116

Declaration

The text and the figures being reproduced in this chapter are from my own co-authored publication “*Carbon, 2020,161, 108-116*” with the permission from the publisher.

I acknowledge Dr. Mani Mahajan for conceptualizing the novel room temperature synthesis of the material and her active help in device fabrication and testing.

1. Introduction:

Development of rechargeable lithium-ion-battery (LIBs) technology ushered a new revolution in the electrical energy storage space which has witnessed major successes over the past few decades. This has favoured the emergence of multiple applications, especially in the sector of clean and renewable energy.¹⁻³ This has continued to necessitate an evolution in the alkali ion battery technologies with demands for higher energy and power density, lighter weight, low cost, and enhanced cycling stability. The key to achieve these requirements mainly depends on the property of electrode materials.³⁻⁵ Therefore, a major effort is being constantly expended towards the designing of high capacity anode materials for new generation LIBs/SIBs (sodium-ion-battery). Although graphite for LIBs and different forms of hard (turbostratic) carbons for SIBs show great promise as anodes in terms of capacity, cyclic stability and coulombic efficiency, they lack in their theoretical capacity limit (e.g. 372 mAh g⁻¹ for graphite as LIB anode).⁴⁻⁶ Hence copious research is being performed on designing several other high-capacity anode materials like transition metal oxides (TMO), transition metal sulfides (TMS) as conversion materials, Si, Ge, Sn, P based materials as alloying types etc. which render capacities far beyond the value of commercialized graphite for LIB and have continued to attract great attention.⁷⁻¹⁴ Unfortunately, the practical application of these materials is still not realized due to low electronic conductivity, volume expansion during cycling leading to pulverization, voltage hysteresis, and particle aggregation during the repeated lithium/sodium insertion/de-insertion processes, which lead to low rate performance, voltage decay as well as poor cycling stability.^{3,5,7,15,16}

To overcome these issues, in recent studies two crucial strategies have been adopted to enhance the electrical conductivity as well structural stability of anode materials. One strategy is to prepare the anode material on the nano-scale to reduce the diffusion path length of ions and buffering the volume variation during the discharge and charge processes. Another strategy is to improve the lithium storage and cycling performance by mixing the nano-crystals with conductive additives like graphene, carbon nanotubes, graphitic carbons, phosphorene etc., which not only accommodate the mechanical strain, but also increase the electrical conductivity and structural flexibility of the composite material, and also prevent the aggregation of the active materials during cycling.^{5,7,17} Moreover, the solid electrolyte interphase (SEI) layer formed on

carbon surfaces have also been found to be relatively stable.^{18,19} Until now, various forms of functional carbon based composite anode materials have been reported by various research groups for LIBs/SIBs (e.g. CoP_3/C , FeP_2/C , CaMoO_4/C , $\text{Fe}_3\text{O}_4/\text{GNS}$, $\text{Fe}_3\text{O}_4\text{-C}$, $\text{Li}_4\text{Ti}_5\text{O}_{12}/\text{C}$, $\text{Mn}_3\text{O}_4/\text{C}$, $\text{LiNi}_{0.8}\text{Co}_{0.1}\text{Mn}_{0.1}\text{O}_2/\text{GR}$, SnO_2/rGO , Si/C , $\text{CNTs}/\text{C}/\text{CO}_{1-x}\text{S}$).^{4,18,20-26} Their results have indicated that suitably designed and engineered composites of carbon with active materials indeed exhibit enhanced electrochemical performance in terms of charge discharge cycling, rate performance, and capacity.

Recently, materials belonging to a new family of transition-metal carbides (TMCs) have attracted a wide interest in terms of catalytic and electrochemical applications due to their high electrical and thermal conductivities, excellent mechanical as well as chemical stability along with resistance against corrosion in reaction conditions.²⁷⁻²⁹ Thus, the potential possibility of TMCs as energy storage materials in LIBs/SIBs has been and is being investigated vigorously in terms of both experiment and theory. Gogotsi and coworkers have explored and demonstrated the viability of a series of two-dimensional carbides (V_2C , Nb_2C , Ti_3C_2 , Cr_2C etc.) in this context, opening a new window for the investigation of carbides as one of the promising classes of potential materials for energy storage devices.^{28,30-33} In addition, among non-layered carbide materials, Wang et al. prepared $\text{Mo}_2\text{C}/\text{GR}$ hybrids which exhibited much better lithium storage properties, reflecting their potential for application as anode materials in lithium-ion batteries.³⁴ Su et al. have also prepared a nanocomposite of $\text{Fe}/\text{Fe}_3\text{C}/\text{C}$, which delivered a better reversible capacity along with structural stability during lithium insertion/de-insertion process.³⁵ Qiu et al. have developed hollow carbon nitride hierarchical microspheres with ultrafine N-doped MoC (MoC_xN_y), which showed remarkable cycle stability with high specific capacity due to buffering in the volume change and inhibited the aggregation of nanoparticles upon sodiation/desodiation.³⁶ Yang et al. have fabricated nanohybrids of vanadium carbide nanoparticles decorated with reduced graphene oxide (RGO) ($\text{V}_8\text{C}_7/\text{RGO}$) and reported high reversible specific capacity, and long cycle life with an excellent rate performance for LIBs.³⁷

Inspired by the above results and considering the advantages of using carbon with TMCs, in this report we demonstrate lithium as well as sodium storage performance of single-step room temperature synthesized carbon encapsulated three-dimensional Vanadium Carbide nanoparticles (VC/C) as an anode material in LIBs/SIBs. Most importantly, our protocol of

single-step room temperature mechano-chemical ball-milling renders *in-situ* carbon encapsulated VC (VC@C) nanocomposites with three-dimensional (3D) core-shell structure without further heating or using any external substrate. This material is shown to exhibit impressive rate capability, high cycling stability, and capacity retention as anode material both for the LIBs and SIBs systems, owing to its unique morphology and metal ion hosting capability. To the best of our knowledge, among all the state-of-the-art TMC-based electrode materials synthesized by different techniques, the current material (VC@C) stands tall with the unique room temperature synthetic strategy as well as impressive electrochemical performance.

2. Experimental section:

2.1. Raw materials used:

The raw materials used for preparing the carbon-coated vanadium carbide nanocomposite (VC@C) were vanadium pentoxide, V₂O₅ (99%, Loba Chemie), magnesium metal powder, Mg (99%, Loba Chemie) and activated charcoal, C (99%, S.D. fine chemicals). All these materials were used without any further purification.

2.2. Materials and Methods:

For the mechano-chemical synthesis of VC@C nanocomposite, fixed amount of V₂O₅ (Vanadium pentoxide, 2 g), magnesium (Mg, 2.5 g) and activated charcoal (1 g) were used as the starting materials. The milling was carried out at room temperature using a planetary ball mill (RETSCH PM 100) with the rotation speed of 300 RPM for constant time period of 15 h in tungsten carbide (WC) jar of 250 mL capacity. Tungsten carbide (WC) balls with diameter 10 mm and weight 7.7 g was used as a milling media. The ball-to-powder weight ratio was kept constant (20:1). To remove the by-product of the milling, the as-milled powders were treated with (1:1) HCl followed by the washing with water several times to maintain the neutrality of the solution. The final powder was then dried in the oven at 120 °C for 12 h.

2.3. Characterizations:

X-ray diffraction (XRD) was done using Philips PANalytical X'Pert – PRO with CuK α radiation ($\lambda = 1.54 \text{ \AA}$). Micro-structural features of the sample were examined using FE-SEM (Zeiss Ultra Plus instrument) and high-resolution TEM (TECHNAI G) at 200 kV. Raman spectrum was recorded using Ar⁺ excitation source of 514.5 nm wavelength with a Renishaw-Invia micro-Raman spectrometer. The Brunauer–Emmett–Teller (BET) surface area was calculated from N₂ adsorption/desorption isotherms at 77 K using Micromeritics Gas Adsorption Analyser (Tristar 3000). Thermo-gravimetric and Differential scanning calorimetry (TG-DSC) were carried out in the heating cycle mode at a rate of 5°/min using NETZSCH STA 449F3 thermal analyser. The spectrum was obtained in the temperature range of 0–900 °C in air atmosphere. X-ray photoelectron spectrum (XPS) was collected on a Thermo Fisher Scientific Instruments, U.K. instrument.

2.4. Electrode and Coin Cell Preparation for Electrochemical Measurement:

Electrochemical tests were performed using 2032 coin cell assembly with Li/Na metal as the reference electrode. The carbon-coated vanadium carbide electrodes were prepared by mixing the active materials VC@C, conducting carbon (Super-P) and binder Polyvinylidene fluoride (PVDF) in the weight ratio of 7:2:1 using N-methyl-2-pyrrolidone (NMP) as the solvent. The mixture was spread onto the Cu foil uniformly and dried overnight at 80 °C. The material-coated foil was then punched into circular discs for electrodes. The mass loading of active material was in the range of 1.0 – 1.8 mg. The coin cells were assembled inside an argon-filled glove box. The electrolyte used was 1M LiPF₆/NaClO₄ in 1:1 v/v ethylene carbonate (EC)/di-methyl carbonate (DMC) for LIBs and SIBs, respectively with 5 % fluoroethylene carbonate (FEC). Celgard and whatman separators were used for Li-ion and Na-ion, respectively. Galvanostatic charge/discharge measurements were carried out using a multi-channel BTS-Neware battery tester. Cyclic voltammograms (CV) and impedance were recorded using Biologic EC Lab SP 300 at a scan rate of 0.2 mV/s.

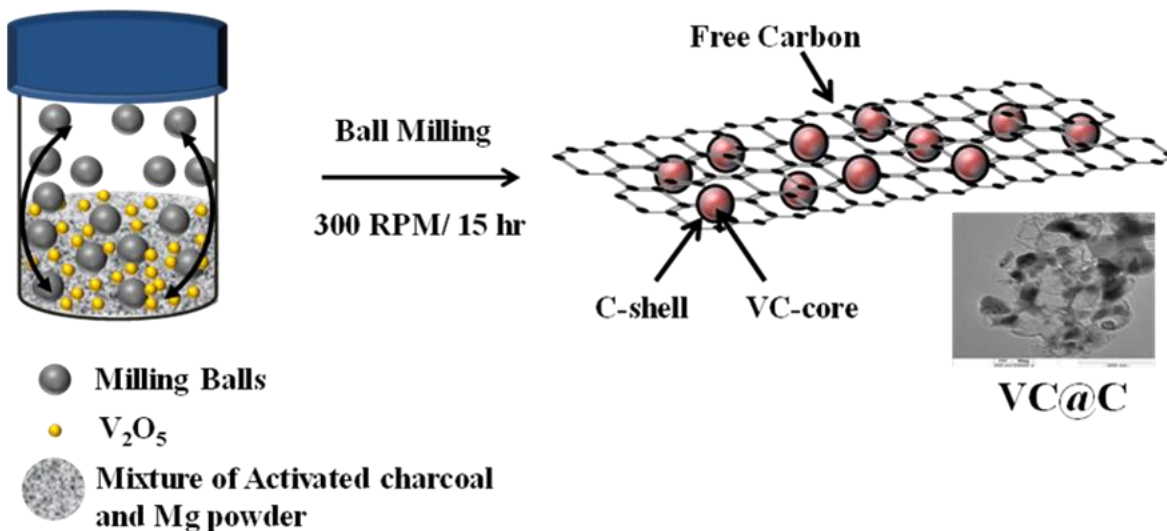
2.5. Full cell fabrication:

The full cell was fabricated by employing the electrochemical activation technique. The VC@C anode and the LiCoO₂ cathode were electrochemically activated first (One lithiation-delithiation cycle) followed by a full cell fabrication using the activated electrodes. LiPF₆ in EC:DMC (1:1) along with 5 vol % FEC was used as the electrolyte and Celgard was used as separator.

3. Result and discussions:

3.1. Material characterizations:

During the ball-milling process, the local inter-particle impact energy generated at high RPM is sufficient enough in several cases involving oxide or other materials to enable the chemical reaction to occur through continuously generated fresh surfaces, defects, deformations, and creation of active sites with the passage of time, even at ambient room temperature.³⁸ Grain refinement because of the fragmentation results in the build-up of the internal stresses, which helps to reduce the particle size.^{39,40} At such high RPM value, the deformations and fragmentation of oxide particles becomes more which enables the reduction/carburization process at faster rate to facilitate the growth of crystalline VC phase as shown in **Fig. 1a**. The appearance of diffraction peaks corresponding to 2θ at 37.3°, 43.4°, 63.0°, 75.6° and 79.6° confirms the formation of cubic VC (ICDD Card No. 01-073-0476) of NaCl type structure.⁴¹ The schematic representation for the synthesis of VC@C is shown in **Scheme 1**.



Scheme 1. Schematic diagram for the synthesis of carbon-coated vanadium carbide VC@C.

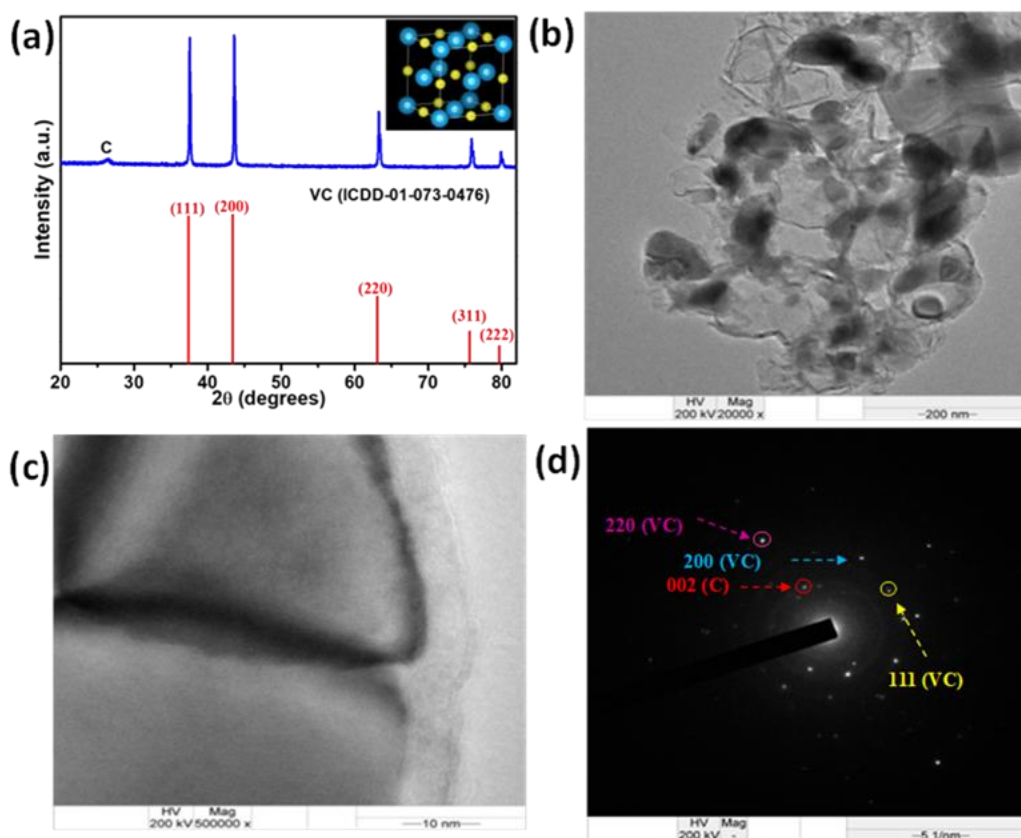


Figure 1. (a) Powder x-ray diffraction data of the VC@C along with the ICDD reference data; (b) TEM image of the as-synthesized VC@C material; (c) HRTEM image revealing the carbon coated VC system; (d) Selected area electron diffraction (SAED) pattern of the VC@C material.

Lower surface area of $32.4 \text{ m}^2\text{g}^{-1}$ and pore size of 3.7 nm of the synthesized VC@C is noted from the BET analysis (**Fig. 2a**). Lower value of I_D/I_G ratio and emergence of 2D band observed in **Fig. 2b** indicates the improved local structural order in VC@C.⁴² FESEM and EDAX images confirm the formation of irregular particles with large aggregates as a result of continuous fracture and welding of the particles at high RPM with the existence of vanadium and carbon as shown in **Fig. 3(a and b)**. VC particles of average diameter of 100 nm embedded in carbon layers can be clearly seen from the TEM analysis as shown in **Fig. 1b**. The particles of VC tend to join with each other because of the agglomeration occurring at high RPM due to the intense milling. Interconnected VC particles coated by outer carbon layers can be clearly inferred from HRTEM analysis shown in **Fig. 1c**. The interplanar spacings (averaged) of these layers and that of core particle is about 0.35 and 0.21 nm, which corresponds to the (002) and (200) plane of C and VC, respectively (**Fig. 4**), which represents an appropriate choice for reversible intercalation and de-intercalation of Li/Na ions.⁶ The SAED pattern taken from the nanocrystalline region shows the reflections of crystalline phase of cubic VC and carbon **Fig. 1d**. These interconnected 3D ordered porous structures are a unique feature which enhances the mechanical strength and shortens the diffusion path of ions which ensures better performance and long-term cyclic stability as an electrode material in energy storage devices.⁴³ The carbon content in the VC@C composite is confirmed by TG analysis (**Fig. 5**) and it turns out to be ~36 %. The detail discussions and calculations regarding the TGA can be found in the supporting information (Page 5 and 6). In the high resolution V2p X-ray photoelectron spectroscopy (XPS) data, the peaks with binding energies of 517.09 and 524.24 eV shown in **Fig. 6** could be assigned to V $2p_{3/2}$ and V $2p_{1/2}$. After deconvolution of V $2p_{3/2}$ band, three bands at 513.5, 515.7 and 517.0 eV, assigned to V atoms in V–V, V–O and V–C bonding configurations, respectively appear as in **Fig. 6**.⁴⁴ The V–O bonds result from the surface absorption of oxygen molecules resulting in the lower binding energy than that of V–C bonds.

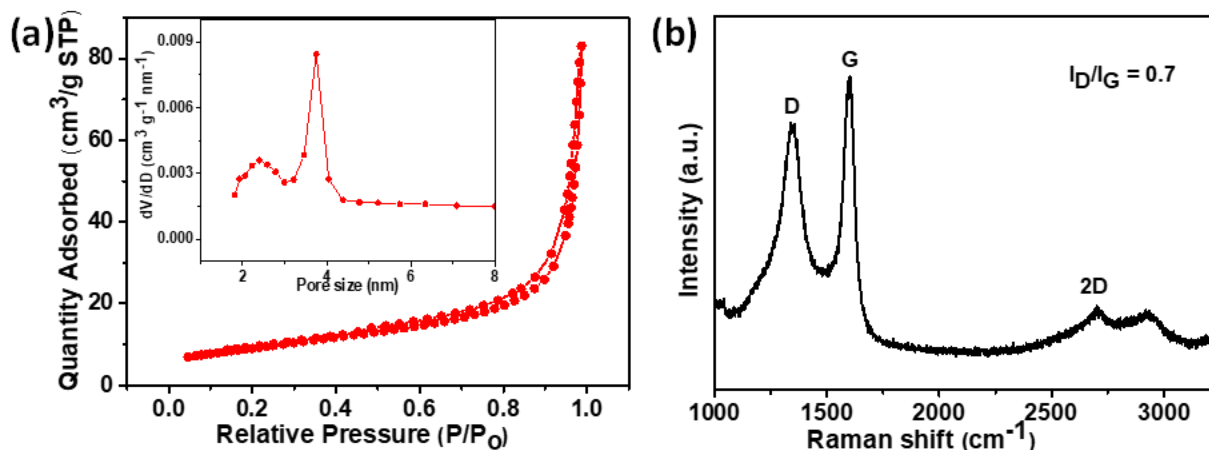


Figure 2. (a) N₂ adsorption-desorption isotherm and Pore size distribution curve (inset); (b) Raman spectrum of VC@C. (The formation of crystalline VC in VC@C is considered to be a result of mechanically induced self-sustaining reactions (MSR) initiated by energy induced at high RPM (300).¹ During extensive milling at high RPM (300), high energy is imparted to the particles being milled and eventually, particles started to agglomerate in order to reduce their surface free energy. Similar behaviour was also observed by many authors during high intensity dry grinding of materials.^{2,3} As a result of this, lower surface area of 32.4 m²g⁻¹ and pore size of 3.7 nm has been reflected from BET analysis)

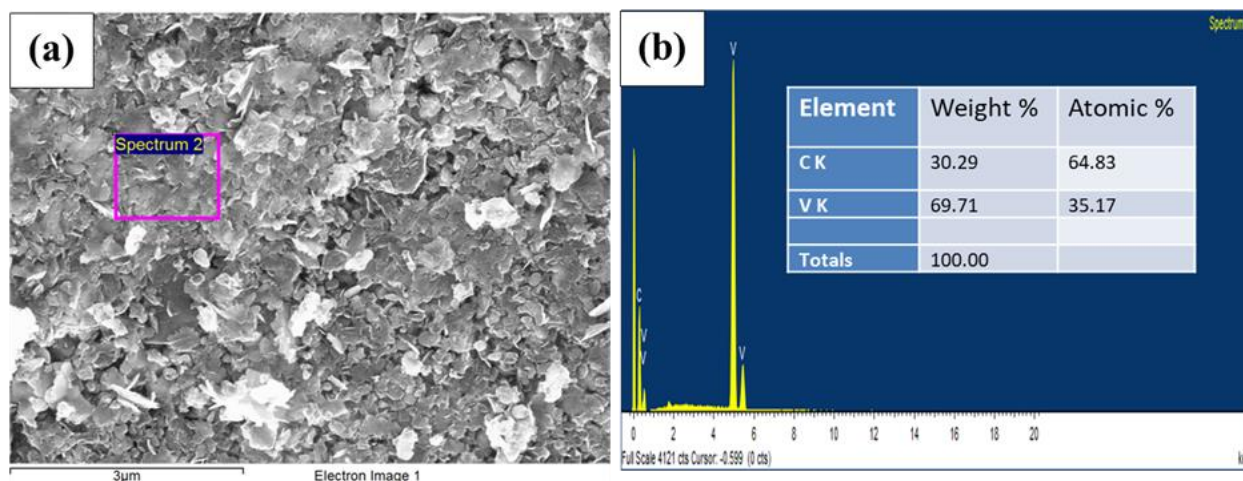


Figure 3. (a) FESEM; (b) EDAX images of VC@C.

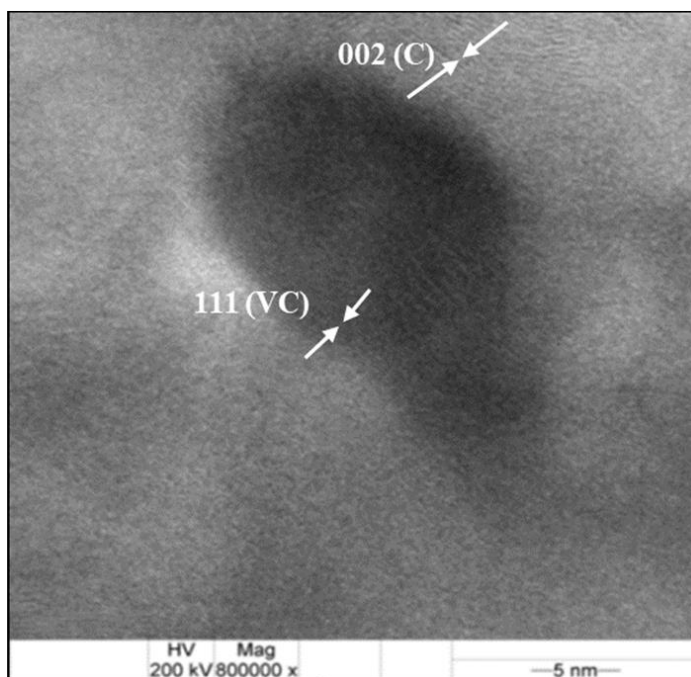


Figure 4. HRTEM image of the VC@C material.

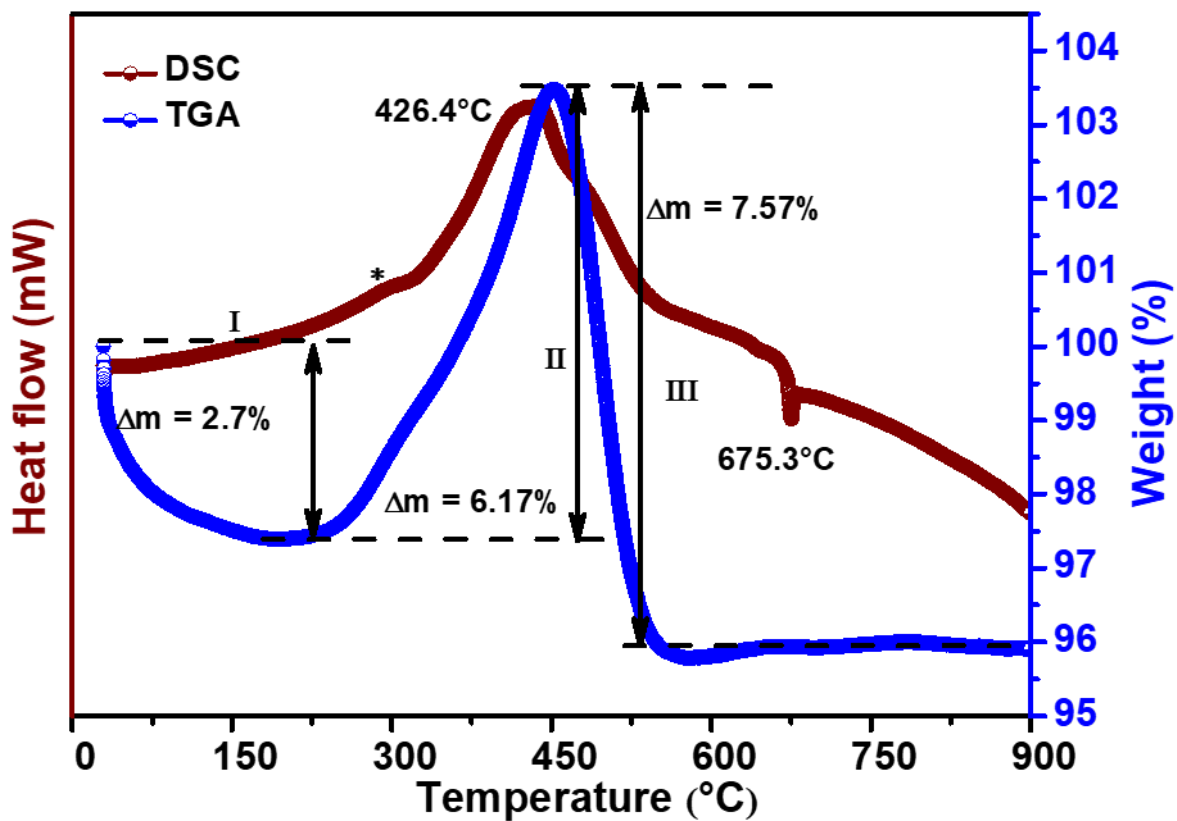


Figure 5. TGA-DSC plot for the VC@C material.

The thermal stability as well as oxidation resistance of the as synthesized VC@C was analysed by TGA-DSC plot in air from RT to 900 °C as shown in **Fig. 5**. TG curve is divided into three stages. In the first stage, small decrease in the mass (~3 %) during heating from RT to 230 °C corresponds to the loss of surface adsorbed species on the surface of the powder sample. The maximum weight gain in the second stage of TG curve (230 – 450 °C) indicates the oxidation process of VC with mass gain of 6.17 %. Such kind of conversion is considered to be a two-step process: release of carbon from the VC, followed by its oxidation. The temperatures corresponding to these two processes are indicated by a broad hump (marked as *) as well as broad exothermic peak in DSC curve at ~ 292 and 426 °C, respectively. If the as-prepared sample consists of pure VC, then its oxidation results more than 6% weight gain at 450 °C. Lesser increase in weight in our sample is mainly due to the existence of carbonaceous content in the synthesized sample. The rapid mass loss (7.57 %) in the third stage of TG curve from 450 – 550 °C corresponds to the oxidation of carbon into CO₂. Furthermore, TG curve seems to be stable after 600 °C, which indicates that all carbon and carbon coated VC (VC@C) have been oxidized completely leaving only stable V₂O₅. The appearance of endothermic peak in DSC curve at 675 °C corresponds to the melting of formed V₂O₅.⁴

The residual mass at these temperatures is used to calculate the free carbon content in the synthesized samples using the formula:⁵

$$\% \text{ free Carbon} = 100 \times \left[1 - 2 \times \frac{m_f}{m_i} \times \frac{MW_{VC}}{MW_{V_2O_5}} \right]$$

where, m_f : final mass, m_i : initial mass, MW_{VC} : molecular mass of VC, $MW_{V_2O_5}$: molar mass of V₂O₅. The free carbon content in VC@C comes out to be 36 %.

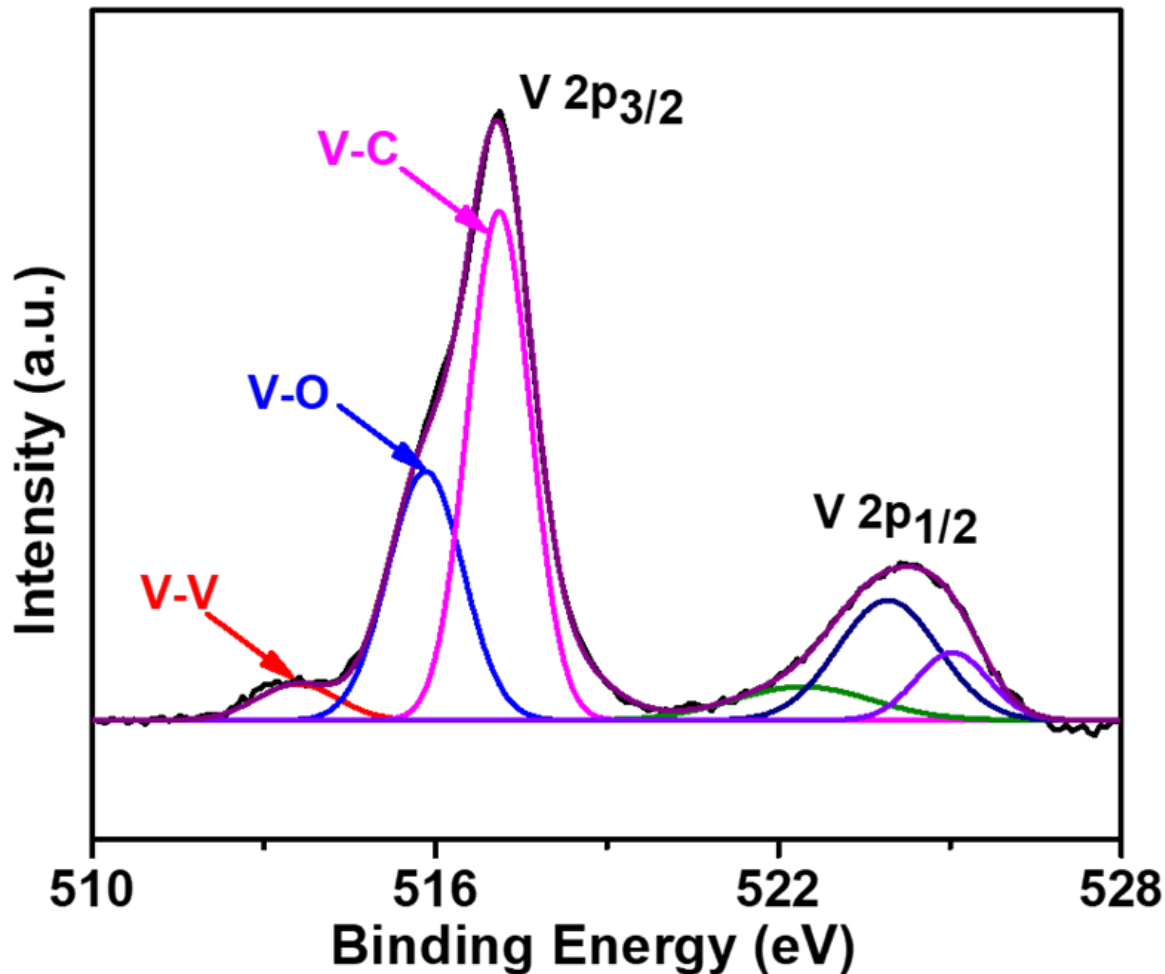


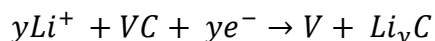
Figure 6. V2p XPS spectra of VC@C.

3.2. Material characterizations:

3.2.1. Electrochemical performance for LIB:

The electrochemical performance of VC@C nanocomposite was first investigated for LIBs. **Fig. 7a** shows the cyclic voltammetry (CV) measurements of VC@C obtained between a potential window of 0.01 and 3.0 V at an applied scan rate of 0.2 mV s⁻¹.

During the initial discharge cycle, the appearance of an irreversible anodic peak at around 1.5 V is more likely due to the decomposition of electrolyte on the electrode surface and formation of solid electrolyte interphase (SEI) layer on the surface of electrode which is found to be absent from in the consecutive cycles which indicates the formation of a stable SEI layer on the electrode-electrolyte interface.^{37,45} In the subsequent cycles, no signature of SEI was found which results in no irreversible capacity loss in the further cycles leading to a very stable anodic performance. VC@C clearly showed well-defined redox peaks at 2.52/2.69 V, 1.01/1.85 V and 0.57/1.19 V during lithiation and de-lithiation depicting the insertion of Li into the carbide system by reversible redox reactions of Li⁺ with VC which is in accordance with the existing transition metal carbide based electrode materials as:^{37,46}



Holding the same reversible features in the subsequent cycles, VC@C indicates the robustness of the 3D carbide material in terms of maintaining its structural integrity under reversible lithiation and de-lithiation process.

Charge-discharge data (**Fig. 7b**) can also be correlated with the cyclic voltammetry as the reversible redox peaks from the CV are also reflected in the voltage plateau region in the charge discharge data. The reversible Li storage ability of the material was found to be very impressive. VC@C showed remarkably stable anode performance with a very high initial discharge capacity of 1165 mAh g⁻¹ along with a reversible capacity of 640 mAh g⁻¹ after 100 cycles at an applied current density of 0.1 A g⁻¹ with ~100 % Coulombic efficiency (**Fig. 7c**). Gradual increase of capacity in VC@C following the initial reversible value is related to the potential driven steady activation of the favourable electrochemical sites for Li accommodation with long cycling or contact of more electrolyte into meso/micro pores of the active material.^{37,46} At a high current density of 1 A g⁻¹, a stable reversible capacity of 440 mAh g⁻¹ were realized after 1000 charge discharge cycles with 82 % capacity retention (**Fig. 7c**). This stable reversible Li ion storage capability can be attributed to its unique interconnected structure joined by carbon layers that provides well-ordered channels throughout the structure which can be clearly seen from the TEM image (**Fig. 1b**).

These channels facilitate the transport of the Li ions at a faster rate.⁴⁵ VC@C nanocomposite also shows an excellent rate performance (**Fig. 7d**) when exposed to variable current densities of 50 mA g⁻¹, 100 mA g⁻¹, 200 mA g⁻¹, 500 mA g⁻¹, 1 A g⁻¹, 2 A g⁻¹ and was further reduced back to 50 mA g⁻¹. The capacity drop was significantly less upon increasing the current density proving the carbide material to have the potential to deliver high power. The capacity was as high as 328 mAh g⁻¹ could be seen by increasing the current density by 40 times (2 A g⁻¹) than initial (0.05 A g⁻¹) in case of VC@C (**Fig. 7d**) which is approachable to the theoretical capacity of graphite at low current density.

Notably, the half-cell performance of the synthesized VC@C mentioned above is much higher than the values reported for most of the 2D/3D transition metal carbide-based anode materials along with their composites, as presented in the comparison table in **Table 2**.

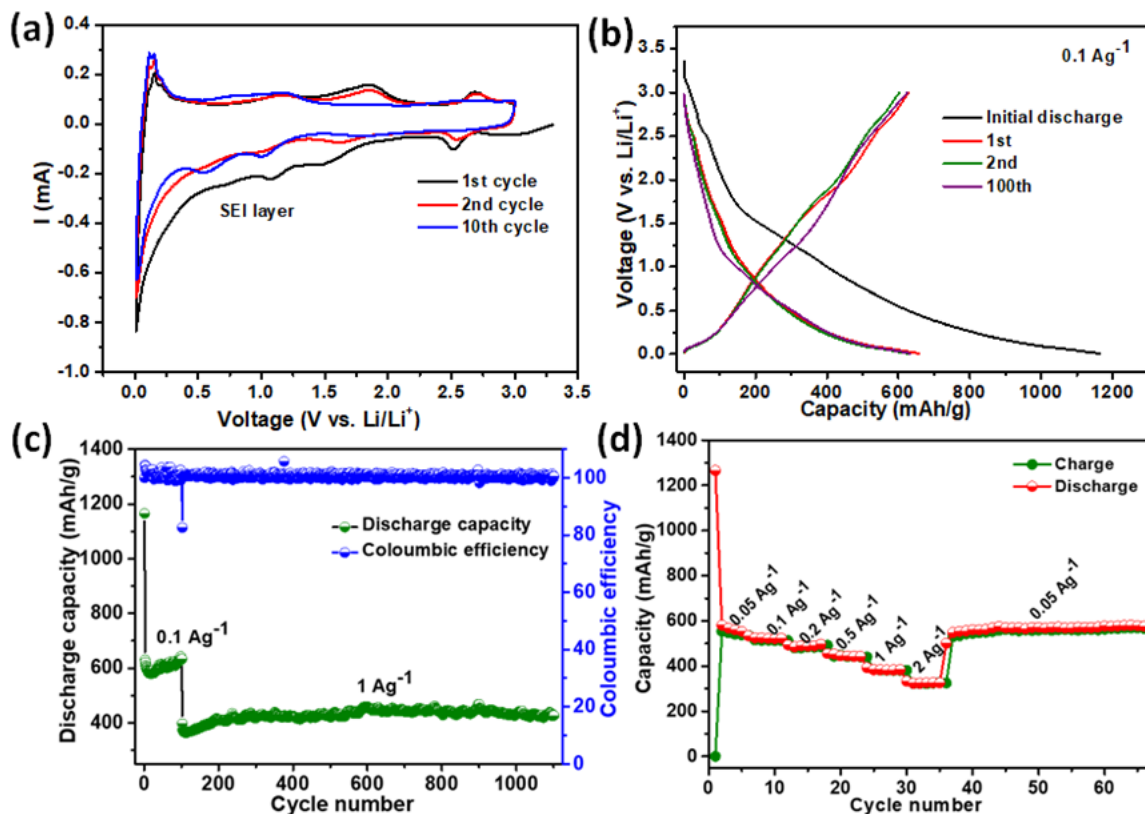


Figure 7. Li-ion electrochemistry data of VC@C material; (a) cyclic voltammetry data at a scan rate of 0.2 mV s^{-1} ; (b) Charge-discharge profile at a current density of 0.1 A g^{-1} ; (c) cyclic stability and coulombic efficiency data; (d) Rate performance data.

A full cell study was also performed to check the achievement of VC@C in terms of practicality. It offered a reversible charging capacity of 95 mAh g^{-1} at an applied current density of 0.1 A g^{-1} (based on the anode weight) after 100 charge discharge cycle with a Coulombic efficiency of 96 % (**Fig. 8a and b**) which in-turn gives a strong backing to the reversibility and robustness of the carbide material. Although for the first few cycles the Coulombic efficiency was low, it appeared to be more than 95 % in later cycles (**Fig. 8a**).

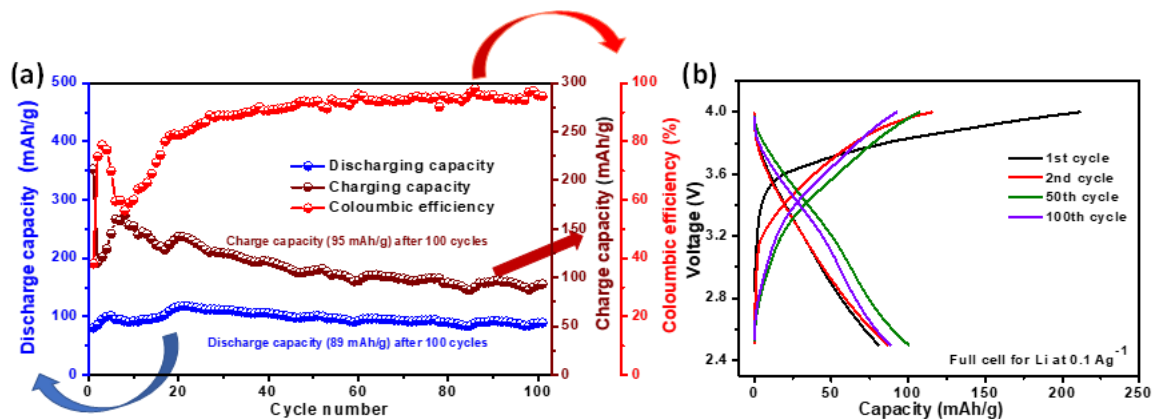


Figure 8. Li-ion full battery using VC@C as anode and LiCoO_2 ; (a) cyclic stability and coulombic efficiency data; (b) Charge-discharge profile at a current density of 0.1 A g^{-1} .

3.2.2. Electrochemical performance for SIB:

Na-ion electrochemistry of this carbide system was also studied. Na being larger (and heavier) in size than Li (1.02 Å vs. 0.76 Å), the reversible gravimetric capacity was obviously found to be less compared to Li. Absence of distinguishable sharp peaks and clear voltage plateau in CV (**Fig. 9a**) and charge discharge curve (**Fig. 9b**), respectively, depict that the nature of Na insertion into VC@C material differs to some extent from the Li insertion. However, this material also shows a clear promise in terms of cyclic stability and rate capability even for Na-ion (**Fig. 9c and d**). An initial discharge capacity 422 mAh g⁻¹ and a reversible capacity of 160 mAh g⁻¹ after 100 cycles at an applied current density of 100 mA g⁻¹ were observed in case of Na-ion.

The reduction peak in the first sodiation process at 1.43 V is attributed to the insertion of Na⁺ into VC, forming Na_xVC. The next reduction peak during sodiation (discharge) at 0.81 V is related to the further insertion of Na⁺ along with the formation of solid electrolyte interface (SEI) layer on the surface of electrode. In the oxidation curve of VC@C, a peak near 2.41 V can be ascribed to the de-sodiation process in VC@C system. In the subsequent cycles, a redox couple at ~0.55/0.71 V during discharge and charge cycles in VC@C can be ascribed to the electrochemical reduction/oxidation reactions (VC↔V) associated with Na⁺ insertion/deinsertion. Overlapping of peaks in subsequent cycles shows the excellent reversibility and robustness of the anode material to be used in SIBs. Absence of sharply defined peaks in VC@C as those observed in LIBs case is because of the large size, heavy mass and poor mobility of Na ion than Li.⁴⁵ A high discharge capacity of 111.2 mAh g⁻¹ is maintained even at a high current density of 1 A g⁻¹ after 500 cycles in VC@C composite with 89.1 % capacity retention (**Fig. 9c**). This can again be attributed to the robust structure of 3D carbide which can be observed from the post cycling characterizations as described in the later paragraph.

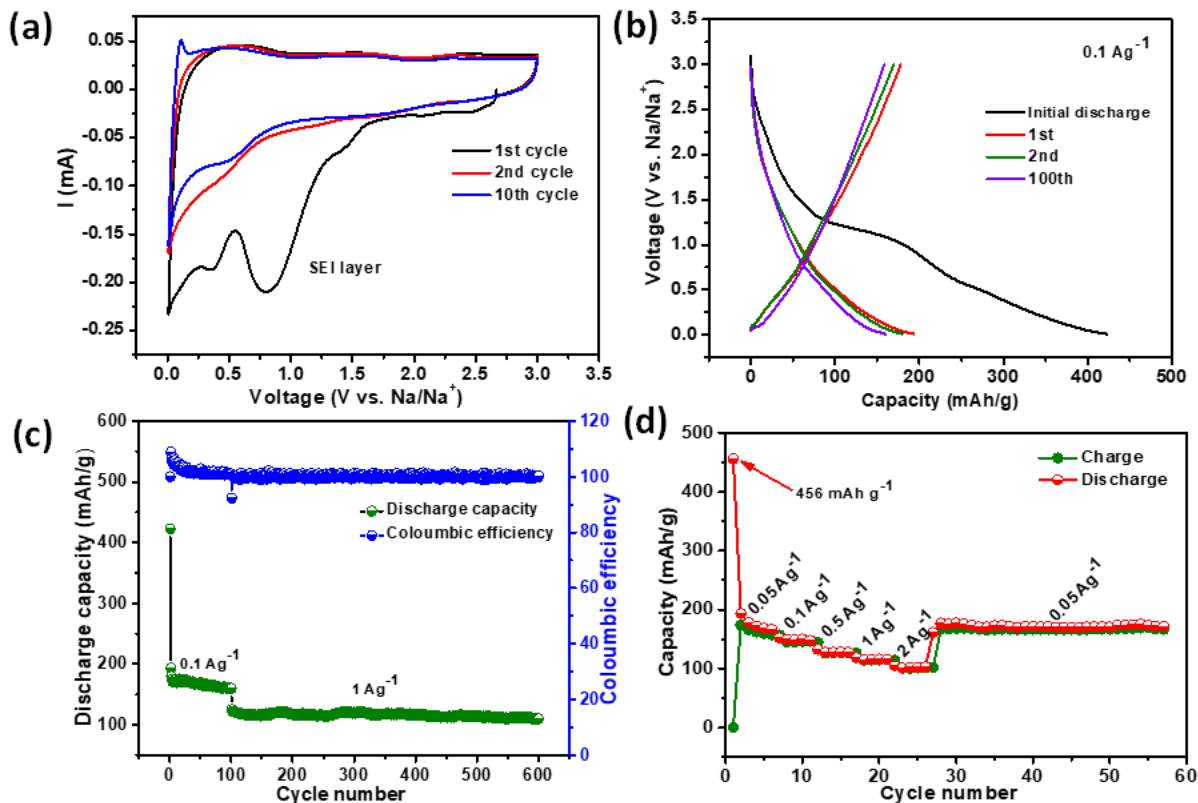


Figure 9. Na-ion electrochemistry data of VC@C material; (a) cyclic voltammetry data at a scan rate of 0.2 mV s^{-1} ; (b) Charge-discharge profile at a current density of 0.1 A g^{-1} ; (c) cyclic stability and coulombic efficiency data; (d) Rate performance data

3.2.3. Diffusion coefficient calculations:

Electrochemical impedance spectroscopy data (Fig. 10a and 10b) reveal a moderately low charge transfer resistance (R_{ct}) both in the case of Li and Na ions indicating good accessibility of electrolyte to the electrode surface as well as to the bulk of the material with reduced ion diffusion pathway.

To calculate the diffusion coefficients in case of Li and Na, plots of the real part of the impedance (Z_{real}) versus the reciprocal square root of the lower frequencies ($\omega^{-0.5}$) were examined (**Fig. 11a and 11b**).⁴⁷ The diffusion coefficient ($D^{\text{Li}+}/ D^{\text{Na}+}$) values for Li and Na turned out to be $3.4 \times 10^{-10} \text{ cm}^2 \text{ S}^{-1}$ and $1.6 \times 10^{-11} \text{ cm}^2 \text{ S}^{-1}$, respectively, which are significantly high among the reported literatures.⁴⁸⁻⁵⁵ This can be well correlated with the excellent rate performance of the VC@C material and hence this Li/Na storage in the VC@C material can be inferred as a diffusion-assisted insertion mechanism. Comparison tables (**table 2 and table 3**) show that the *in-situ* synthesized VC@C material stands tall among the reported carbide systems (2D/3D) for both the cases of Li and Na.

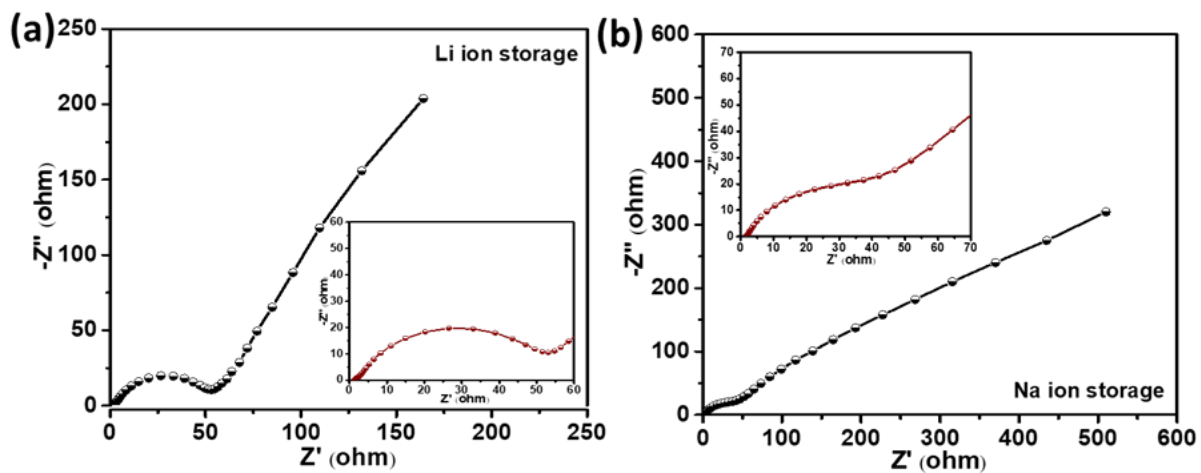


Figure 10. Impedance spectra for VC@C nanocomposite for (a) Li ion; (b) Na ion storage.

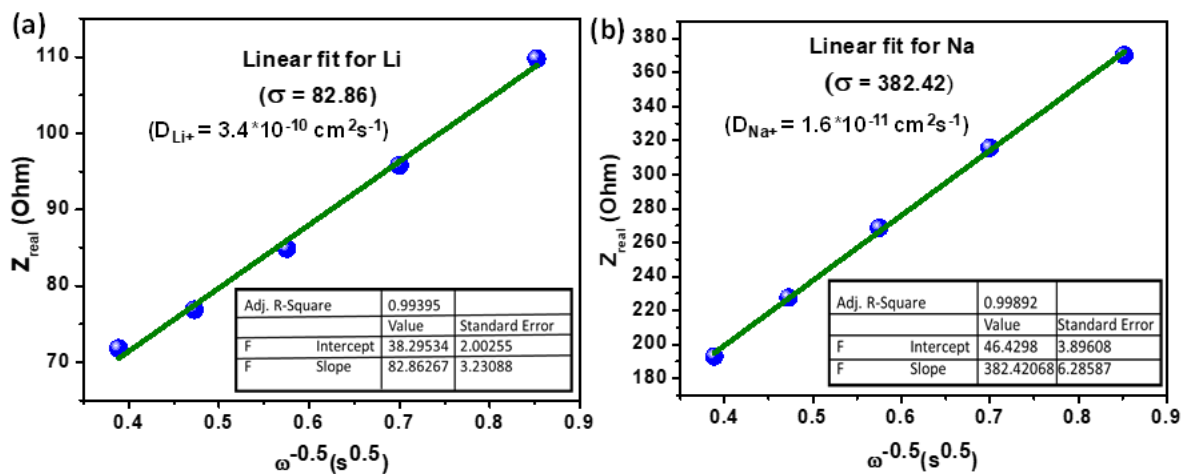


Figure 11. Z_{real} vs $\omega^{-0.5}$ plot for (a) Li-ion; (b) Na-ion.

Diffusion coefficients of Li and Na ion were calculated using the following equation:⁶

$$D = 0.5(RT/AF^2\sigma C)^2$$

Where, R is the universal gas constant ($8.314 \text{ J mol}^{-1} \text{ K}^{-1}$), T is the temperature (298.5 K), A is the area of the electrode surface (1.14 cm^2), F is the Faraday's constant ($9.65 \times 10^4 \text{ C mol}^{-1}$), C is the molar concentration of Li^+/Na^+ , and σ is the Warburg coefficient.

Warburg co-efficient, σ can be calculated using the following equation:

$$Z_{re} = R_e + R_{ct} + \sigma\omega^{-0.5}$$

where σ is the slope for the plot of Z_{re} vs. the reciprocal root square of the lower angular frequencies ($\omega^{-0.5}$).

Warburg co-efficient, σ for Li turns out to be 82.86 whereas, for Na it is 382.42. Corresponding calculated values of diffusion co-efficients are $3.4 \times 10^{-10} \text{ cm}^2 \text{ s}^{-1}$ and $1.6 \times 10^{-11} \text{ cm}^2 \text{ s}^{-1}$ for Li and Na respectively.

3.2.4. Electrochemical kinetics analysis:

Charge storage kinetics analysis was done from CV curves to understand the battery-capacitive mechanism in VC@C for Li^+/Na^+ ions. The CV curves of VC@C composite as LIB and SIB electrode at different scan rates from 0.1 to 2 mV s^{-1} are shown in inset of **Fig. 12a and 12d**, respectively. The capacitive contribution can be analysed according to the power law given below⁷:

$$i_{peak} = a v^b$$

$$\log(i_{peak}) = \log(a) + b \log(v)$$

where i_{peak} is the cathodic current, v is the scan rate, a and b is constant.

The ‘b’ value determines the diffusion controlled (~ 0.5) or capacitance controlled (~ 1.0) mechanism or the combination of both in Li/Na storage processes. By plotting $\log(i)$ versus $\log(v)$, the ‘b’ value comes out to be 0.66 for Li storage and 0.81 for Na storage as shown in **Fig. 12a and 12d**, respectively indicating the charge storage controlled by both diffusion-controlled and capacitive-controlled processes. However, it is more diffusion dominates in case of LIBs and capacitive dominance in SIBs.

Quantitatively, the capacity contribution to the total capacity can be determined by the following equation⁷:

$$i = k_1v + k_2v^{1/2} \quad (k_1 \text{ and } k_2 \text{ are constants})$$

where k_1v and $k_2v^{1/2}$ are the pseudo-capacitive and intercalation contributions.

The total capacitive contribution ratios of VC@C at different scan rates were calculated for both Li^+ and Na^+ and shown in **Fig. 12c and 12f**, respectively. The results reveal that the capacitive effect in the VC@C composite increases with increasing in the scan rate. Interestingly, charge storage in VC@C in case of LIBs is diffusion-controlled whereas, pseudo-capacitance charge-storage dominates the whole capacity in case of SIBs.

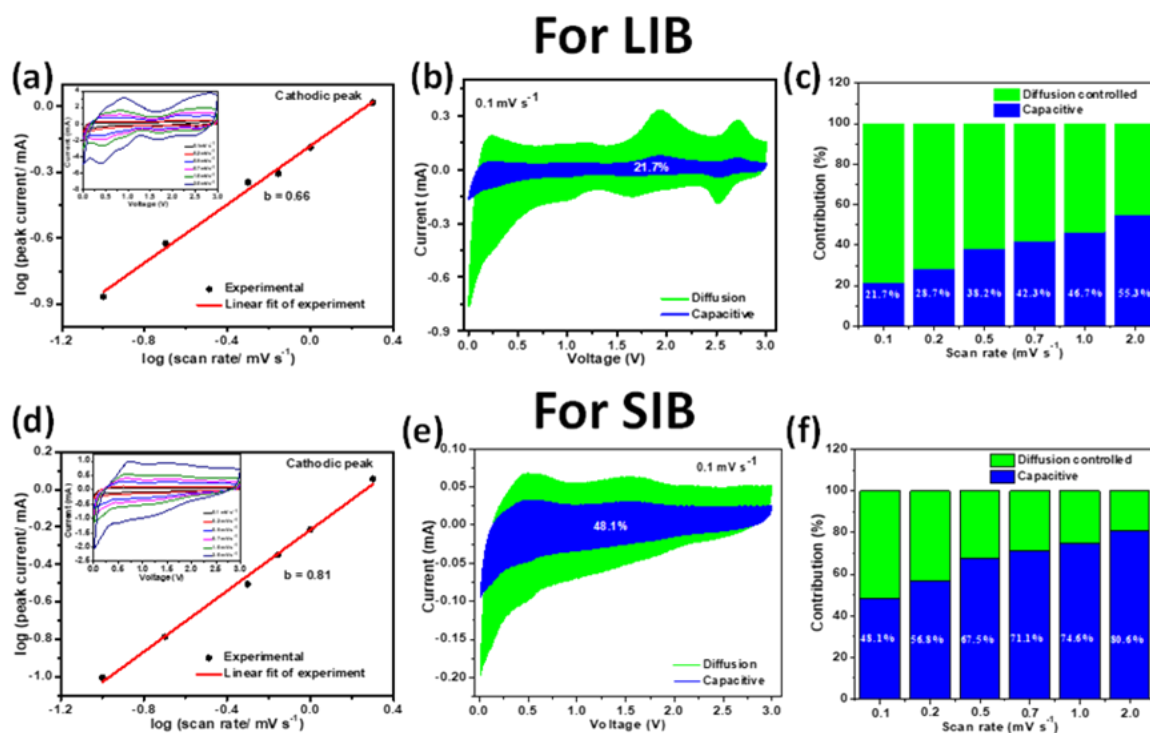


Figure 12. Diffusion and capacitive contribution calculation; (a) $\log(i)$ versus $\log(v)$ plot of the cathodic peak current for LIB (inset CV curves at various scan rates from 0.1 – 2 mV s^{-1}); (b) Capacitive (blue) and diffusion (green) contribution from CV curve at 0.1 mV s^{-1} for LIB; (c) Contribution ratio of the capacitive and diffusion-controlled charge storage versus scan rate for VC@C electrode for LIB. (d) $\log(i)$ versus $\log(v)$ plot of the cathodic peak current for SIB (inset CV curves at various scan rates from 0.1 – 2 mV s^{-1}); (e) Capacitive (blue) and diffusion (green) contribution from CV curve at 0.1 mV s^{-1} for SIB; (f) Contribution ratio of the capacitive and diffusion-controlled charge storage versus scan rate for VC@C electrode for SIB.

3.2.5. Post cycling characterizations:

Post cycling grazing incidence X-ray diffraction data (**Fig. 13a**) show that the cubic structure of the material remains intact upon lithiation and de-lithiation. However, a tensile strain in the cubic structure was noted as Li goes into the system as depicted by the observed shift towards lower 2θ in the post discharge XRD peaks. After charging, as the Li ions leaves the system it showed a tendency to go back to its original structure although there is some extent of irreversibility in it as is clear from the post-cycling XRD (**Fig. 13b**). But for Na ion, the trend differs from that of Li ion. For Na, a shift towards lower 2θ is observed in the XRD peaks while discharging, and after charging a further shift towards lower 2θ is observed (**Fig. 13d and 13e**). This can probably be attributed to the larger size of Na ion. As Na ion goes into the system, it renders an irreversible tensile strain to the system. The same trends were also observed in the Raman spectra (**Fig. 13c**) wherein as the G-band and 2D-band show a shift towards lower 2θ after discharge (lithiation) which is reversible as it comes back to original position after charging (delithiation) in the case of Li ion. Interestingly, no reversibility was observed during charging (desodiation) in the Raman peak of VC@C composite in case of Na ion (**Fig. 13f**).

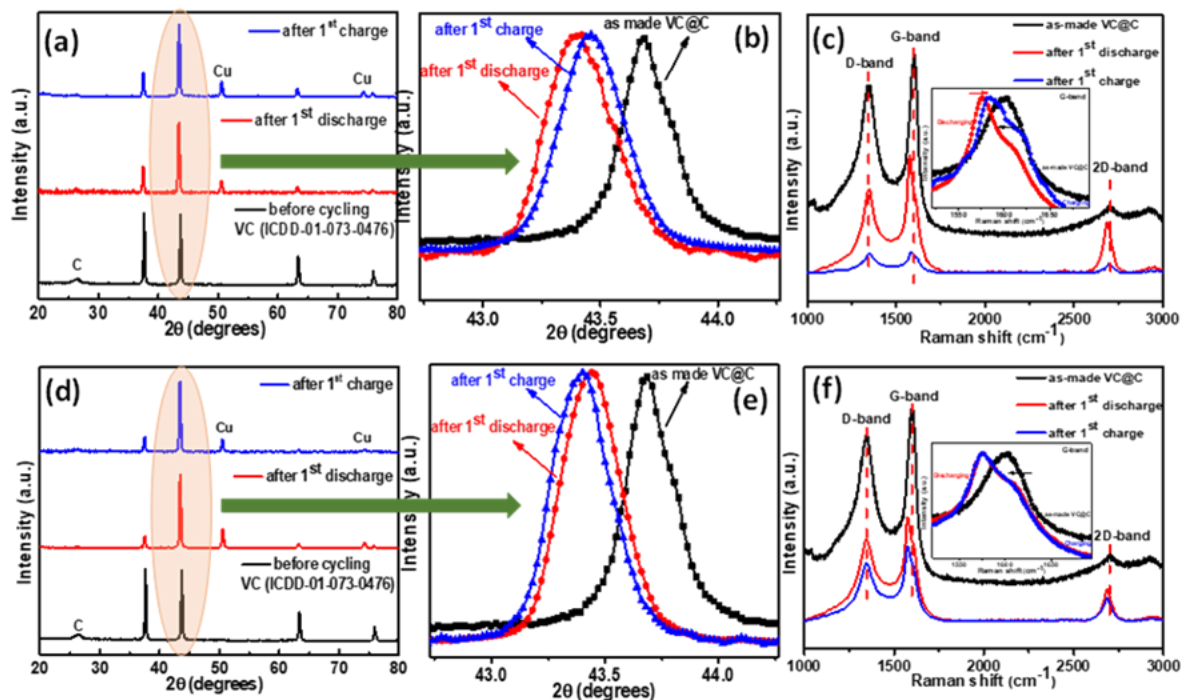


Figure 13. Post cycling characterizations in case of Li (a-c) and Na (d-f); (a and d) Post-cycling GIXRD in case of Li-ion and Na-ion half cells, respectively; (b and e) zoomed image of the GIXRD data to show the shift compare to the as-made material after discharging and charging in case Li-ion and Na-ion, respectively; (c and f) Post-cycling Raman spectra for Li and Na, respectively.

In order to further examine the lithium storage mechanism of VC@C, post-cycling Li1S XPS spectra and HRTEM were recorded after 1st lithiation to 0.01 V and de-lithiation to 3 V (**Fig. 14 and 15**). These data reveal that the structure is able to hold its integrity after lithiation and de-lithiation with no major change owing to the robustness of the 3D carbide system. Moreover, no much change in the morphology of VC@C was observed even after 1000 and 500 charge-discharge cycles for Li and Na ion, respectively (**Fig. 16**) which is also supported by elemental mapping where the uniform distribution of vanadium and carbon can be seen in **Fig. 17 and 18**.

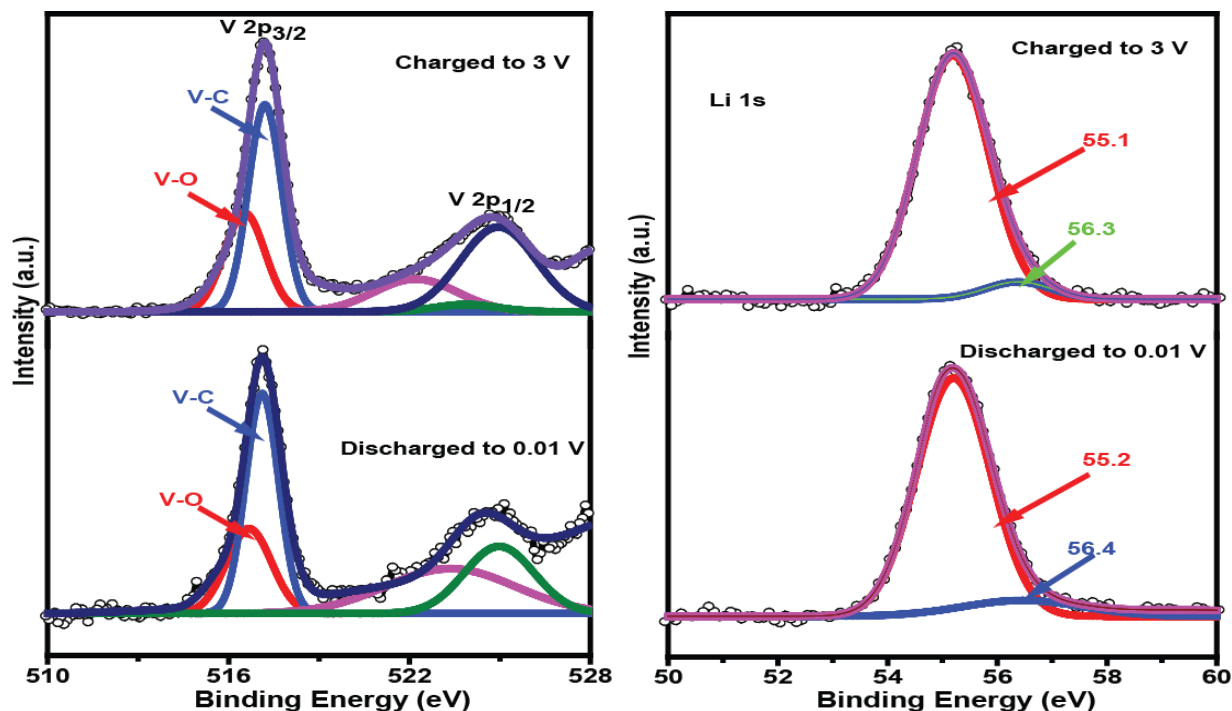


Figure 14. Post-cycling XPS spectra of (a) VC@C; (b) Lithium, after 1st discharge and 1st charge.

Post-cycling XPS spectra of VC@C after 1st discharge to 0.01 and 1st charge to 3 V are shown in **Fig. 14(a)**. In both cases, composition and structure of VC@C do not change. Moreover, from Li 1s XPS spectra for lithiated and delithiated states, absence of any extra peak implies almost no change in structure during cycling (**Fig. 14(b)**). This is the testimony to the robustness of the VC@C system in terms of holding its structure upon lithiation and de-lithiation.

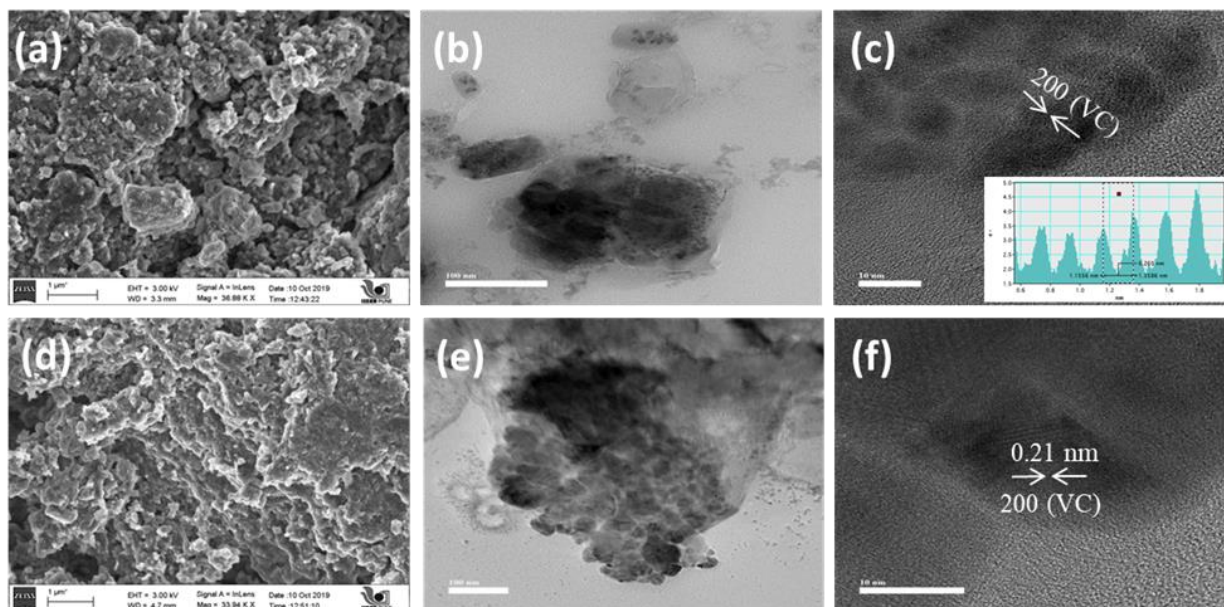


Figure 15. FESEM and TEM data of VC@C electrode (a-c) after 1st discharge (lithiation); (d-f) 1st charge (delithiation), respectively.

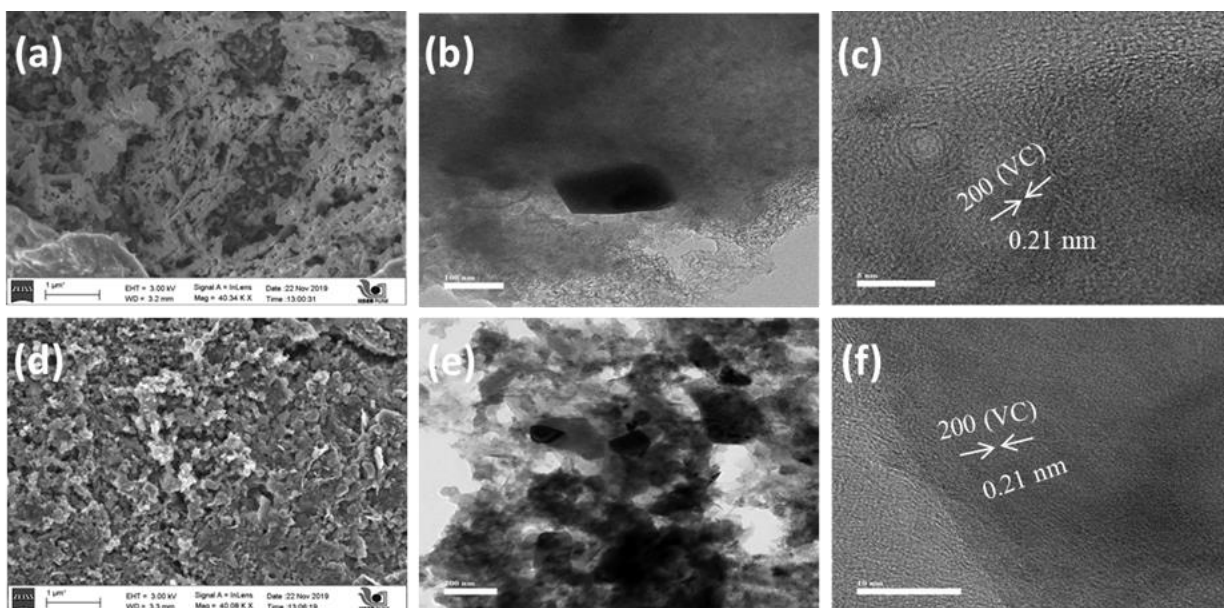


Figure 16. FESEM and TEM data of VC@C electrode (a-c) after 1st discharge (lithiation); (d-f) 1st charge (delithiation), respectively.

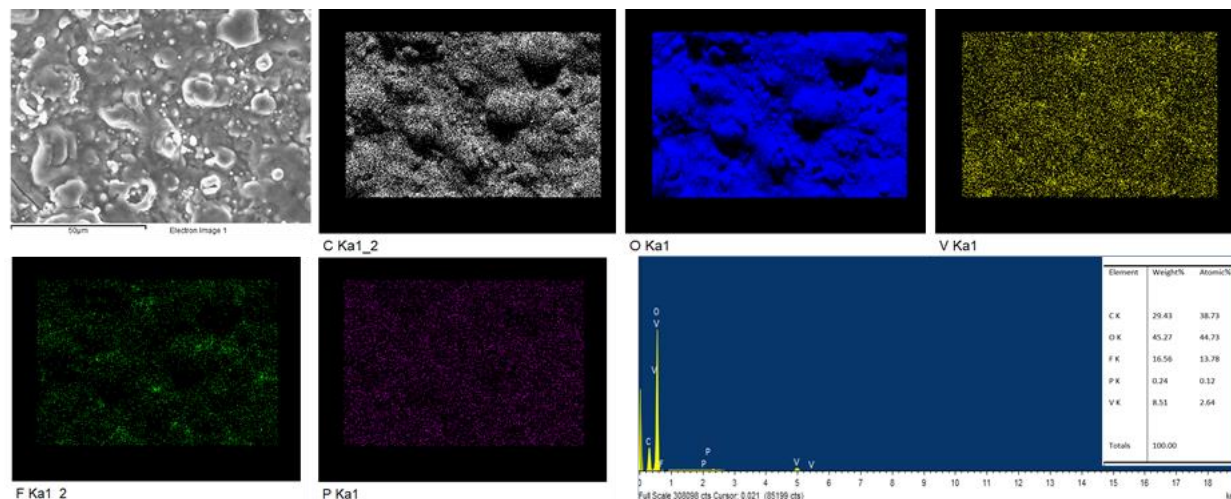


Figure 17. EDX spectra and corresponding elemental mapping of VC@C electrode after 1000 charge-discharge cycles in case of LIBs.

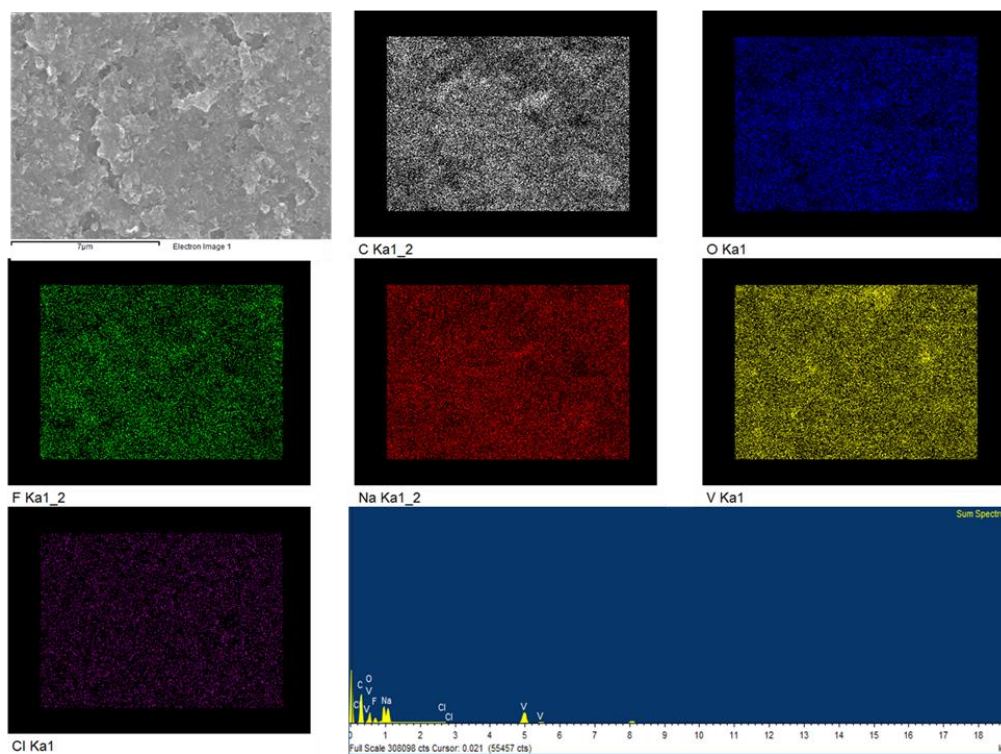


Figure 18. EDX spectra and corresponding elemental mapping of VC@C electrode after 500 charge-discharge cycles in case of SIBs.

3.2.6. Williamson-Hall analysis:

Although there are theoretical studies based on the stress generation and deformation during migration of Li/Na ions in some systems, studies on its correlation with experimental evidence are rare.⁵⁶⁻⁶¹ Herein, we study the role of strain, stress, and deformation caused by the introduction of the guest ion (Li/Na) in the system by Williamson-Hall analysis (**Fig. 19**) using Uniform Deformation Model (UDM), uniform stress deformation model (USDm), and uniform deformation energy-density model (UDEDm). The outcome of the analysis is tabled below (**Table 1**).

		Pristine VC@C	LIBs		SIBs	
			Discharging	Charging	Discharging	Charging
UDM	$\epsilon \times 10^{-3}$	1.18	4.12	1.31	1.45	1.73
USDm	$\epsilon \times 10^{-3}$	1.13	4.11	1.18	1.38	1.56
	σ (MPa)	556	2030	583	681	772
UDEDm	$\epsilon \times 10^{-3}$	1.17	4.14	1.26	1.43	1.68
	σ (MPa)	575	2044	621	704	830
	$u \times 10^3$ (kJ/m ³)	0.336	4.24	0.392	0.504	0.698

Table 1. Geometric parameters of VC@C obtained from Williamson-Hall analysis.

✚ **Detailed Williamson-Hall calculations:**

✓ **Migration effect of Li/Na ions on VC crystal structure (From Williamson-Hall analysis):**

To reveal the structural integrity of the as-made electrode during Li/Na ions migration, post cycling measurements were done. **Fig. 13** shows the X-ray diffraction of the anode before cycling and after 1st discharge and charge cycle for LIBs and SIBs. The observed shift towards lower 2 theta in the peak position in XRD profile is because of the distortion in the lattice with the migration of Li/Na ions. The inherent defect in terms of distortion results to induce strain in the crystal structure of VC@C, which has been evaluated through the analysis of line broadening of X-ray profile shown in **Fig. 13(a and d)**. Although there are theoretical studies based on the stress generation and deformation during migration of Li/Na ions, studies on its correlation with experimental evidence is rare.⁶²⁻⁶⁵

In this analysis, we highlight the effect of insertion/deinsertion of Li/Na ions on the generation of (i) strain, (ii) stress and (iii) deformation energy. Among the available methods to estimate the lattice strain, Williamson-Hall (W-H) analysis is a simplified method where strain-induced broadening are deconvoluted by considering the peak width as a function of 2θ .⁶⁶ In order to determine the induced strain due to the lattice deformation as a result of Li/Na species migration, W-H analysis has been modified into Uniform Deformation Model (UDM), uniform stress deformation model (USDM) and uniform deformation energy-density model (UDEDM).⁶⁷ However, by assuming the particle size and strain contributions to X-ray line broadening independent of each other, the observed total integral breadth of Bragg peak is a result of additive component of size (β_D) and strain (β_s) broadening viz:⁶⁸

$$\beta_{hkl} = \beta_D + \beta_s = (k\lambda/D\cos\theta_{hkl}) + (4\epsilon_{hkl}\tan\theta_{hkl}) \quad (1)$$

$$\beta_{hkl}\cos\theta_{hkl} = (k\lambda/D) + (4\epsilon_{hkl}\sin\theta_{hkl}) \quad (2)$$

Here k is the shape factor, λ is the X-ray wavelength, θ_{hkl} is the Bragg angle, β_{hkl} is peak width at half-maximum intensity, D is the effective crystallite size and ϵ_{hkl} is induced microstrain due to crystal imperfection and distortion. Equation (2) represents the UDM, where the strain was assumed to be uniform in all crystallographic directions, thus considering the isotropic nature of the crystal.⁶⁹ The Williamson-Hall plot for UDM has been plotted by using term ($\beta_{hkl} \cos\theta_{hkl}$) with respect to ($4 \sin\theta_{hkl}$) for as-made VC@C as well as Li/Na migrated samples after charging

and discharging stage and have been shown in **Fig. 19**. The obtained positive value of micro strain ‘ ϵ ’ through the slope of plot is mentioned in **Table 1** which designates the tensile strain in the system.

The value of strain through UDM has been obtained by considering the induced strain to be uniform in all directions of isotropic crystal during synthesis of material as well migration of Li/Na species after charging and discharging. But in most cases, the assumption of the homogeneity and isotropy is not fulfilled. So, by assuming the cause of lattice strain to be deformation stress and density of deformation energy ‘ u ’ (energy per unit volume), the USDM and UDEDM have been taken into consideration.⁶⁸ Hence, with this approach the Williamson-Hall equation for USDM and USEDMD has been converted into the form of:

$$\beta_{hkl}\cos\theta_{hkl} = (k\lambda/D) + (4\sigma\sin\theta_{hkl}/E_{hkl}) \quad (3)$$

$$\beta_{hkl}\cos\theta_{hkl} = (k\lambda/D) + (4\sin\theta_{hkl}(2u/E_{hkl})^{1/2}) \quad (4)$$

E_{hkl} is the Young’s modulus in the direction perpendicular to the set of planes (hkl). The value of uniform stress σ and energy density ‘ u ’ can be calculated from the slope of plot between $\beta_{hkl}\cos\theta_{hkl}$ as a function of $4\sin\theta_{hkl}/E_{hkl}$ and $\beta_{hkl}\cos\theta_{hkl}$ as a function of $4\sin\theta_{hkl}(2u/E_{hkl})^{1/2}$, respectively. Hence, the value of anisotropic microstrain ϵ_{hkl} through these two models can be calculated by knowing E_{hkl} . For a sample with cubic crystals (VC), Young’s modulus E_{hkl} in the direction perpendicular to the set of planes (hkl) is in the form of $E_{hkl}^{-1} = s_{11} - (2s_{11} - 2s_{12} - s_{44})[(k^2l^2 + l^2h^2 + h^2k^2)/(h^2 + k^2 + l^2)^2]$.⁷⁰ Here s_{11} , s_{12} and s_{44} are the elastic compliances. The value of elastic compliances ($s_{11}=1.8\times 10^{-3}$ GPa⁻¹, $s_{12}=0.36\times 10^{-3}$ GPa⁻¹, $s_{44}= 5.6\times 10^{-3}$ GPa⁻¹) used in this equation for VC has been calculated from elastic constant by using relations between them.^{71,72} The plot for USDM and USEDMD for as-synthesized VC and Li/Na migrated samples after discharging and charging have been shown in **Fig. 19**. The data obtained from these figures are summarized in **Table 1**.

The observed values clearly attribute that during lithiation, high value of induced deformation energy and deformation stress results to highly strained system. Interestingly, the release of overall lithiation induced strain (LIS) during delithiation strongly supports that extraction of Li causes unit cell breathing phenomena takes place in LIBs system.⁷³ It shows excellent reversibility of the electrode material which has been revealed through the post-cycling XRD of (200) plane of VC in **Fig. 13b**. This has also been confirmed by observing the notable difference

in stress-strain values during delithiation (**Table 1**). Generation of tensile stress during lithiation have been reported by many authors.⁷³⁻⁷⁵ So, VC@C has been proved to be a mechanical robust material for LIBs which can release the stress generated during discharging without much change in the structure.

Conversely, the increase of stress-strain values during desodiation results in high deformation in the lattice which is clear from the data shown in **Table 1**. Such kind of irreversible behavior has also been observed from the post-cycling XRD of (200) plane of VC for SIBs shown in **Fig. 13e**. This might be because, Na being bulkier in size compare to Li, it suppressed unit cell breathing in the lattice resulting in more deformation and eventually, less capacity.

The observed shift in the G-band of Raman spectroscopy can be related to the internal stress inside the lattice.⁷⁶ Observed blue-shift of the Raman band during lithiation suggest the tensile stress in the material whereas upshift of G-band during delithiation as compared to lithiation shows relaxation behavior of the crystal in LIBs which is in excellent agreement with post-cycling XRD results (**Fig. 13c**).²³ As expected in case of SIBs, no change in the G-band of raman spectroscopy during sodiation/desodiation shows the irreversibility in case of Na during desodiation which agrees well with our post-cycling XRD results for SIBs (**Fig. 13f**).

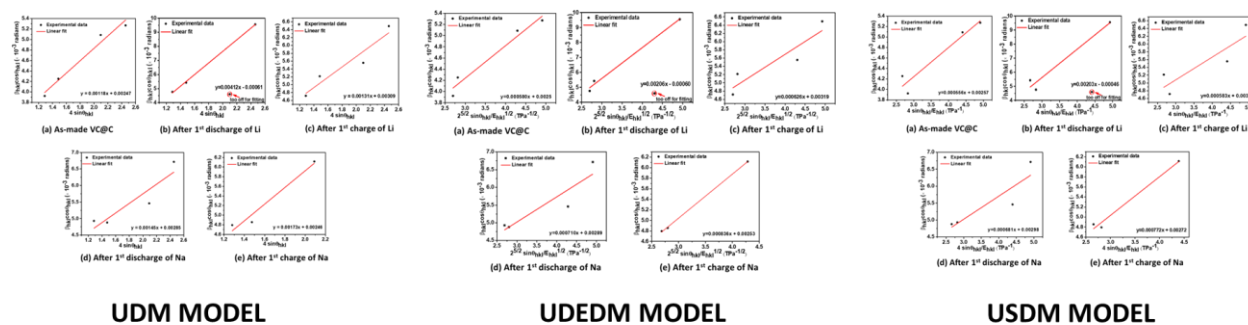


Figure 19. Modified form of W-H analysis assuming UDM, UEDM and USDM models

Material Composition	Current density (mA g⁻¹) or C-rate	Initial Discharge capacity (mAh g⁻¹)	First Reversible Capacity (mAh g⁻¹)	Reversible capacity after number of cycles (mAh g⁻¹)	Synthesis Route
V ₂ C ^[77]	370	467	291	243 at 0.5 A g ⁻¹ after 500 cycles	High temperature heating at 1500 °C, multi-step route
V ₂ CT _x ^[78]	1C	380	210	260 at 1 C after 150 cycles	Multi-step route followed by sintering at 1500 °C under Ar
Nb ₂ CT _x ^[79]	1C	422	250	170 at 1 C after 150 cycles	Multi-step route followed by high temperature heating at 1600 °C under Ar
Ti ₃ C ₂ T _x ^[80]	0.1 C	410	250	147.4 at 1 C after 100 cycles	Tw-step route followed by calcination upto 1000 °C
MoS ₂ @Ti ₃ C ₂ ^[81]	50	386.4	245	131.6 at 1 A g ⁻¹ after 200 cycles	Multi-step route followed by calcination at 450 °C under Ar-H ₂
MoC _{0.654} @CNS ^[82]	200	1667	1100	815 at 0.5 A g ⁻¹ after 680 cycles	Multi-step route followed by heat treatment at 900-1000 °C under Ar

Mo ₂ C/G R ^[83]	100	1718	1000	813 at 0.1 A g ⁻¹ after 100 cycles	Two-step route followed by annealing at 800 °C under Ar
Fe@Fe ₃ C/C ^[84]	50	941.1	505	382.2 at 0.2 A g ⁻¹ after 30 cycles	Multi-step route followed by multiple heatings at high temperatures
Fe ₃ C- C ^[85]	50	300	230	250 at 0.05 A g ⁻¹ after 20 cycles	Multi-step route followed by high temperature sintering at 750 °C
Mo ₂ C- C ^[86]	100	1054.3	940	777.7 at 1 A g ⁻¹ after 1000 cycles	Two-step route followed by calcination at 850 °C under N ₂
MoC/gra phitic carbon ^[87]	50	1176.9	910.9	742 at 0.2 A g ⁻¹ after 50 cycles	Calcination at 700 °C under N ₂
Mo ₂ C- NCNFs ^[89]	100	1070.9	790	411.9 at 2 A g ⁻¹ after 50 cycles	Multi-step route followed by heat treatment at 800 °C under N ₂
Mo ₂ C-C nanosph eres ^[90]	100	951.2	770	308.7 at 2 A g ⁻¹ after 50 cycles	Multi-step route followed by calcination at 550 °C under H ₂ -Ar
MoO ₂ /M o ₂ C ^[91]	200	480	460	510 at 1 A g ⁻¹ after 140 cycles	Multi-step reaction route subsequently treated at 820 °C under N ₂
TiC/NiO ^[92]	50	918.1	600	507.5 at 0.2A g ⁻¹ after 60 cycles	Multi-step reaction route followed by annealing at 350 °C

					under N ₂
V ₈ C ₇ /R GO ^[93]	100	1280.1	1065	1059.8 at 0.1 A g ⁻¹ after 120 cycles	Multi-step route followed by heat- treatment at 1000 °C under H ₂ -Ar flow
Ti ₃ C ₂ T _x / Fe ₂ O ₃ ^[94]	1 C	737	490	460 at 1C after 180 cycles	Multi-step reaction route calcined at 400 °C under Ar followed by ball milling
Ti ₃ C ₂ /C NF ^[95]	1 C	848	407	320 at 1C after 295 cycles	Multi-step reaction route followed by heat-treatment at 600 °C under Ar- H ₂ flow
Nano- Sn/C ^[96]	200	1029	710	700 at 0.2 A g ⁻¹ after 130 cycles	aerosol spray pyrolysis, followed by heat treatment at 900 °C
SiC nanofibe rs ^[97]	100	309.3	210	504.1 at 0.3 A g ⁻¹ after 500 cycles	Carbothermal reduction at 1400 °C in Ar
VC@C (Present work)	100	1165.4	663.9	440 at 1 A g⁻¹ after 1000 cycles	Single-step mechano-chemical synthesis

Table 2. Electrochemical performance of Transition metal Carbides/Composites as LIB anode materials.

Material Composition	Current density (mA g⁻¹) or C-rate	Initial Discharge capacity (mAh g⁻¹)	First Reversible Capacity (mAh g⁻¹)	Reversible capacity at Large current density after number of cycles	Synthesis Route
V ₂ CT _x ^[98]	2.5 C	470	260	310 at 2.5 C after 1000 cycles	High-temperature sintering from 850-1500 °C under Ar followed by etching
Mo ₂ CT _x ^[98]		400	210	290 at 2.5 C after 1000 cycles	
Ti ₃ C ₂ T _x ^[98]		390	210	295 at 2.5 C after 1000 cycles	
V ₂ CT _x ^[98]	10	220	120	50 at 1 A g ⁻¹ after 5 cycles	High-temperature sintering at 1500 °C under Ar followed by etching
p-Ti ₃ C ₂ T _x ^[99]	100	641	210	189 at 1 A g ⁻¹ after 1000 cycles	High-temperature sintering at 1350 °C under Ar

					followed by etching
MoC/graphitic carbon ^[87]	50	551.3	340	250 at 0.05 A g ⁻¹ after 50 cycles	Calcination at 700 °C under N ₂
VC@C (Present work)	100	422.4	195.3	111.2 at 1 A g⁻¹ after 600 cycles	Single-step mechano-chemical synthesis

Table 3. Electrochemical performance of Transition metal Carbides/Composites as SIB anode materials.

Thus, on the whole, the unique material properties and architecture of VC@C effectively withstand the volume change, restrict the aggregation of VC, and prevent the structure from collapsing during multiple cycling. Carbon matrix not only accommodates the volume change of VC during electrochemical lithiation and delithiation but also prevents continual cracking and re-formation of SEI film resulting in longer battery life.

4. Conclusions:

In summary, we have prepared *in-situ* carbon encapsulated VC (VC@C) nanocomposite with three-dimensional core-shell structure by a single-step room-temperature ball milling procedure and investigated its electrochemical performance of this very less explored carbide material as anode for LIBs and SIBs. The as-prepared VC@C shows a clear promise for practical use in terms of electrochemical performance with an impressive capacity of 640 mAh g⁻¹ after 100 discharge/charge cycles at 0.1 A g⁻¹ for LIBs with very high reversibility. The same material also proves to be a good host for Na ions with very good rate capability and cyclic stability. Post cyclic GIXRD data prove that the reversibility and rate capability can be attributed to the robust nature of 3D carbide since the cubic structure of the material remains intact upon charging and discharging. Indeed, VC appears to be one of the most stable battery materials in the current family of anode materials. The room temperature mechano-chemical ball-milling synthesis strategy reported in this present work is facile and cost-effective and therefore, can be expected to be a promising development for the synthesis of other transition metal carbides with different morphologies for use as a potential material in energy storage devices.

References:

- [1]. Zheng, Y., Zhou, T., Zhao, X., Pang, W. K., Gao, H., Li, S., Zhou, Z., Liu, H., Guo, Z. *Adv. Mater.* **2017**, 29, 1700396.
- [2]. Ortiz-Vitoriano, N., Drewett, N. E., Gonzalo, E., Rojo, T. *Energy Environ. Sci.* **2017**, 10, 1051-1074.
- [3]. Li, L., Zheng, Y., Zhang, S., Yang, J., Shao, Z., Guo, Z. **2018**, 11, 2310-2340.
- [4]. Lv, X., Wei, W., Huang, B., Dai, Y. *J. Mater. Chem. A* **2019**, 7, 2165-2171.
- [5]. Jiang, Y., Yue, J. -L., Guo, Q., Xia, Q., Zhou, C., Feng, T., Xu, J., Xia, H. *Small* **2018**, 14, 1704296.
- [6]. Wahid, M., Gawli, Y., Puthusseri, D., Kumar, A., Shelke, M. V., Ogale, S. *ACS Omega* **2017**, 2, 3601-3609.
- [7]. Cao, K., Jiao, L., Liu, Y., Liu, H., Wang, Y., Yuan, H. *Adv. Funct. Mater.* **2015**, 25, 1082-1089.
- [8]. Tan, G., Wu, F., Yuan, Y., Chen, R., Zhao, T., Yao, Y., Qian, J., Liu, J., Ye, Y., Shahbazian-Yassar, R., Lu, J., Amine, K. *Nat. Commun.* **2016**, 7, 11774.
- [9]. Stephenson, T., Li, Z., Olsenab, B., Mitlin, D. *Energy Environ. Sci.* **2014**, 7, 209-231.
- [10]. Gao, M. -R., Xu, Y. -F., Jiang, J., Yu, S. -H. *Chem. Soc. Rev.* **2013**, 42, 2986-3017.
- [11]. Roy, K., Wahid, M., Puthusseri, D., Patrike, A., Muduli, S., Vaidhyanathan, R., Ogale, S. *Sustainable Energy Fuels* **2019**, 3, 245-250.
- [12]. Chan, C. K., Zhang, X. F., Cui, Y. High Capacity Li Ion Battery Anodes Using Ge Nanowires. *Nano Lett.* **2008**, 8, 307-309.
- [13]. Zhang, Q., Gao, Q., Qian, W., Zhang, H., Tan, Y., Tian, W., Li, Z., Xiao, H. *J. Mater. Chem. A* **2017**, 5, 19136-19142.
- [14]. Ramireddy, T., Xing, T., Rahman, M. M., Chen, Y., Dutercq, Q., Gunzelmann, D., Glushenkov, A. M. *J. Mater. Chem. A* **2015**, 3, 5572-5584.
- [15]. Puthusseri, D., Wahid, M., Ogale, S. *ACS Omega* **2018**, 3, 4591-4601.
- [16]. Wang, M., Ma, Y., Jiang, J., Huang, Y., Li, X., Zheng, J., Qin, C., Yan, P., Cao, G. *ChemElectroChem* **2019**, 6, 1139-1148.
- [17]. Lu, B., Liu, J., Hu, R., Wang, H., Liu, J., Zhu, M. *J. Mater. Chem. A* **2017**, 5, 8555-8565.
- [18]. Zhang, W. -M., Wu, X. -L., Hu, J. -S., Guo, Y. -G., Wan, L. -J. *Adv. Funct. Mater.* **2008**, 18, 3941-3946.

- [19]. Needham, S. A., Wang, G. X., Konstantinov, K., Tournayre, Y., Lao, Z., Liu, H. K. *Electrochem. Solid-State Lett.* **2006**, 9, A315-A319.
- [20]. Zhao, W., Ma, X., Wang, G., Long, X., Li, Y., Zhang, W., Zhang, P. *Appl. Surf. Sci.* **2018**, 445, 167-174.
- [21]. Jiang, J., Wang, W., Wang, C., Zhang, L., Tang, K., Zuo, J., Yang, Q. *Electrochim. Acta* **2015**, 170, 140-145.
- [22]. Sharma, N., Shaju, K. M., Subba Rao, G. V., Chowdari, B. V. R., Dong, Z. L., White, T. *J. Chem. Mater.* **2004**, 16, 504-512.
- [23]. Zhou, G., Wang, D. -W., Li, F., Zhang, L., Li, N., Wu, Z. -S., Wen, L., Lu, G. Q. (Max), Cheng, H. -M. *Chem. Mater.* **2010**, 22, 5306-5313.
- [24]. Liu, Y., Liu, J., Hou, M., Fan, L., Wangand, Y., Xia, Y. *J. Mater. Chem. A* **2017**, 5, 10902-10908.
- [25]. Arnaiz, M., Botas, C., Carriazo, D., Mysyk, R., Mijangos, F., Rojo, T., Ajuria, J., Goikole, E. *Electrochim. Acta* **2018**, 284, 542-550.
- [26]. Jin, R., Jiang, Y., Li, G., Meng, Y. *Electrochim. Acta* **2017**, 257, 20-30.
- [27]. Zhong, Y., Xia, X., Shi, F., Zhan, J., Tu, J., Fan, H. *J. Adv. Sci.* **2016**, 3, 1500286.
- [28]. Naguib, M., Halim, J., Lu, J., Cook, K. M., Hultman, L., Gogotsi, Y., Barsoum, M. W. *J. Am. Chem. Soc.* **2013**, 135, 15966-15969.
- [29]. Xiao, Y., Sun, P., Cao, M. *ACS Nano* **2014**, 8, 7846-7857.
- [30]. Naguib, M., Mochalin, V. N., Barsoum, M. W., Gogotsi, Y. **2014**, 26, 992-1005.
- [31]. Kim, S. J., Naguib, M., Zhao, M., Zhang, C., Jung, H. T., Barsoum, M. W., Gogotsi, Y. *Electrochim. Acta* **2015**, 163, 246-251.
- [32]. Naguib, M., Come, J., Dyatkin, B., Presser, V., Taberna, P. -L., Simon, P., Barsoum, M. W., Gogotsi, Y. *MXene Electrochem. Commun.* **2012**, 16, 61-64.
- [33]. Kurra, N., Alhabeab, M., Maleski, K., Wang, C. -H., Alshareef, H. N., Gogotsi, Y. *ACS Energy Lett.* **2018**, 3, 2094-2100.
- [34]. Wang, B., Wang, G., Wang, H. *J. Mater. Chem. A* **2015**, 3, 17403-17411.
- [35]. Su, L., Zhou, Z., Shen, P. *Electrochim. Acta* **2013**, 87, 180-185.
- [36]. Qiu, J., Yang, Z., Li, Q., Li, Y., Wu, X., Qi, C., Qiao, Q. *J. Mater. Chem. A* **2016**, 4, 13296-13306.
- [37]. Yang, J., Li, L., Zhang, Y., Zhang, Y., Sun, C., Tan, H., Huang, W., Yan, Q., Dong, X. *ChemistrySelect* **2016**, 1, 2682-2686.

- [38]. Balaz, P., Achimovicova, M., Balaz, M., Billik, P., Cherkezova-Zheleva, Z., Criado, J. M., Delogu, F., Dutkova, E., Gaffet, E., Gotor, F. J., Kumar, R., Mitov, I., Rojac, T., Senna, M., Streletskii, A., Wieczorek-Ciurowa, K. *Chem. Soc. Rev.* **2013**, 42, 7571-7637.
- [39]. Mendoza-Duarte, J. M., Estrada-Guel, I., Carreño-Gallardo, C., Martínez-Sánchez, R. *J. Alloys Compd.* **2015**, 643, S172-S177.
- [40]. Sharifi, E. M., Karimzadeh, F., Enayati, M. H. *Mater. Des.* **2011**, 32, 3263-3271.
- [41]. Ma, J., Wu, M., Du, Y., Chen, S., Ye, J., Jin, L. *Mater. Lett.* **2009**, 63, 905-907.
- [42]. Stadie, N. P., Billeter, E., Piveteau, L., Kravchyk, K. V., Dobeli, M., Kovalenko, M. V. *Chem. Mater.* **2017**, 29, 3211-3218.
- [43]. Liu, Z., Yuan, X., Zhang, S., Wang, J., Huang, Q., Yu, N., Zhu, Y., Fu, L., Wang, F., Chen, Y., Wu, Y. *NPG Asia Mater.* **2019**, 11, 12.
- [44]. Jin, J., Wei, Z., Qiao, X., Fan, H., Cui, L. *RSC Adv.* **2017**, 7, 26710-26716.
- [45]. Li, M., Yu, S., Chen, Z., Wang, Z., Lv, F., Nan, B., Zhu, Y., Shi, Y., Wang, W., Wu, S., Liu, H., Tang, Y., Lu, Z. *MoC Inorg. Chem. Front.* **2017**, 4, 289-295.
- [46]. Xiao, Y., Zheng, L., Cao, M. *Nano Energy* **2015**, 12, 152-160.
- [47]. Haldar, S., Roy, K., Nandi, S., Chakraborty, D., Puthusseri, D., Gawli, Y., Ogale, S., Vaidhyanathan, R. *Adv. Energy Mater.* **2018**, 8, 1702170.
- [48]. Liu, H., Cao, Q., Fu, L. J., Li, C., Wu, Y. P., Wu, H. Q. *Electrochem. Commun.* **2006**, 8, 1553-1557.
- [49]. Rui, X. H., Ding, N., Liu, J., Li, C., Chen, C. H. *Electrochim. Acta* **2010**, 55, 2384-2390.
- [50]. Wang, Y.-Q., Gu, L., Guo, Y.-G., Li, H., He, X.-Q., Tsukimoto, S., Ikuhara, Y., Wan, L.-J. *J. Am. Chem. Soc.* **2012**, 134, 7874-7879.
- [51]. Wu, H., Meng, Y., Lu, K., Wei, Z. *J. Mater. Chem. A* **2013**, 1, 6366-6372.
- [52]. Roy, K., Chavan, V., Hossain, S. M., Haldar, S., Vaidhyanathan, R., Ghosh, P., Ogale, S. B. *ChemSusChem.* **2020**, 13, 196-204.
- [53]. Haldar, S., Roy, K., Kushwaha, R., Ogale, S., Vaidhyanathan, R. *Adv. Energy Mater.* **2019**, 9, 1902428(1-10)
- [54]. Cui, Y., Zhao, X., Guo, R. *Electrochim. Acta* **2010**, 55, 922-926.
- [55]. Ma, Z., Peng, Y., Wang, G., Fan, Y., Song, J., Liu, T., Qin, X., Shao, G. *Electrochim. Acta* **2015**, 156, 77-85.
- [56]. Huggins, R. A., Nix, W. D. *Ionics* **2000**, 6, 57-63.
- [57]. Christensen, J., Newman, J. *J. Electrochem. Soc.* **2006**, 153, A1019-A1030.

- [58]. Qi, Y., Harris, S. J. *J. Electrochem. Soc.* **2010**, 157, A741-A747.
- [59]. Cheng, Y. T., Verbrugge, M. W. *J. Appl. Phys.* **2008**, 104, 083521.
- [60]. Zhang, X., Sastry, A. M., Shyy, W. *J. Electrochem. Soc.* **2008**, 155, A542-A552.
- [61]. Cheng, Y. -T., Verbrugge, M. W. *J. Power Sources* 2009, 190, 453-460.
- [62]. Huggins, R. A., Nix, W. D. *Ionics* **2000**, 6, 57-63.
- [63]. Qi, Y., Harris, S. J. *J. Electrochem. Soc.* **2010**, 157, A741-A747.
- [64]. Zhang, X., Sastry, A. M., Shyy, W. *J. Electrochem. Soc.* **2008**, 155, A542-A552.
- [65]. Cheng, Y. T., Verbrugge, M. W. *J. Appl. Phys.* **2008**, 104, 083521.
- [66]. Suryanarayana, C., Norton, M. G. Springer, New York, **1998**.
- [67]. Zak, A. K., Majid, W.H. Abd., Abrishami, M. E., Yousefi, R. *Solid State Sci.* **2011**, 13, 251-256.
- [68]. Singla, G., Singh, K., Pandey, O. P. *Appl. Phys A* **2013**, 113, 237-242.
- [69]. Biju, V., Sugathan, N., Vrinda, V., Salini, S. L. *J. Mater. Sci.* **2008**, 43, 1175-1179.
- [70]. Sadovnikov, S. I., Rempel, A. A., Gusev, A. I. Springer, Switzerland (**2018**).
- [71]. Knowles, K. M., Howie, P. R. *J. Elast.* **2015**, 120, 87-108.
- [72]. Sun, Z. M., Ahuja, R., Lowther, J. E. *Solid State Commun.* **2010**, 150, 697-700.
- [73]. Yang, X. Q., Sun, X., Lee, S. J., McBreen, J., Mukerjee, S., Daroux, M. L., Xing, X. K. *Electrochem. Solid State Lett.* **1999**, 2, 157-160.
- [74]. Whiteley, J. M., Kim, J. W., Kang, C. S., Cho, J. S., Oh, K. H., Lee, S.-H. *J. Electrochem. Soc.* **2015**, 162, A711-A715.
- [75]. Zhang, W., Schroder, D., Arlt, T., Manke, I., Koerver, R., Pinedo, R., Waber, D. A., Sann, J., Zeier, W.G., Janek, J. *J. Mater. Chem. A* **2017**, 5, 9929-9936.
- [76]. Tardif, S., Pavlenko, E., Quazuguel, L., Boniface, M., Marechal, M., Micha, J.-S., Gonon, L., Mareau, V., Gebel, G., Guillemaud, P. B., Rieutord, F., Lyonnard, S. *ACS Nano* **2017**, 11, 11306-11316.
- [77]. Paillard, V., Puech, P., Laguna, M. A., Temple-Boyer, P., Caussat, B., Couderc, J. P., Mauduit, B. *Appl. Phys. Lett.* **1998**, 73, 1718.
- [78]. Liu, F., Zhou, J., Wang, S., Wang, B., Shen, C., Wang, L., Hu, Q., Huang, Q., Zhou, A. *J. Electrochem. Soc.* **2017**, 164, A709-A713.
- [79]. Naguib, M., Halim, J., Lu, J., Cook, K. M., Hultman, L., Gogotsi, Y., Barsoum, M. W. *J. Am. Chem. Soc.* **2013**, 135, 15966-15969.

- [80]. Kong, F., He, X., Liu, Q., Qi, X., Zheng, Y., Wang, R., Bai, Y. *Electrochim. Acta* **2018**, 265, 140-150.
- [81]. Shen, C., Wang, L., Zhou, A., Zhang, H., Chen, Z., Hu, Q., Qin, G. *J. Electrochem. Soc.* **2017**, 164, A2654-A2659.
- [82]. Zhu, J., Sakaushi, K., Clavel, G., Shalom, M., Antonietti, M., Fellingner, T.-P. *J. Am. Chem. Soc.* **2015**, 137, 5480-5485.
- [83]. Wang, B., Wang, G., Wang, H. *J. Mater. Chem. A* **2015**, 3, 17403-17411.
- [84]. Su, L., Zhou, Z., Shen, P. Core-shell Fe@Fe₃C/C *Electrochim. Acta* **2013**, 87, 180-185.
- [85]. Kitajou, A., Kudo, S., Hayashi, J. -I., Okada, S. *Electrochemistry* **2017**, 85, 630-633.
- [86]. Xiao, Y., Zheng, L., Cao, M. *Nano Energy* **2015**, 12, 152-160.
- [87]. Li, M., Yu, S., Chen, Z., Wang, Z., Lv, F., Nan, B., Zhu, Y., Shi, Y., Wang, W., Wu, S., Liu, H., Tang, Y., Lu, Z. *Inorg. Chem. Front* **2017**, 4, 289-295.
- [88]. Li, R., Wang, S., Wang, W., Cao, M. *Phys. Chem. Chem. Phys.* **2015**, 17, 24803-24809.
- [89]. Gao, Q., Zhao, X., Xiao, Y., Zhao, D., Cao, M. *Nanoscale* **2014**, 6, 6151-6157.
- [90]. Zhang, H. -J., Wang, K. -X., Wu, X. -Y., Jiang, Y. -M., Zhai, Y. -B., Wang, C., Wei, X., Chen, J. -S. *Adv. Funct. Mater.* **2014**, 24, 3399-3404.
- [91]. Huang, H., Feng, T., Gan, Y., Fang, M., Xia, Y., Liang, C., Tao, X., Zhang, W. *ACS Appl. Mater. Interfaces* **2015**, 7, 11842-11848.
- [92]. Yang, J., Li, L., Zhang, Y., Zhang, Y., Sun, C., Tan, H., Huang, W., Yan, Q., Dong, X. *ChemistrySelect* **2016**, 1, 2682-2686.
- [93]. Ali, A., Hantanasirisakul, K., Abdala, A., Urbankowski, P., Zhao, M. -Q., Anasori, B., Gogotsi, Y., Aissa, B., *Langmuir* **2018**, 34, 11325-11334.
- [94]. Lin, Z., Sun, D., Huang, Q., Yang, J., Barsoum, M. W., Yan, X. *J. Mater. Chem. A* **2015**, 3, 14096-14100.
- [95]. Xu, Y., Liu, Q., Zhu, Y., Liu, Y., Langrock, A., Zachariah, M. R., Wang, C. *Nano Lett.* **2013**, 13, 470-474.
- [96]. Sun, X., Shao, C., Zhang, F., Li, Y., Wu, Q. -H., Yang, Y. *Front. Chem.* **2018**, 6, 166.
- [97]. Zhao, M. -Q., Xie, X., Ren, C. E., Makaryan, T., Anasori, B., Wang, G., Gogotsi, Y. *Adv. Mater.* **2017**, 29, 1702410.
- [98]. Bak, S. -M., Qiao, R., Yang, W., Lee, S., Yu, X., Anasori, B., Lee, H., Gogotsi, Y., Yang, X. -Q. *Adv. Energy Mater.* **2017**, 7, 1700959.

- [99]. Xie, X., Kretschmer, K., Anasori, B., Sun, B., Wang, G., Gogotsi, Y. Porous $Ti_3C_2T_x$
ACS Appl. Nano Mater. **2018**, 1, 505-511.

Chapter 4

High capacity, power density and cycling stability of silicon Li-ion battery anode by few layer black phosphorous additive

The exceptionally high theoretical capacity of silicon as the Li-ion battery anode material (4200 mAhg^{-1}) is hard to realize and stabilize in practice due to its huge (300%) volume changes during the lithiation/de-lithiation. The design, constitution, and microstructure of the anode hold the key to a desired potential solution. Towards this end, herein we exploit the very high flexibility of few layer black phosphorous (FLBP), far exceeding that of most of the carbon forms extensively studied thus far, attributed to its typical puckered structure and low Young's Modulus, to realize an exceptionally high capacity, power density and stability Si nanoparticle based anode design. Our process employs a simple physical mixture of silicon nanoparticles (SiNPs) and chemically exfoliated few layer black phosphorous (FLBP), which is simple and easily scalable. Very high capacity values reaching 3386 mAhg^{-1} and 2331 mAhg^{-1} at current densities of 0.1 Ag^{-1} and 0.5 Ag^{-1} , respectively, are obtained with impressive stability measured up to 250 cycles.

Related publication: *Sustainable Energy Fuels*, 2019, 3, 245

Declaration

The text and the figures being reproduced in this chapter are from my own co-authored “*Sustainable energy and fuels, 2019, 3, 245*” with permission from the publisher.

I acknowledge help and active collaboration of Dr. Malik Wahid and Dr. Dhanya Puthusseri in the fabrication of the device and analyses.

1. Introduction:

The modern electrically driven world largely depends on the availability of efficient and robust energy storage devices, both stationary and transportable. Li-ion batteries are still the highest performing commercialized rechargeable batteries, wherein graphite is used as anode due to its high stability, very low irreversible capacity loss, and low cost. However, its theoretical capacity being low (372 mAhg^{-1} , LiC_6) alternate high capacity anode materials are being sought as its potential replacements. In particular, these include alloying materials such as Sn (theoretical capacity 992 mAhg^{-1} , $\text{Li}_{4.4}\text{Sn}$) and Si (theoretical capacity 4200 mAhg^{-1} , $\text{Li}_{22}\text{Si}_5$).¹⁻³ In spite of its very high theoretical capacity, utilization of silicon as anode has been plagued by the stability issues emanating from the huge (300%) volume expansion and contraction upon lithiation and de-lithiation, which causes mechanical rupturing and loss of electrical contact between the particles.⁴⁻⁶ Along with the volume expansion, there are a number of other issues with Si anode such as poor material conductivity, repeated chemical reaction with the electrolyte, high irreversible capacity loss, and fast capacity fade.⁷ Therefore, a number of very interesting and innovative strategies have been designed and employed in recent years to stabilize the high capacity of Si, the primary ones being the use of carbon materials as elastic conducting additives in the form of composites or coatings, as discussed at length in multiple significant contributions by Y. Cui and coworkers, Y. Sun and coworkers, and many others.^{3-6,8-16} In some cases, these strategies are synthetically quite complex, while in other cases the use of larger weight fraction of carbon concedes the high capacity advantage of silicon, because carbon in itself is an ineffective material (capacity $300\text{-}400 \text{ mAhg}^{-1}$) in the capacity context.^{8-10,15,16}

Non-carbon conductive alternatives which could either be effective in minute quantities in accommodating the stresses and/or could concurrently contribute through their own high Li ion storage capacity have also been researched, and innovative strategies based on the use of Si-X compounds like SiO_2 , SiO , CaSi_2 , Mg_2Si etc. have shown a good promise in this regard.¹⁷⁻²¹ Several research groups have tried to stabilize the Si anode by optimizing the binders as well. Poly(vinylidene fluoride), PVDF being the most widely used binders for Li ion battery electrode preparation owing to its fair thermal and electrochemical stability is not so popular in the context of Si anode since its elasticity is less.^{22,23} Thus, capacity fade results even after 8-10 charge discharge cycles due to formation of protective solid electrolyte interphase (SEI) layer in the subsequent cycles.²⁴ Hence several research groups have come up with different binders like

styrene butadiene rubber (SBR), sodium carboxymethyl cellulose (CMC), cross linked polymer binder like Poly(acrylic acid), PAA-CMC composite where large numbers of -OH and -COOH groups render very strong and stable covalent bond and/or hydrogen bonding interaction with oxide layers grown on the Si nanoparticles, thus giving stability and preventing the electrode from further pulverization.²⁵⁻³⁰

Herein we examine chemically exfoliated few layer black phosphorous (FLBP) as an extremely large stress absorbing material with very low Young's modulus (superior to most carbon forms studied thus far), and that too as a simple physical additive, rendering a Si nanoparticle-based anode with very high capacity, power density and stability. Importantly, we have used the conventional and most widely used PVDF binder without resorting to special binders containing highly oxygen containing groups or cross-linking polymer.

2. Experimental section:

2.1. Electrode fabrication:

Electrodes were prepared by direct mixing of SiNPs (Global Nanotech, Method: laser synthesized, particle size: <80 nm) and FLBP (Prepared by exfoliating Black Phosphorous purchased from Smart-elements GmbH, Vienna, Austria) under sonication in NMP (N-methyl 2-pyrrolidone, Sigma Aldrich). To the resulting mixture 10% PVDF (Polyvinylidene difluoride, Sigma Aldrich) binder and 10% conducting carbon were used as the additives. The weight ratio of the SiNP to FLBP were kept 92:8. The final slurry was dropcasted on a copper foil for followed by an overnight vacuum drying at 80°C. High vacuum conditions were applied to prevent the degradation of FLBP.

2.2. Characterizations:

Powder X-ray diffraction and Field emission SEM (FE-SEM) along with Energy dispersive x-ray (EDAX) were done in Bruker D8 advance x-ray instrument and NOVA nano SEM respectively. Cyclic voltammetry was performed in Ametek potentiost at a scan-rate of 0.1 mV/s keeping the vertex potentials from 0.01 to 2 V. The galvanostatic charge discharge measurements were carried out in MTI corporation battery analyzer at variable current densities of 0.1 Ag⁻¹, 0.5 Ag⁻¹,

1 Ag⁻¹, 2 Ag⁻¹ and 4 Ag⁻¹. The electrochemical impedance spectroscopy (EIS) measurements were studied in the Ametek potentiostat instrument. For the bias voltage dependent impedance measurements, the freshly prepared cells were discharged to 0.01 V and then charged back to 2V to complete the first charging discharging cycle. Subsequently, the cell was discharged to the impedance bias voltage before recording the impedance plot.

3. Result and discussions:

It has been theoretically shown that FLBP, a material of immense current interest due to its several unique properties, can sustain huge strains up to 32% in view of its unique puckered structure which can flatten in response to strain without need to extend P-P bond,³¹⁻³⁴ a property not endowed to flat graphene. The attendant much smaller Young's modulus of FLBP thus brings great value to strain engineering in the case of Si-anode problem. Thus, by deviating considerably from the mainstream strategies like Si-C anode strategy for Li-ion anode or synthesis of binary or ternary Si compounds that involve rigorous synthesis protocols, we have achieved a SiNPs based anode that not only delivers the desirable exceptionally high reversible capacity of 3386 mAhg⁻¹ but also an excellent rate-cum-cyclic stability. This is realized by using FLBP as a simple and optimum physical additive. Note, that this and other values reported here are calculated with the total weight of the material and not simply the weight of Si. Thus, capacity values of 2331 mAhg⁻¹, 1901 mAhg⁻¹, 1617mAhg⁻¹, and 1207 mAhg⁻¹ are realized at current densities of 0.5 Ag⁻¹, 1 Ag⁻¹, 2Ag⁻¹, and 4Ag⁻¹, respectively, which are among the highest reported for Si (**Table 1**).

We would like to emphasize that physical addition of phosphorene or few layer BP (FLBP) to a silicon nanoparticle-based anode adopted in our work is a novel approach than using any form of phosphorous for silicon-based compound synthesis and using that compound as an anode. This is because in our case the mechanically flexible identity of FLBP is maintained intact, which is of utmost importance for the absorption of stresses.

There is only one previous report by Bo et. al. wherein phosphorene was used to encapsulate Si to improve the performance of the Si anode.³⁶ However unlike our work using the most commonly and widely used PVDF binder, they have used Sodium Carboxymethyl Cellulose

(NaCMC) binder which is known to stabilize SiNP based anodes even without addition of any external additives^{37,38}. Also they have shown stability data only upto 100 cycles without providing any rate performance data.

As an example of the other compound formation strategy one could cite a recent interesting work of Park et. al. who synthesized silicon di-phosphide (SiP_2) compound having a 3D crystalline framework with a 6-fold coordination of Si, in which the Li-ion storage mechanism involves a three-step reaction between SiP_2 and Li.³⁵ Moreover, the authors also included carbon in the composite anode through high energy ball milling of SiP_2 and C (super P) in a weight ratio of 60:40 and achieved a good reversible capacity of 1661 mAhg^{-1} though with poor cycling stability (only 50% retention after 100 cycles) when operated in potential window of 0-2V. Moving into a revised potential window of 0.25-2 V they could achieve enhanced cycling stability, though with lower reversible capacity of 1137 mAhg^{-1} . Clearly, as indicated above, our strategy has rendered far superior results, and that too without any carbon additive.

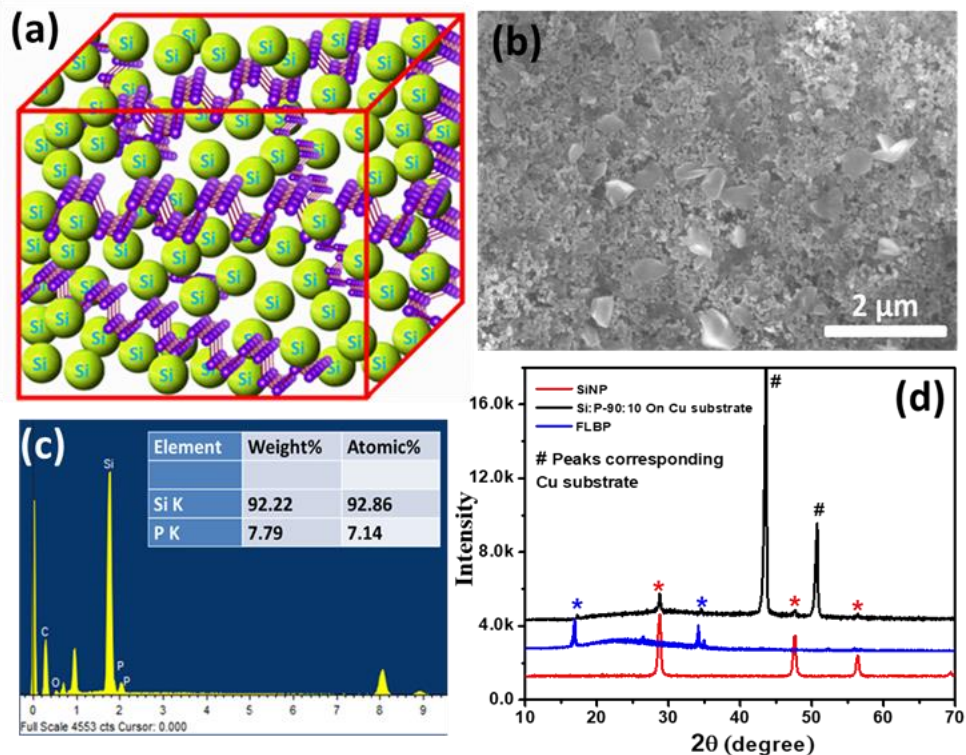


Figure 1. (a) The schematic depicting the union of FLBP and SiNPs in the electrode, (b) FE-SEM image of SiNP-FLBP composite electrode, (c) EDAX data showing a composition of SiNP:FLBP (92:8), (d) X-ray diffraction data of SiNP, FLBP and SiNP-FLBP composite (on Cu foil electrode).

The Field emission scanning electron microscopy (FESEM), and high-resolution transmission electron microscopy (HRTEM) data, and the Raman spectrum for FLBP can be found in Fig. 2. The FESEM images and XRD data for SiNP are shown in Fig. 3. These data confirm the essential expected structural and morphological features pertaining to the two separate systems used in this work.

The detailed SiNPs/FLBP electrode fabrication procedure employed in our work is given in the electrode fabrication section in the experimental section. Different relative compositions of SiNPs and FLBP were carefully studied (Please see Table 2). The optimized 92:8 weight ratio (8 wt.% FLBP) yielded the best performance. Fig. 1a displays a cartoon depicting the expected physical union of SiNPs and FLBP in the electrode. The uniform distribution of inter-dispersed FLBP in the continuum of SiNPs can be clearly seen from Fig. 1b. The comparison of the morphology in the case of only SiNP and SiNP-FLBP composite electrode is shown in Fig. 7. The weight ratio observed from the EDAX analysis (Fig. 1c) for the optimal case is in good agreement with the weight ratios added during electrode fabrication. The x-ray diffraction (XRD) shown in Fig. 1d depicts that the physical individuality of constituents is maintained in the electrode, as expected.

The rate-cum-stability plots shown in Fig. 4a with other electrochemical measurements such as cyclic voltammetry (Fig 4c), charge discharge plot of SiNP and SiNP-FLBP composite (Fig. 4b and 4d) reveal a highly impressive near theoretical electrochemical performance rendered by our FLBP-based SiNPs LiB anode design. A comparison in the cyclic voltammetry data of SiNP and SiNP-FLBP composite system can be found in Fig 6 which reveals that the FLBP is electrochemically inactive in terms of enhancing the capacity. The first reversible capacity achieved in the SiNPs/FLBP-92:8 mixed anode (3384 mAhg^{-1}) is clearly superior to the separate SiNPs (3003 mAhg^{-1}) and FLBP (143 mAhg^{-1}) anodes. The expected capacity based on the observed (and not theoretical) individual performances of SiNPs and FLBP amounts to 2717 mAhg^{-1} which implies a significant enhancement of 669 mAhg^{-1} . This enhancement in FLBP/SiNP may be accounted for by considering the improvement in the effective capacity delivered by the SiNPs when inter-dispersed by FLBP in the electrode. It can be noted from the inset of fig. 4b and fig. 7 (a and b) that the electrochemical contribution of FLBP is really negligible in terms of capacity and it is only working as a stress absorbing cushion by protecting SiNP from pulverization on continuous lithiation-delithiation cycles.

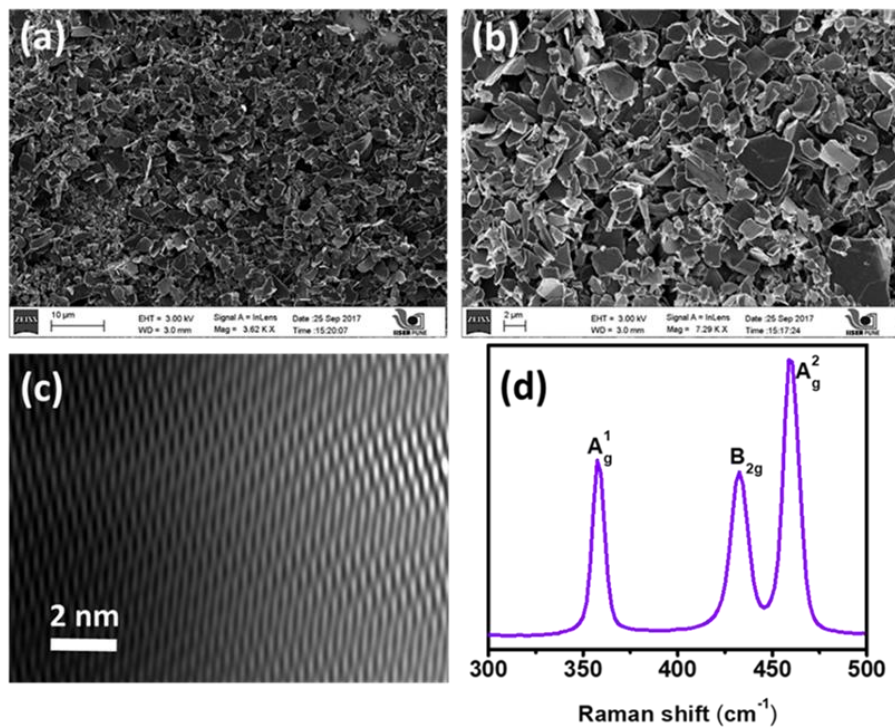


Figure 2. (a-b) FESEM images and (c) HRTEM image showing the morphology of the few layer black Phosphorous and (d) Raman Spectra showing the signature peaks of FLBP.

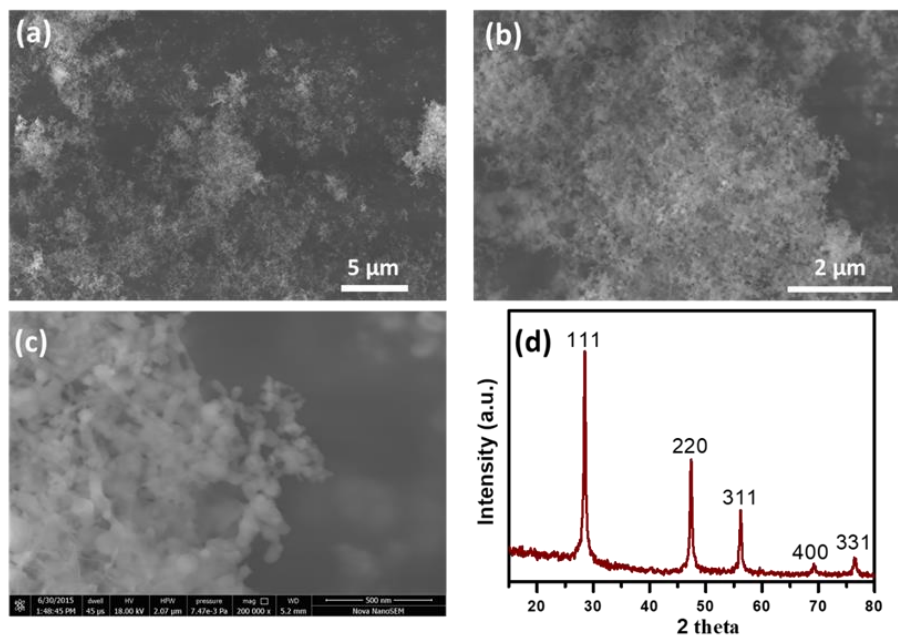


Figure 3. (a-c) FESEM images Si nanoparticles showing the morphology and particle size, (d) XRD showing the characteristic peaks of Si

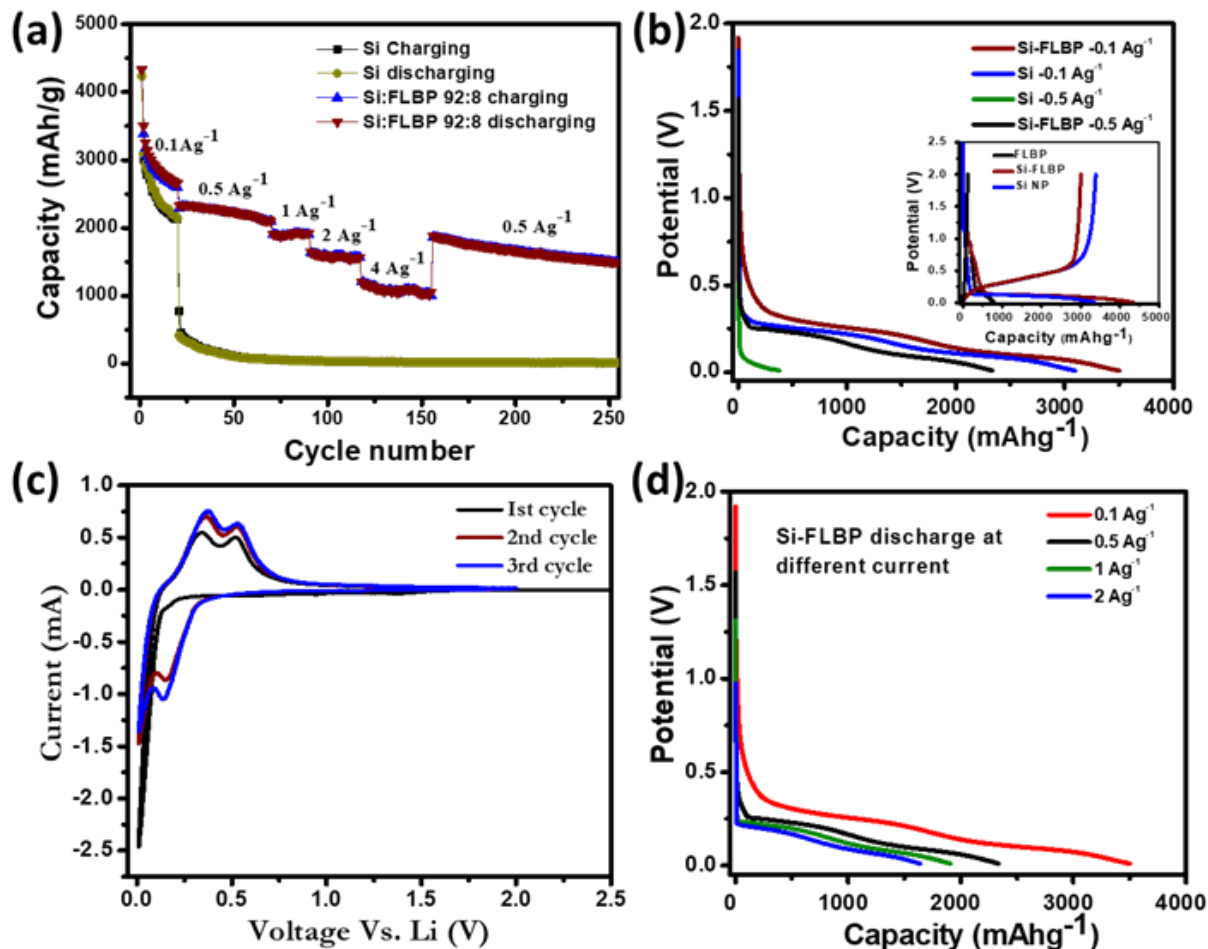


Figure 4 (a) Rate cum stability plot for SiNP and SiNP-FLBP composite electrode, (b) Comparison of charge discharge plots for SiNP and SiNP-FLBP composite 0.1 Ag^{-1} and 0.5 Ag^{-1} , (c) Cyclic voltammety data of SiNP-FLBP composite system and (d) Charge discharge data for SiNP-FLBP composite system at 0.1 Ag^{-1} , 0.5 Ag^{-1} , 1 Ag^{-1} and 2 Ag^{-1} .

From Fig. 4a dramatic differences may be noted in the rate-cum-stability characteristics of the SiNP and FLBP/SiNP anodes. At low current density of 0.1 Ag^{-1} , after 20 cycles the SiNPs electrode shows 72% retention, while the SiNPs/FLBP-92:8 electrode shows 79% retention. The curves bifurcate significantly as the current density is increased. Indeed, the remarkable result realized in this work is the high capacity retention at higher current densities as revealed by Fig. 4a. While the capacity of only SiNPs-based anode declines by an order of magnitude to a value of only 392 mAhg^{-1} at higher current density of 0.5 Ag^{-1} , the SiNPs/FLBP-92:8 displays commendable retention with a capacity of 2331 mAhg^{-1} even at this current density (Fig. 4b), a huge difference indeed. The stability comparison over the next 50 cycles at higher current

density of 0.5Ag^{-1} further establishes the superiority of SiNPs/FLBP-92:8 anode. While the only SiNPs anode deteriorates by a drastic decline to the value of only 58mAhg^{-1} from the initial 393mAhg^{-1} at the end of the 50th cycle, the SiNPs/FLBP-92:8.

The stability comparison over the next 50 cycles at higher current density of 0.5Ag^{-1} further establishes the superiority of SiNPs/FLBP-92:8 anode. While the only SiNPs anode deteriorates by a drastic decline to the value of only 58mAhg^{-1} from the initial 393mAhg^{-1} at the end of the 50th cycle, the SiNPs/FLBP-92:8 displays tremendous integrity with a very high capacity value of 2120mAhg^{-1} at the end of the 50th cycles. The increase in the current density to 1Ag^{-1} renders an equally impressive value of 1907mAhg^{-1} which runs quite smoothly for the next 20 cycles. The capacities of 1636mAhg^{-1} and 1207mAhg^{-1} are realized at the current densities of 2Ag^{-1} and 4Ag^{-1} , respectively. When again brought back to 0.5Ag^{-1} , a high capacity of 1866mAhg^{-1} is still realized (effectively implying 83% retention after 150 cycles performed at different high currents) and the anode ran smoothly at this current for the next 20 cycles.

We would further like to point out that we achieved a high first cycle Coloumbic efficiency of 78% which is quite comparable with other reports. This in-turn implies that in our case there is no huge irreversible capacity loss in the first cycle, which is a commonly encountered problem with Si-based anodes. Only a few reports have shown higher first cycle Coloumbic efficiency, but with a high amount of carbon used as additive. Separately, our cell also showed a promising performance in terms of very slow capacity fading and long term cyclic stability (65 % retention of capacity after 250 cycles). A comparison of the electrochemical performance of SiNP-FLBP with other recent reports on Si or Si/C composites as anode for Li-ion battery is presented in table 1.

To confirm the mechanical stability of SiNP-FLBP electrode in comparison with the only SiNP-based electrode under lithiation/de-lithiation, the morphology of both these electrodes was examined after several charge discharge cycles. The FESEM images of Fig. 5 (a and b) reveal that the SiNP electrode forms multiple huge cracks after 20 cycles, while our SiNP-FLBP electrode does not show any discernible cracks even after 250 cycles. Even in higher magnification, the cracks are visible for SiNP cases whereas no cracks are visible for SiNP-FLBP cases. (Fig. 8)

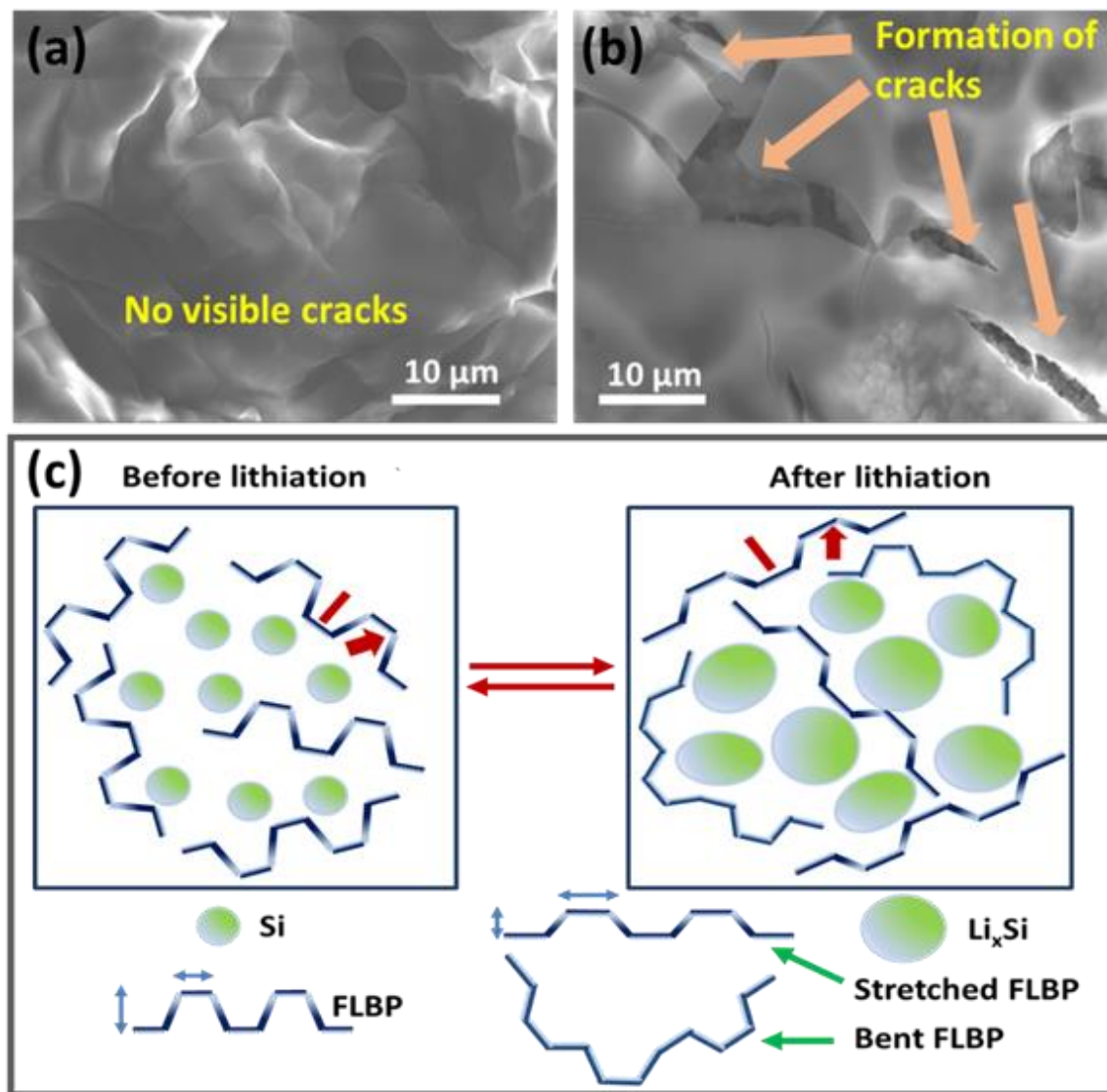


Figure 5. (a-b) Morphology revealed by FE-SEM of (a) SiNP-based anode after 20 charge discharge cycles, and (b) SiNP-FLBP anode after 250 charge discharge cycles. (c) schematic bringing out the primary benefit of using FLBP additive to the SiNP anode.

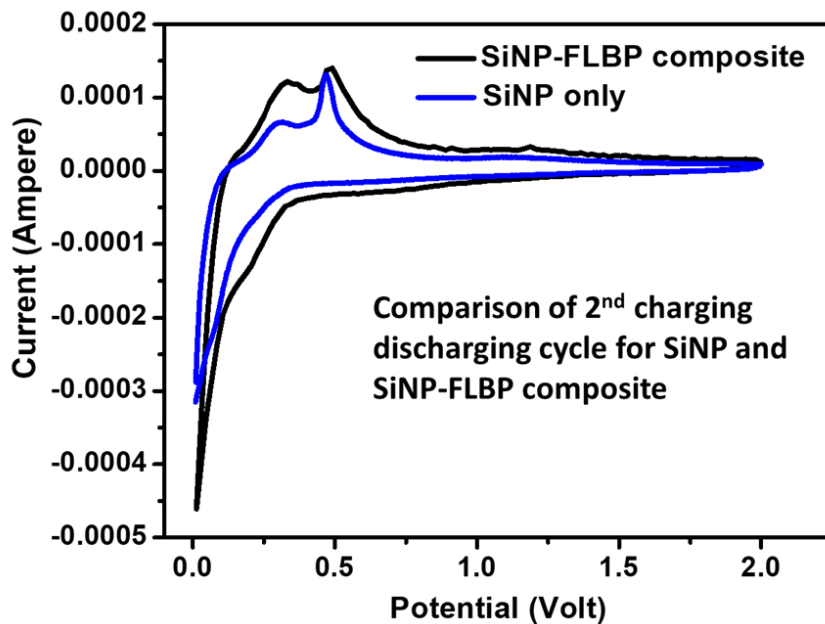


Figure 6. Cyclic Voltammetry comparison of SiNP and SiNP-FLBP composite system.

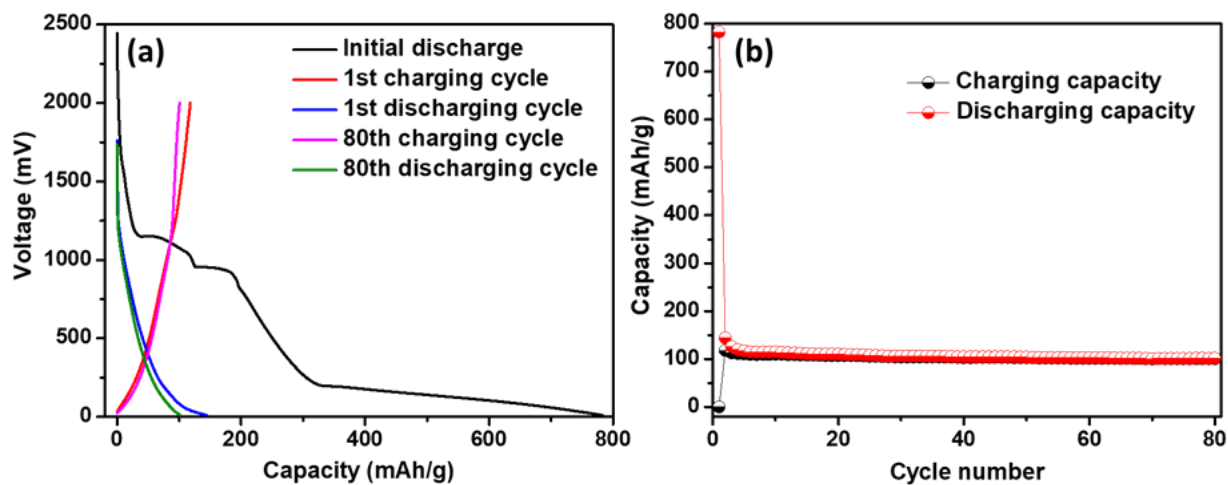


Figure 7. (a) Charge-discharge data, (b) Stability data of only FLBP system.

We can attribute the excellent performance observed in our case to the stress-absorbing cushion provided by FLBP to silicon due to its exceptional flexibility (very low Young's modulus) emanating from the unique puckered crystal structure. Equally importantly, for the SiNP-FLBP anode the SEI layer is also noted to be very stable, and even after long cycling the electrode is covered with a uniform SEI without cracks. This helps the SiNPs maintain the inter-particle electrical contact with conductivity assistance of FLBP leading to very high and stable capacity. A schematic representing the above scenario is presented in the Fig. 5c.

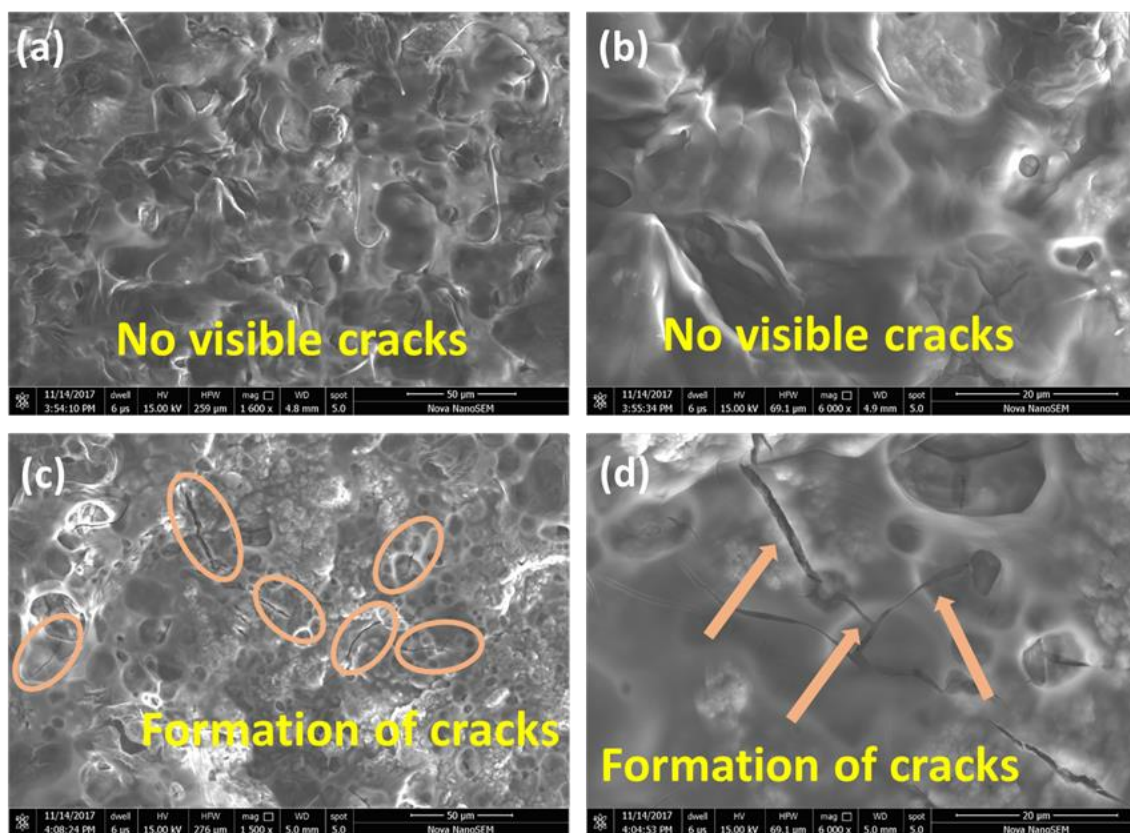


Figure 8. (a) and (b) SiNP-FLBP electrodes after 250 charge discharge cycle. (c) and (d) SiNP based electrode after 20 charge discharge cycle.

In order to probe the lithiation/de-lithiation reaction dynamics in the two cases we carried out the impedance analysis at different bias voltages over the frequency range from 100 mHz to 300 kHz, and AC amplitude of 10mV. The choice of bias voltage was primarily made on the basis of their working potentials. The basic idea was to excite the cell with an AC impulse at potentials close to the working potentials and record the system response through impedance spectroscopy.

The Nyquist plots for SiNP and SiNP-FLBP at different bias voltages are compared in fig. 9. The R_{CT} (charge transfer resistance) for SiNP and SiNP/FLBP anodes was obtained for the bias voltage of 0V, 0.1V, 0.2V, 0.3V and 0.5V from the respective semicircular curves in fig. 9. The comparison of R_{CT} values suggests that lithiation/ delithiation in SiNP-FLBP is more facile at higher voltage compared to lower voltages (in total contrast with the only SiNP cases) which can be correlated with the electrochemical signatures observed from their charge discharge profiles, where it is clearly seen that the working potential of SiNP-FLBP composite is higher as compared to only SiNP. The arrow in Fig. 4 shows the dramatic change of R_{ct} of SiNP and SiNP-FLBP cases when the bias voltage has been changed to 0.2 Volt from 0.1 Volt. The inset of Fig. 4 shows the change of R_{ct} for the SiNP-FLBP case by changing the potential from 0V to 0.5V. This observation also suggests that the FLBP has a definite electrochemical influence on the lithiation /de-lithiation dynamics in addition to providing a flexible, strain absorbing, and electrically conducting cushion. The electro-chemical influence may be due to different type of lithiation mechanism operative in the composite case (2D material support system) compared to bare nanoparticle case.³⁹

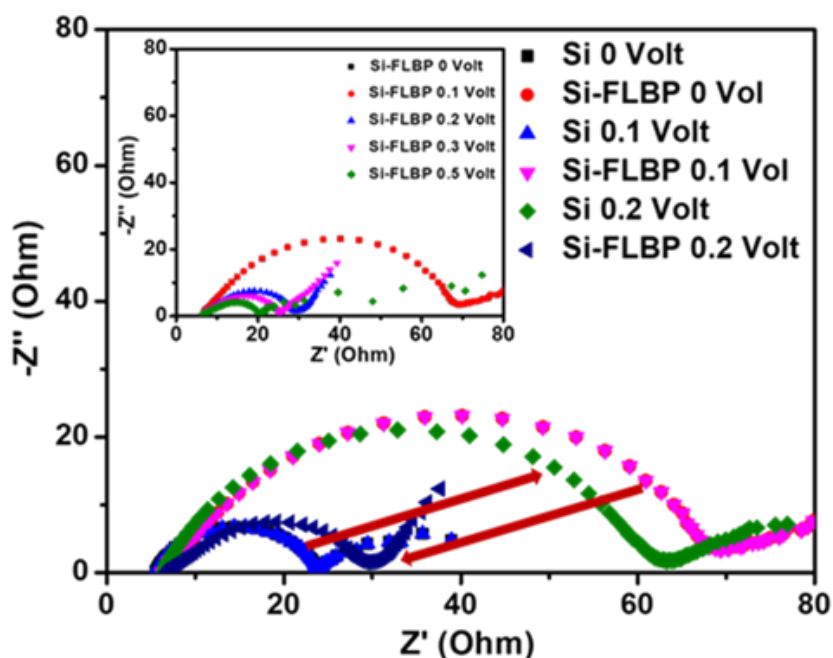


Figure 9. Nyquist plot for electrochemical impedance measurements for SiNP and SiNP-FLBP composite systems at different applied bias voltage. 0 Volt stands for no applied bias. Inset shows the change of charge transfer resistance (R_{ct}) of SiNP-FLBP composite on increasing the bias voltages from 0 Volt to 0.5 Volt.

S.No.	Si Composite	Reversible Capacity (Current Density)	Capacity at (maximum current density)	First cycle Columbic efficiency (%)	Carbon percentage	Journal/ Reference
1.	Si graphene cage composite	3300 mAhg ⁻¹ (200 mAg ⁻¹) (Total mass)	1400 mAhg ⁻¹ (2Ag ⁻¹)	93	9%	⁴⁰ <i>Nat. Energy</i> 2016, 1, 15029.
2.	Si/rGO	2030 mAhg ⁻¹ (200 mAg ⁻¹) (Si weight)	1200 mAhg ⁻¹ (4Ag ⁻¹)	59	25%	⁴¹ <i>Carbon</i> 2017, 120, 397-404.
3.	Carbon coated Si/ graphite Spherical composite	712 mAhg ⁻¹ (130mAg ⁻¹) (Total weight)	626 mAhg ⁻¹ (3.25Ag ⁻¹)	79	21%	⁴² <i>ACS Appl. Mater. Interfaces</i> , 2016, 8 , 12109–12117
4.	Si nano particle graphene composite membrane	1718 mAhg ⁻¹ (100mAg ⁻¹) (Total weight)	307 mAhg ⁻¹ (2 Ag ⁻¹)	54	60%	⁴³ <i>Carbon</i> 2015, 98, 373-380.
5.	Si/ CNM/ Graphene	3200 mAhg ⁻¹ (500mAg ⁻¹) (silicon weight)	2500 mAhg ⁻¹ (3 Ag ⁻¹)	84	50%	⁴⁴ <i>ACS Nano</i> , 2017, 11, 5051–5061.
6.	Si/C microspheres Watermelon	600 mAhg ⁻¹ (120mAg ⁻¹)	500 mAhg ⁻¹ (3Ag ⁻¹)	90	87%	⁴⁵ <i>Adv. Energy Mater.</i> 2017,

7.	Mesoporous Silicon Hollow Nanocubes	2200 mAhg ⁻¹ (100mAhg ⁻¹) (Si weight)	1750 mAhg ⁻¹ (400 mAhg ⁻¹) 1050 mAhg ⁻¹ (30Ag ⁻¹)	80	90%	⁴⁶ ACS Nano, 2017, 11, 4808–4815.
8.	Colloidal nanosilicon from silica	3300 mAhg ⁻¹ (420 mAhg ⁻¹) (Si weight)	2000 mAhg ⁻¹ (2.1Ag ⁻¹) 1100 mAhg ⁻¹ (8.4 Ag ⁻¹)	81	21%	⁴⁷ ACS Nano, 2017, 11, 6065–6073.
9.	Semi-micron-size agglomerate structured silicon-carbon composite	2350 mAhg ⁻¹ (400mAhg ⁻¹) (Total weight)	700 mAhg ⁻¹ (12 Ag ⁻¹)	82	14%	⁴⁸ Journal of Power sources, 2016, 334, 128–136.
10.	Engineering Empty Space between Si Nanoparticles for Lithium-Ion Battery	~1200 mAhg ⁻¹ (800mAhg ⁻¹) (Total mass)	~600 mAhg ⁻¹ (8Ag ⁻¹)	71	53%	⁴⁹ Nano Lett. 2012, 12, 904–909.
11.	Adaptable Silicon Carbon Nano cables Sandwiched between Reduced Graphene Oxide Sheets	~1750 mAhg ⁻¹ (210 mAhg ⁻¹) (Total weight)	~300 mAhg ⁻¹ (12Ag ⁻¹)	50	60%	⁵⁰ ACS Nano, 2013, 7, 1437–1445
12.	Silicon/grapheme sheet/carbon	1500 mAhg ⁻¹ (100mAhg ⁻¹) (Total weight)	1200 mAhg ⁻¹ (500mAhg ⁻¹)	80	49%	⁵¹ Journal of Electrochemical Society, 2017, 164, A6075–A6083.
13.	Three-Dimensional Honeycombed Graphene/Silicon Skeletons	1700 mAhg ⁻¹ (200mAhg ⁻¹) (Total weight)	500 mAhg ⁻¹ (10Ag ⁻¹)	52	58%	⁵² ACS Appl. Mater. Interfaces, 2017, 9, 31879–31886.
14.	Silicon Nanoparticles Embedded in Micro-Carbon Sphere Framework	1200 mAhg ⁻¹ (400mAhg ⁻¹) (Total weight)	~800 mAhg ⁻¹ (940 Ag ⁻¹)	78	70%	⁵³ Nano Lett., 2017, 17, 5600–5606.

15.	Si nanoparticles encapsulated in elastic hollow carbon fibers	1100 mAhg ⁻¹ (100 mAg ⁻¹) (Total Weight)	500 mAhg ⁻¹ (12.8Ag ⁻¹)	45	12%	⁵⁴ Nanoscale 2015, 7, 7409–7414.
16.	Silicon Diphosphide: A Si-Based Three-Dimensional Crystalline Framework as a High-Performance Li-Ion Battery Anode	1137 mAhg ⁻¹ in 110 mAg ⁻¹ (potential window 0.25-2 V)	820 mAhg ⁻¹ (potential window 0.25-2 V) Current density 3.3Ag ⁻¹	86	40%	⁵⁵ ACS Nano 2016, 10, 5701–5709.
17.	Si:P-92:8	3386 mAhg ⁻¹ (100mAg ⁻¹) (Total weight basis)	2331 mAhg ⁻¹ (500 mAg ⁻¹) 1907 mAhg ⁻¹ (1Ag ⁻¹) 1636 mAhg ⁻¹ 2Ag ⁻¹ 1207 mAhg ⁻¹ (4Ag ⁻¹)	78	~8 % Phosphorene	<i>This work</i>

Table 1. Comparison of with the significant literature reports on Si anodes for LIBs involving carbon (**Our data at point no. 17**)

Composition Si:FLBP	First Discharge Capacity (mAhg ⁻¹) @100 mAg ⁻¹	Reversible capacity (mAhg ⁻¹) @100 mAg ⁻¹
82:18	2743	1716
92:8	4329	3386
97:3	2815	2192

Table 2. Electrochemical performance of some SiNPs:FLBP compositions.

4. Conclusions:

In conclusion, we have demonstrated the design of a SiNP based anode for Li-ion batteries with an optimal small quantity of FLBP physical additive which has provided very impressive capacity and stability. This is a departure from the commonly used approach employing different forms of functional carbons as additives or partner materials in Si–C composites. Our approach harnesses the uniquely flexible lithiation/delithiation stress absorbing character of FLBP that is far superior to most carbon forms. Thus, very high capacity values reaching 3386 mAh g⁻¹ and 2331 mAh g⁻¹ at current densities of 0.1 A g⁻¹ and 0.5 A g⁻¹, respectively, are obtained with impressive stability measured up to 250 cycles. We believe that this work will open new avenues for possible utilization of other novel 2D materials in the alkali ion battery context.

References:

- 1 J. B. Goodenough and K. S. Park, *J. Am. Chem. Soc.*, **2013**, 135, 1167–1176.
- 2 W. M. Zhang, J. S. Hu, Y. G. Guo, S. F. Zheng, L. S. Zhong, W. G. Song and L. J. Wan, *Adv. Mater.*, **2008**, 20, 1160–1165.
- 3 S. Suresh, Z. P. Wu, S. F. Bartolucci, S. Basu, R. Mukherjee, T. Gupta, P. Hundekar, Y. Shi, T. M. Lu and N. Koratkar, *ACS Nano*, **2017**, 11, 5051–5061.
- 4 X. Su, Q. Wu, J. Li, X. Xiao, A. Lott, W. Lu, B. W. Sheldon and J. Wu, *Adv. Energy Mater.*, **2014**, 4, n/a-n/a.
- 5 C. Chae, H. J. Noh, J. K. Lee, B. Scrosati and Y. K. Sun, *Adv. Funct. Mater.*, **2014**, 24, 3036–3042.
- 6 Z. Lu, N. Liu, H. W. Lee, J. Zhao, W. Li, Y. Li and Y. Cui, *ACS Nano*, **2015**, 9, 2540–2547.
- 7 X. Zuo, J. Zhu, P. Müller-Buschbaum and Y. J. Cheng, *Nano Energy*, **2017**, 31, 113–143.
- 8 S. Fang, L. Shen, Z. Tong, H. Zheng, F. Zhang and X. Zhang, *Nanoscale*, **2015**, 7, 7409–7414.
- 9 H. Wu, G. Zheng, N. Liu, T. J. Carney, Y. Yang and Y. Cui, *Nano Lett.*, **2012**, 12, 904–909.
- 10 B. Wang, X. Li, X. Zhang, B. Luo, M. Jin, M. Liang, S. A. Dayeh, S. T. Picraux and L. Zhi, *ACS Nano*, **2013**, 7, 1437–1445.
- 11 M. J. Choi, Y. Xiao, J. Y. Hwang, I. Belharouak and Y. K. Sun, *J. Power Sources*, **2017**,

- 348, 302–310.
- 12 J. K. Lee, C. Oh, N. Kim, J. Y. Hwang and Y. K. Sun, *J. Mater. Chem. A*, **2016**, 4, 5366–5384.
 - 13 M. G. Jeong, H. L. Du, M. Islam, J. K. Lee, Y. K. Sun and H. G. Jung, *Nano Lett.*, **2017**, 17, 5600–5606.
 - 14 Y. Li, K. Yan, H.-W. Lee, Z. Lu, N. Liu and Y. Cui, *Nat. Energy*, **2016**, 1, 15029.
 - 15 Q. Xu, J. Y. Li, J. K. Sun, Y. X. Yin, L. J. Wan and Y. G. Guo, *Adv. Energy Mater.*, **2017**, 7, 1–6.
 - 16 Z. Luo, Q. Xiao, G. Lei, Z. Li and C. Tang, *Carbon N. Y.*, **2016**, 98, 373–380.
 - 17 G. A. Roberts, E. J. Cairns and J. A. Reimer, *J. Electrochem. Soc.*, **2004**, 151, A493.
 - 18 H. Kim, J. Choi, H.-J. Sohn and T. Kang, *J. Electrochem. Soc.*, **1999**, 146, 4401–4405.
 - 19 J. Wolfenstine, *J. Power Sources*, 2003, **124**, 241–245.
 - 20 C. M. Park, W. Choi, Y. Hwa, J. H. Kim, G. Jeong and H. J. Sohn, *J. Mater. Chem.*, **2010**, 20, 4854–4860.
 - 21 M. Yamada, A. Ueda, K. Matsumoto and T. Ohzuku, *J. Electrochem. Soc.*, **2011**, 158, A417.
 - 22 J. Li, R. B. Lewis and J. R. Dahn, *Electrochem. Solid-State Lett.*, **2007**, 10, A17.
 - 23 H. Buqa, M. Holzapfel, F. Krumeich, C. Veit and P. Novák, *J. Power Sources*, **2006**, 161, 617–622.
 - 24 W.-R. Liu, M.-H. Yang, H.-C. Wu, S. M. Chiao and N.-L. Wu, *Electrochem. Solid-State Lett.*, **2005**, 8, A100.
 - 25 A. Magasinski, B. Zdyrko, I. Kovalenko, B. Hertzberg, R. Burtovyy, C. F. Huebner, T. F. Fuller, I. Luzinov and G. Yushin, *ACS Appl. Mater. Interfaces*, **2010**, 2, 3004–3010.
 - 26 D. Munao, J. W. M. Van Erven, M. Valvo, E. Garcia-Tamayo and E. M. Kelder, *J. Power Sources*, **2011**, 196, 6695–6702.
 - 27 U. S. Vogl, P. K. Das, A. Z. Weber, M. Winter, R. Kostecki and S. F. Lux, *Langmuir*, **2014**, 30, 10299–10307.
 - 28 B. Lestriez, S. Bahri, I. Sandu, L. Roué and D. Guyomard, *Electrochem. commun.*, **2007**, 9, 2801–2806.
 - 29 N. S. Hochgatterer, M. R. Schweiger, S. Koller, P. R. Raimann, T. Wöhrle, C. Wurm and M. Winter, *Electrochem. Solid-State Lett.*, **2008**, 11, A76.

- 30 J. S. Bridel, T. Azais, M. Morcrette, J. M. Tarascon and D. Larcher, *Chem. Mater.*, **2010**, 22, 1229–1241.
- 31 Q. Wei and X. Peng, *Appl. Phys. Lett.*, , DOI:10.1063/1.4885215.
- 32 J. Jiang and H. S. Park, *J. Phys. D: Appl. Phys.*, **2014**, 47 14–17.
- 33 V. Sorkin and Y. W. Zhang, *J. Phys. D: Appl. Phys.* DOI:10.1088/0957-4484/26/23/235707.
- 34 Z. Sha, Q. Pei, Z. Ding and J. Jiang, *Nanotechnology*, DOI:10.1088/0022-3727/48/39/395303.
- 35 H. T. Kwon, C. K. Lee, K. J. Jeon and C. M. Park, *ACS Nano*, **2016**, 10, 5701–5709.
- 36 P. Bo, X. Yao-Lin, M. Fokko M., *Acta Phys. -Chim. Sin.* **2017**, 33 (11), 2127–2132 .
- 37 X. Su, Q. Wu, J. Li, X. Xiao, A. Lott, W. Lu, B. W. Sheldon and J. Wu, *Adv. Energy Mater.* **2014**, 4, 1–23.
- 38 Z. Bao, M. R. Weatherspoon, S. Shian, Y. Cai, P. D. Graham, S. M. Allan, G. Ahmad, M. B. Dickerson, B. C. Church, Z. Kang, H. W. A. Iii, C. J. Summers, M. Liu and K. H. Sandhage, *Nature*,**2007**, 446, 172–175.
- 39 M.-R. Gao, X. Cao, Q. Gao, Y.-F. Xu, Y.-R. Zheng, J. Jiang and S.-H. Yu, *ACS Nano*, **2014**, 8, 3970–3978.
- 40 Y. Li, K. Yan, H.-W. Lee, Z. Lu, N. Liu and Y. Cui, *Nat. Energy*, **2016**, 1, 15029.
- 41 Y. Yu, G. Li, S. Zhou, X. Chen, H. W. Lee and W. Yang, *Carbon N. Y.*, **2017**, 120, 397–404.
- 42 S. Y. Kim, J. Lee, B. H. Kim, Y. J. Kim, K. S. Yang and M. S. Park, *ACS Appl. Mater. Interfaces*, **2016**, 8, 12109–12117.
- 43 Z. Luo, Q. Xiao, G. Lei, Z. Li and C. Tang, *Carbon N. Y.*, **2016**, 98, 373–380.
- 44 S. Suresh, Z. P. Wu, S. F. Bartolucci, S. Basu, R. Mukherjee, T. Gupta, P. Hundekar, Y. Shi, T. M. Lu and N. Koratkar, *ACS Nano*, **2017**, 11, 5051–5061.
- 45 Q. Xu, J. Y. Li, J. K. Sun, Y. X. Yin, L. J. Wan and Y. G. Guo, *Adv. Energy Mater.*, **2017**, 7, 1–6.
- 46 T. Yoon, T. Bok, C. Kim, Y. Na, S. Park and K. S. Kim, *ACS Nano*, **2017**, 11, 4808–4815.

-
- 47 Z. Liu, X. Chang, T. Wang, W. Li, H. Ju, X. Zheng, X. Wu, C. Wang, J. Zheng and X. Li, *ACS Nano*, **2017**, 11, 6065–6073.
- 48 H. Sohn, D. H. Kim, R. Yi, D. Tang, S. E. Lee, Y. S. Jung and D. Wang, *J. Power Sources*, **2016**, 334, 128–136.
- 49 H. Wu, G. Zheng, N. Liu, T. J. Carney, Y. Yang and Y. Cui, *Nano Lett.*, **2012**, 12, 904–909.
- 50 B. Wang, X. Li, X. Zhang, B. Luo, M. Jin, M. Liang, S. A. Dayeh, S. T. Picraux and L. Zhi, *ACS Nano*, **2013**, 7, 1437–1445.
- 51 N. Kim, C. Oh, J. Kim, J.-S. Kim, E. D. Jeong, J.-S. Bae, T. E. Hong and J. K. Lee, *J. Electrochem. Soc.*, **2017**, 164, A6075–A6083.
- 52 P. Chang, X. Liu, Q. Zhao, Y. Huang, Y. Huang and X. Hu, *ACS Appl. Mater. Interfaces*, **2017**, 9, 31879–31886.
- 53 M. G. Jeong, H. L. Du, M. Islam, J. K. Lee, Y. K. Sun and H. G. Jung, *Nano Lett.*, **2017**, 17, 5600–5606.
- 54 S. Fang, L. Shen, Z. Tong, H. Zheng, F. Zhang and X. Zhang, *Nanoscale*, **2015**, 7, 7409–7414.
- 55 H. T. Kwon, C. K. Lee, K. J. Jeon and C. M. Park, *ACS Nano*, **2016**, 10, 5701–5709.

Conclusions

Chapter 1. This chapter provides a brief idea about the global energy demand, need for renewable energy sources and efficient energy storage devices to store the energy. It also provides basic idea about the basic energy storage systems such as batteries and capacitors followed by their working principle. Although there are exist various energy storage systems of interest, this introduction chapter provides a detailed discussion of batteries, especially Li- ion battery and its working principle and the electrode materials which are being used in this device since the working chapters of this thesis are based on electrode materials for Li-ion batteries..

Chapter 2: This chapter provides a very first report of a ternary intermetallic 3D carbide with unique antiperovskite structure involving both transition (Fe) and post transition (Sn) metals, namely Fe_3SnC , as a stable high capacity anode material for Li ion battery. DFT based computational studies reveal that Li insertion results in deviation from the cubic anti-perovskite structure with a volume expansion that induces significant strain in the electrode as is evident from the XRD and SAED data. We have also in-situ synthesized Fe_3SnC Carbon Nano Fiber (CNF) composite and realized a very impressive cyclic stability. Initial discharge capacity was found to be 1045 mAhg^{-1} and along with a stable reversible capacity of 600 mAhg^{-1} at 200 mA g^{-1} and 500 mAhg^{-1} at 1 Ag^{-1} after 1000 charge discharge cycle with almost ~96% retention of capacity. Similarly, exceptionally high rate performance was observed with a high value of ~500 mAhg^{-1} obtained even at a current of 2 Ag^{-1} . Fe_3SnC is thus projected as a novel and very efficient material among the 3D carbide systems with the corresponding Li storage performance competing the best materials. We believe that this work will open up various new possibilities to focus on intermetallics and 3D carbide systems to be explored in the field of energy storage.

Chapter 3: This chapter provides an original work done on synthesis of an *in-situ* carbon encapsulated VC (VC@C) nanocomposite with three-dimensional core-shell structure by a single-step room-temperature ball milling procedure and investigation of its electrochemical

performance as anodes for LIBs and SIBs. The as-prepared VC@C shows a clear promise for practical use in terms of electrochemical performance with an impressive capacity of 640 mAh g^{-1} after 100 discharge/charge cycles at 0.1 A g^{-1} for LIBs with very high reversibility. The same material also proves to be a good host for Na ions with very good rate capability and cyclic stability. Post cyclic GIXRD data prove that the reversibility and rate capability can be attributed to the robust nature of 3D carbide since the cubic structure of the material remains intact upon charging and discharging. Indeed, VC appears to be one of the most stable battery materials in the current family of anode materials. The room temperature mechano-chemical ball-milling synthesis strategy reported in this present work is facile and cost-effective and therefore, can be expected to be a promising development for the synthesis of other transition metal carbides with different morphologies for use as a potential material in energy storage devices.

Chapter 4: This chapter provides an original work on designing a SiNP based anode for Li-ion batteries with an optimal small quantity of FLBP as physical additive which has provided very impressive capacity and stability. This is a departure from the commonly used approach employing different forms of functional carbons as additives or partner materials in Si-C composites. Our approach harnesses the uniquely flexible lithiation/delithiation stress absorbing character of FLBP that is far superior to most carbon forms. Thus, very high capacity values reaching 3386 mAh g^{-1} and 2331 mAh g^{-1} at current densities of 0.1 A g^{-1} and 0.5 A g^{-1} , respectively, are obtained with impressive stability measured up to 250 cycles. We believe that this work will open new avenues for possible utilization of other novel 2D materials in the alkali ion battery context.

Appendix

Utilization of Novel Covalent Organic Framework for Li-ion Batteries

In this Appendix chapter, novel covalent organic frameworks are utilized as anode materials for Li-ion batteries. Herein, a unique covalent organic nanosheet is shown to deliver a very high reversible specific capacity of 720 mAh g^{-1} at an applied current density of 100 mA g^{-1} with an impressive stability of 1000 cycles. An excellent rate capability is also been observed when the material came up with an extremely low capacity drop ($\sim 20\%$) upon increasing the current density to 1 A g^{-1} from 100 mA g^{-1} . In another study, a chemically exfoliated covalent organic framework is shown splendid full cell performance delivering a specific capacity of 220 mAh g^{-1} with a stability of 200 cycles, LiCoO_2 being used as the cathode.

Related publications:

1. *Adv. Energy Mater.* 2018, 8, 1702170
2. *Adv. Energy Mater.* 2019, 1902428

Declaration

The Covalent Organic Framework Materials discussed in this Appendix have been designed, synthesized and completely characterized by my fellow Ph.D. student Mr. Sattwick Haldar. He has also developed the electrodes and electrochemical set-ups to measure the electrochemical characteristics of the material. For these projects, I have contributed in the coin-cell fabrication, battery measurements and electrochemical analysis. Dr. Dhanya Puthusseri also helped with valuable discussions and intellectual inputs.

Since these two above-mentioned publications will be included in the main thesis of Mr. Sattwick Haldar, a brief discussion is presented here as a part of the Appendix of my thesis.

I have an equal contribution to the first authorship in both of these two publications.

Appendix 1. (*Ref. Adv. Energy Mater. 2018, 8, 1702170*)

Herein, we report a new Covalent Organic Framework which is self-exfoliated during the synthesis and grows as Covalent Organic Nanosheets. The material is extremely novel and unique and is named as (IISERP)-CON 1. After revealing the phase-purity and morphology via Powder XRD and FESEM respectively, the material is employed as an anode material in a Li-ion battery half-cell.

The material showed an impressive specific capacity of 720 mAh g⁻¹ at an applied specific current of 100 mA g⁻¹ which is turned out to be 0.1 C. If the self-standing non-graphenic materials are taken into considerations, this is undoubtedly the highest performing anode material. The material also stands very tall in terms of rate performance. When the current density is increased to 1 A g⁻¹ from 100 mA g⁻¹, (IISERP)-CON 1 comes up with a drop in the specific capacity as little as ~20%. The calculated (from the electrochemical impedance spectroscopy data) Li-diffusion co-efficient is turned out to be 5.48×10^{-11} cm² s⁻¹ which clearly owes to the very high power density shown by the material. The material also shows a very little contribution in terms of surface charge storage when a capacitive vs diffusion contribution calculation is being done from the cyclic voltammetry data (Measuring the cyclic voltammetry data at different scan rates and then fitting in the power law). Both the charge-transfer resistance (8.13 Ω) and the series resistance (11.46 Ω) values are on the lower side as compared to the different reported non-graphenic materials.

To understand the basic lithiation de-lithiation mechanism, we first calculated the number of Li-ions that can be inserted into the unit cell of the CON from the charge-discharge value and this number turns out to be 16. Two major peaks in the cyclic voltammetry confirm two different charge storage mechanisms, one from the intercalation of Li-ions in the interlayer of the two aromatic rings of the CON majorly like graphite and the other from the possible interactions with the -OH groups of the Phloroglucinol rings of the CON which is being proven from the computational studies and the post cycling XPS measurements.

It can be concluded herewith that a self-exfoliated a covalent organic nanosheet having Li binding functional groups can be an excellent anode choice for Li-ion batteries.

Appendix 2. (*Ref. Adv. Energy Mater. 2019, 1902428*)

Herein, two novel covalent organic frameworks have been synthesized followed by a chemical exfoliation via 4+2 cycloaddition (Diles-Alder reaction) in contrary to the appendix-1 where the covalent organic nanosheet was self-exfoliated during the synthesis. This work gives a validation to the claim done in the appendix-1. It proves an exfoliated covalent organic framework can potentially be much more effective in terms of storing charge when used as the anodes for Li-ion batteries.

The two exfoliated COFs (IISERP-COF 7 and IISERP-COF 8) are named as IISERP-CON 2 and IISERP-CON 3. After confirming the phase purities and revealing the morphologies, these two materials are being tested as the anode materials for Li-ion half cells to have a comparative study on the superiority of the CONs over COFs.

The IISERP-CON 2 and IISERP-CON 3 retain capacities at $\sim 770 \text{ mAh g}^{-1}$ and $\sim 590 \text{ mAh g}^{-1}$ respectively after 1000 cycles whereas the IISERP-COF 7 and IISERP-COF 8 deliver a much lower specific capacities of $\sim 200 \text{ mAh g}^{-1}$ and $\sim 120 \text{ mAh g}^{-1}$ respectively after 600 cycles. Even the rate capacities are fairly impressive for both the nanosheets.

Afterwards, practical Li-ion full batteries are fabricated employing these two nanosheets incorporating LiCoO_2 as the cathode material. IISERP-CON 2 and IISERP-CON 3 come up with a stable reversible specific capacity of $\sim 230 \text{ mAh g}^{-1}$ and $\sim 180 \text{ mAh g}^{-1}$ respectively after 200 cycles which is very impressive if we compare these values with commercial graphite-LCO full cell.

The diffusion co-efficient values are also being calculated from the two fabricated full cells which turn out to be $3.69 * 10^{-11} \text{ cm}^2 \text{ s}^{-1}$ and $3.62 * 10^{-11} \text{ cm}^2 \text{ s}^{-1}$ respectively which is much better compare to the graphite anode (of the order of 10^{-13}). This in-turn proves that the Li-ion bulk diffusion is much more facile in the nanosheet materials compare to the graphite anode leading to much better specific capacities and rate capabilities leading to much energy densities (Energy density values are 364 Wh kg^{-1} for IISERP-CON 2 and 286 Wh kg^{-1} for IISERP-CON 3)

Hence, it can be concluded herewith that the CONs are great anode choices to fabricate Li-ion full cells using a commercial cathode.

List of publications

1. **Kingshuk Roy**, Vinila Chavan, Sk Mujaffar Hossain, Sattwick Halder, Ramanathan Vaidhyathan, Prasenjit Ghosh, Satishchandra B Ogale, *Fe₃SnC@CNF: A 3D Antiperovskite Intermetallic Carbide System as a New Robust High-Capacity Lithium-Ion Battery Anode*, **ChemSusChem**, 2019,12,1–10
2. Sattwick Halder*, **Kingshuk Roy***, Rinku Kushwaha, Satishchandra B Ogale, Ramanathan Vaidhyathan, *Chemical Exfoliation as a Controlled Route to Enhance the Anodic Performance of COF in LIB*, **Advanced Energy Materials**, 2019, 1902428
(* **Equal contribution**)
3. **Kingshuk Roy**, Tianyue Li, Satishchandra Ogale and Neil Robertson, *Hybrid Perovskite-like Iodobismuthates as Low-cost and Stable Anode Materials for Lithium-ion Battery Applications*, **UK Patent**. (under process)
4. Subhajit Sarkar, SS Sumukh, **Kingshuk Roy**, Navpreet Kamboj, Taniya Purkait, Manisha Das, Ramendra Sundar Dey, *Facile one step synthesis of Cu-g-C₃N₄ electrocatalyst realized oxygen reduction reaction with excellent methanol crossover impact and durability*, **Journal of colloid and interface science**, 2019, 558, 182-189
5. **Kingshuk Roy**, Malik Wahid, Dhanya Puthusseri, Apurva Patrike, Subas Muduli, Ramanathan Vaidhyathan and Satishchandra Ogale, *High capacity, power density and cycling stability of silicon Li-ion battery anodes with a few layer black phosphorus additive*, **Sustainable Energy and Fuels**, **Sustainable Energy Fuels**, 2019, 3, 245

6. Mani Mahajan*, **Kingshuk Roy***, Swati Parmar, Gourav Singla, O.P. Pandey, K. Singh, Ramanathan Vaidhyanathan, and Satishchandra Ogale, *Room temperature processed in-situ carbon-coated vanadium carbide (VC@C) as a high capacity robust Li/Na battery anode material*, **Carbon**, 2020, (doi.org/10.1016/j.carbon.2020.01.057)

(* **Equal contribution**)

7. Sattwick Haldar*, **Kingshuk Roy***, Shyamapada Nandi, Debanjan Chakraborty, Dhanya Puthusseri, Yogesh Gawli, Satishchandra Ogale, and Ramanathan Vaidhyanathan, *High and Reversible Lithium Ion Storage in Self-Exfoliated Triazole-Triformyl Phloroglucinol-Based Covalent Organic Nanosheets*, **Advanced Energy Materials**, Adv. Energy Mater. 2018, 8, 1702170

(* **Equal contribution**)

8. Aniruddha Basu, **Kingshuk Roy**, Neha Sharma, Shyamapada Nandi, Ramanathan Vaidhyanathan, Sunit Rane, Chandrasekhar V. Rode, Satishchandra B. Ogale, *CO₂ laser direct written MOF-based metal-decorated and hetero-atom doped porous graphene for flexible all-solid-state micro-supercapacitor with extremely high cycling stability*, **ACS Applied Materials and Interfaces**, 2016, 8 (46), 31841–31848

9. Ghulam Mohmad, Subhajit Sarkar, Ashmita Biswas, **Kingshuk Roy**, and Ramendra Sundar Dey, *Polymer-assisted electrophoretic synthesis of N-doped graphene-polypyrrole demonstrating oxygen reduction reaction with excellent methanol crossover impact and durability*. (Manuscript to be submitted)